Electric Field Induced Patterning of Thin Polymer Film

A thesis submitted

in partial fulfillment of the requirements

for the degree of

Doctor of Philosophy

by

Pritam Roy

CENTRE FOR NANOTECHNOLOGY
INDIAN INSTITUTE OF TECHNOLOGY GUWAHATI
GUWAHATI-781039 (INDIA)
AUGUST, 2021

TH-2671_146153005

TH-2671_146153005

STATEMENT

I do hereby declare that the matter embedded in this thesis is the result of experiments and analysis carried out by me at the Center for Nanotechnology, Indian Institute of Technology Guwahati, Assam, India, under the supervision of Dr. Partho Sarathi Gooh Pattader of Center for Nanotechnology, Indian Institute of Technology Guwahati India. In keeping with the general practice of reporting scientific observations, due acknowledgment has been made where the work described is a contribution of another investigator.

Dated:25/11/2020

Place: IIT Guwahati

Name: Pritam Roy

Roll no. :146153005

Center for Nanotechnology

Indian Institute of Technology Guwahati

Guwahati – 781 039

Assam, India

TH-2671_146153005

TH-2671_146153005

C E R T I F I C A T E

It is certified that the work contained in this thesis entitled **"Electric Field Induced Patterning of Thin Polymer Film,"** by **Mr. Pritam Roy**, has been carried out under my supervision and has not been submitted elsewhere for a degree.

Thesis supervisor

Dr. Partho Sarathi Gooh Pattader
Assistant Professor
Department of Chemical Engineering
Center for Nanotechnology
Indian Institute of Technology Guwahati

TH-2671_146153005

TH-2671_146153005

Acknowledgments

It is time to look back on those golden six years of my stay in IIT Guwahati, eight years since I left my native place for study, and ten years of my first introduction to the term 'Nanotechnology'. It is unarguably one of the most memorable experiences in the most incredible journey of my life.

As I began my doctoral research in the winter of 2015, I was both excited and worried. I was excited because I had entered the field of soft materials, a long-cherished desire of mine, and worried, as I was undertaking problems in a research direction, which lacked many explorations.

Thus, first and foremost, thank goes to my thesis supervisor Dr. Partho Sarathi Gooh Pattader, who motivated and criticized me in one way or another, which helped me to work independently. Despite his busy schedule, he always dedicated his time to analyze the problems and give necessary suggestions for my work's betterment.

I wish to thank my doctoral committee members, Prof. Dipankar Narayan Basu, Department of Mechanical Engineering, Prof. Dipankar Bandyopadhyay, and Prof. Tapas K. Mandal, Department of Chemical Engineering, for their valuable suggestions and efforts during my thesis work.

Sincere thanks to Dr. Bolledu Ravi for making me familiar with the colorful world of liquid crystals. I am also thankful to all the PSDL research group members, Mr. Kaniska Murmu, Mr. Ankur Pandey, Mr. Aniruddha Deb, Mr. Sunil Kumar Singh, Ms. Prerona Gogoi, Mr. Krishna Pradeep, Mr. Himanshu Raturi, Ms. Aishwarya Srinivasan, Mr. Rishabh Nikam, and. Mr. Tesfay Gebremikael Teklehaimanot.

I also acknowledge the support from Centre for Nanotechnology and the Analytical Laboratory in in Chemical Engineering for their characterization facilities.

Although words shall fail to carry real emotions, I appreciate friends and batchmates like Mrs. Tamanna Bhuyan and Mr. Shatrudhan Palsaniya for making my stay in IITG special.

Special thanks go to my parents, grandmother, and inlaws for their blessings and good wishes. It is their endless love that backs me to wrap up with this journey. My heartfelt thank goes to Anushikha for her much needed support, cooperation, and solitaire.

Amingaon, November 2020 PRITAM ROY

TH-2671_146153005

TH-2671_146153005

Dedicated
to the rejoice of
harmonious
creativity
&
my parents for all
their sacrifices.

TH-2671_146153005

TH-2671_146153005

EPIGRAPH

.....

Deep in the sea

all molecules repeat

the pattern of one another

till complex new ones are formed.

They make others like themselves

and a new dance starts.

Richard P. Feynman (1955)

TH-2671_146153005

TH-2671_146153005

Synopsis

Electric Field Induced Patterning of Thin Polymer Film

1. Introduction

Patterned surfaces exist in nature for their purposeful use. Self-cleaning superhydrophobic surface,[1] anti-reflective coating,[2] fog collection system,[3] microfluidic adhesive,[4] etc., are some of the examples of structured surfaces with enhanced functionalities. A large number of applications may be formulated exploiting chemical, mechanical, electromagnetic responses to those organized structures. Both bottom-up and top-down approaches can fabricate these structured surfaces. The bottom-up approaches are based upon atomic or molecular self-assembly and organizing elementary units to create patterns. Controlled self-assembly of the block copolymer,[5] controlled evaporative self-assembly in breath figure pattern,[6] phase separation of the polymer blend,[7] and coffee ring effect,[8] are highly promising bottom-up approaches to construct numerous surface structures. Among the top-down methods, template guided dewetting,[9] electrohydrodynamic patterning,[10] nano imprint lithography,[11] capillary force lithography[12] are commonly known micro-manufacturing processes. In all these techniques to get aligned mesostructure, it generally demands pre-patterned masks that are mostly fabricated using any of the conventional lithographic methods. Although photolithography, in this regard, is a routine job for creating sub-micron/nano-patterned masks, it ties in with rigorous fabrication cycles using harsh chemicals. It is also not an economically friendly option. Another problem associated with templated structure fabrication is that intricate geometrical patterns are hard to generate in the experiment. Due to these constraints, soft lithographic techniques are getting popular day by day as it strongly relies on some fundamental physical forces. Replication of mesopatterns on flat soft surfaces without using any high-end instrumentation and tiresome sample preparation technique is a challenge for soft lithographic techniques.

A variety of soft lithographic technique is electric field induced lithography (EFL). It has its usual significance as by controlling the parameters, the dynamics of interface instabilities can be controlled as well as microstructures having a specific lateral wavelength can be generated. These instabilities can also be promoted within a particular area of the film by either patterning the bottom polymer layer or the top electrode before applying the electric field. The electric

TH-2671_146153005

field and hence the destabilizing forces will always be the most substantial where the distance between the polymer and top electrode is the least. Most reported literature includes a thin air gap between the thin polymer layer and the top electrode. Air, having a lower dielectric permittivity, can be easily replaced by the elongated periodic polymer micro-columns from the interface. We introduce a degree of complexity by replacing the air gap with a 5CB nematic liquid crystal. Generally, in reported articles, polymer-air bilayer,[13,14] polymer-polymer bilayer[15] and polymer-polymer-air trilayer[16] under electric field bias, all are investigated widely theoretically and, in few cases, experimentally.[17,18] In the following chapters, we use both hard and soft viscoelastic films (PDMS) and nematic liquid crystal layer (5CB) to constitute the required confined bilayer systems.

The 5CB is a nematic liquid crystal at room temperature. 5CB nematic liquid crystal having high breakdown potential can be easily placed between PDMS and ITO under the high electric field. The large dielectric contrast of nematic 5CB-viscoelastic PDMS bilayer fastens up the processing time of rapid electrodynamic instability across the interface to perturb it into microwells filled with liquid crystal.

2. **Background Theories & Tools**

After the introduction, **Chapter 2** gives a brief outline of the fundamental background theories and tools involved in the other chapters. A basic idea related to the standard scientific terms involved in describing the polymer-liquid crystal bilayer system is concisely explained. In particular, the effect of electrical stress on instabilities at the interface is discussed. A theoretical perspective of some instruments useful for the study is also included.

3. **Electrohydrodynamic Instability: Effect of Rheological Characteristics on the Morphological Evolution of Liquid Crystal-Polymer Interface**

In **Chapter 3**, we show that for viscoelastic polymer, by controlling the extent of crosslinking, one can tune the ratio of the viscous to the elastic component of the polymer [19]. This gives a tunable tool to pattern a viscoelastic polymer in a significantly viscous state and freeze it by making it predominantly elastic at a later stage by inducing more crosslinking[20] by UVO treatment, depending on the type of the polymer used. To date, there is no experimental evidence on the morphological variations (pillars/holes) in EFL settings depending on the rheological properties of the film.

TH-2671_146153005

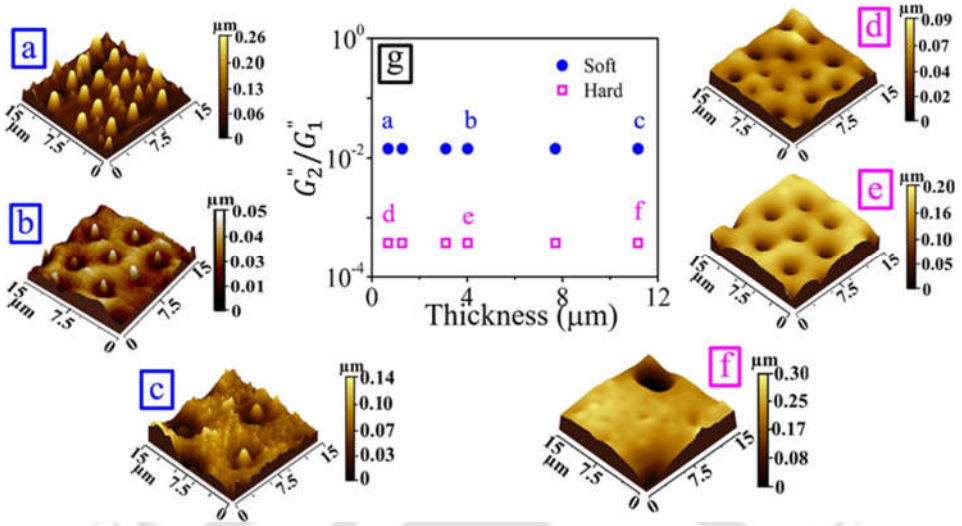

Figure 1: Predominantly micropillar (soft PDMS film, a, b, c) and microwell (hard PDMS film, d, e, f) morphology after EFL experiments. (g) depicts the ratio of loss moduli of the LC layer to that of lower PDMS film against film thickness. The AFM images (a-f) were identified in figure (g), which portray the morphological variation as a function of film thickness and the ratio of loss moduli.

We have demonstrated experimentally for the first time that for a combination of bilayer undergoing EFL, not only the dielectric constant and the film thickness but also the rheology of the bilayer influences the morphology (micropillars or microwells) of the polymer film when instigated within very short time scale. The evolution's short time scale is achieved using 5CB liquid crystal as an upper layer to realize high dielectric contrast across the LC-PDMS interface and low interfacial tension between 5CB and PDMS. Earlier, morphological variation during EFL is predicted numerically by Wu et al.[21] in a combination of the dielectric contrast and the film thickness ratio. In the present experimental study, we demonstrate that for the viscoelastic hard sample, with a relatively higher elastic modulus compared to the viscoelastic soft sample, microwells are obtained irrespective of film thickness. Whereas for viscoelastic soft sample, micropillars are obtained for relatively thin films, and a combination of micropillars and microwells are observed for a film of ~ 11 μm. Lastly, we have demonstrated a pathway to fabricate multiscale patterns of planar boxes and grids decorated with micropillars or microwells by tuning the polymer films' rheological properties.

TH-2671_146153005

4. **Electrodynamic-Contact-Line-Lithography with Nematic Liquid Crystal for Template-Less E-writing of Mesopatterns on Soft Surfaces**

In **Chapter 4**, we report the development of a single-step, template-less and fast pathway, namely, Electrodynamic-Contact-Line-Lithography (ECLL), to write micro to nano-patterns on the surface of a soft polymer film. As a model system, a layer of nematic liquid crystal (NLC), resting on a polymer thin film, is sandwiched between a pair of electrodes emulating the electrowetting on a dielectric (EWOD) setup. Upon application of electric field, the Maxwell stresses generated at the NLC-polymer interface due to the high dielectric contrast stimulated an unprecedented fingering instability at the advancing NLC-polymer-air contact line. In the process, the advancing electrospreading front of NLC left the footprint of an array of micro to nanoscale wells on the polymer surface with a long-range ordering, thus unveiled a pathway for maskless patterning of a soft elastic film. Unlike the conventional electric field induced lithography (EFL), the meso-scale morphology is found to follow the short wave length-scales as the periodicity of the patterns (λ_C) varied linearly with the thickness of the film (h), ($\lambda_C \propto h$). The high dielectric contrast at the NLC-polymer interface and the local fluctuation of the NLC directors ensured a time scale much faster than the same observed for the polymer-air systems.

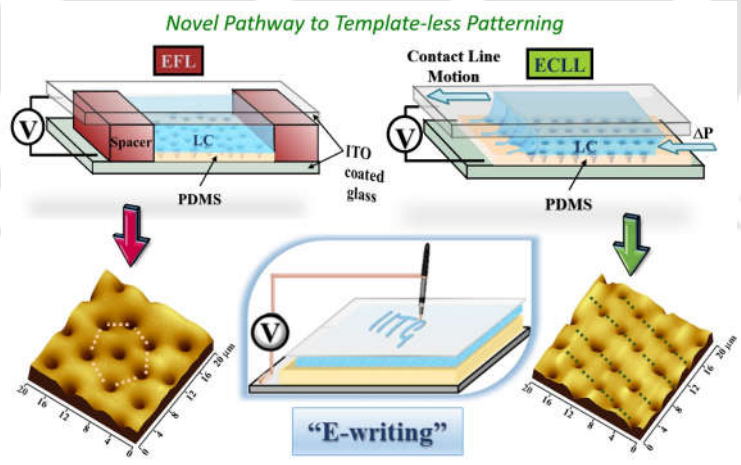

Figure 2: Schematic diagram of the experimental setup: stationary Electric Field induced Lithography (EFL) and Electrodynamic Contact Line Lithography (ECLL). For simplicity, the spacers ECLL method is not shown. Predominantly hexagonal and aligned arrangement of microwells in the PDMS layer is obtained from EFL and ECLL, respectively.

TH-2671_146153005

This study demonstrates an ultrafast, template-less technique, called ECLL, to fabricate ordered micro/nano-pattern on the thin polymer surface. Dynamic electrospreading of periodic NLC front is used as a soft template to create ordered patterns at the interface of the NLC-PDMS in electric field induced instability settings. The faster kinetics of the destabilization due to the high dielectric contrast at the interface of NLC-PDMS layers along with the local fluctuation of the highly dielectric NLC domains, make ECLL a novel technological tool for miniaturized mesoscale patterning of the thin polymer film. This inherent expeditious nature of this NLC-PDMS system for the EHD destabilization of the interface also allows one to write (E-writing) on the polymer surface using an insulated electrode tip as a pen. In contrast to the conventional EFL experiments, which follows longwave characteristics with a hexagonal arrangement of microstructures, ECLL shows a shortwave length scale with $\lambda_c \sim 0.8h$. A simple linear stability analysis reasonably predicts the length scale of the destabilization of the NLC-PDMS interface following conventional EFL and also of the NLC-PDMS-Air three-phase contact line following ECLL. The in-line wavelength (λ_f), of the micro/nano-wells, formed by ECLL, is weakly sensitive to the velocity of the LC spreading front, characterization of which needs extensive study and is reserved for our future publications. The ECLL induced patterning can have significant potential in the fabrication of MEMS/NEMS, optoelectronics, microsensors, etc. We have demonstrated one such application by fabricating the array of solvent responsive light-reflecting micro-pixels.

5. Template-Less Cross-Patterning on Soft Surfaces by Field Driven Directional Flow of Nematic Liquid Crystal

The origin of electric field induced interfacial instability in a confined bilayer system is studied in **Chapter 5**. The bilayer consists of partially crosslinked Polydimethylsiloxane (PDMS) film (isotropic and soft with respect to the fully crosslinked mechanically tough one) and 5CB (4-Cyano-4'-pentylbiphenyl) nematic liquid crystal layer. The instability generated due to Maxwell stresses at the interface for the imposed electric field. Electric field induced motion of anisotropic nematic liquid crystal - wavefront on soft viscoelastic thin film has empowered to produce remarkable opportunities in fabricating arrays of microwells on soft viscoelastic PDMS in any direction with high fidelity in wavelength and geometry of pattern. The present study also validates the genesis of fingering instability at PDMS/air/5CB contact line reported previously as ECLL (Electrodynamic-Contact-Line-Lithography) technique.

TH-2671_146153005

Despite that, it is also shown that the injection of a perpendicular stream of 5CB to the ECLL patterned area in the air under the electric field can create cross patterns with sufficient accuracy.

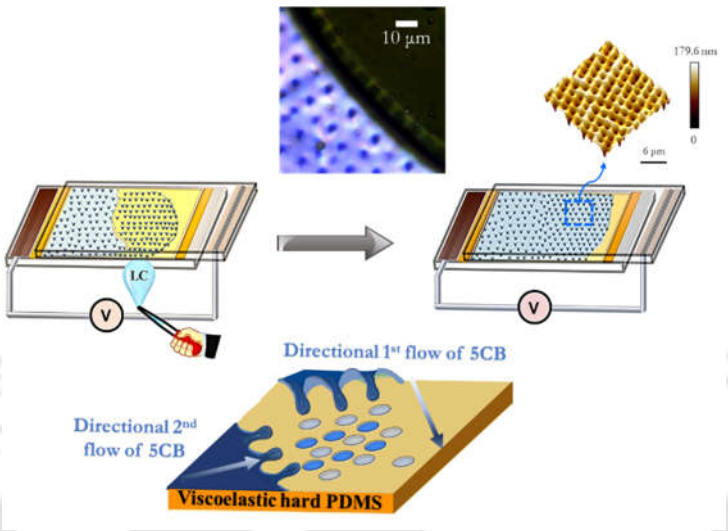

Figure 3: Optical polarized micrograph shows the fingering instability generated during Electrodynamic Contact Line Lithography (ECLL). The schematic diagram of the experimental setup depicts the method of fabricating the cross-pattern and the corresponding Atomic Force Micrograph is shown. The probable mechanism is illustrated.

In a confined arrangement, nematic LC molecules interact differently with the confined walls, i.e., the ITO surface and viscoelastic solid PDMS surface. The wetting characteristics change in applying electric field bias to the system. Electrocapillarity and electrowetting phenomena take place at a specific applied voltage, and with the increase of voltage, the nematic LC wavefront progresses. During this movement, the perturbed LC interface having a particular wavelength of instability penetrates the PDMS thin film to form aligned patterned microwells filled with LC. Herein, we have tried to couple the ECLL phenomenon due to 5CB injection from two different directions in the same system, intending to generate two different electrodynamic instabilities, that subsequently interact within 5CB medium. Herein, we report the experimental findings by considering the nematic flow of two miscible fluids, over the soft viscoelastic solid PDMS film under DC voltage through parallel flat ITO electrodes. Since the fingering instability of 5CB is observed, it is assumed to play a pivot role in determining the instability wavelength. For the 1st line pattern, the spacing between the

TH-2671_146153005

two lines are constrained by the instability wavelength of the same flow. In the second flow of 5CB NLC from the perpendicular direction, compel the previously patterned line of micro-wells to reorganized, and the wavelength in the new direction is determined by the instability of the newly introduced layer of 5CB NLC. If both the wavelengths are identical we obtain square patterns over a large area (Atomic force micrograph, 35 μm×35 μm). The easy applicability and flexibility in designing complex hierarchical structures, open a new horizon for producing a tailor-made patterned surface for novel soft materials in microfluidics and soft lithography applications.

6. **Multiscale Patterning of Thin Viscoelastic Film by a Dynamic Breath Figure Mask and Electric Field Induced Lithography**

Breath figure is a promising patterning technique, and it has been effectively used in preparing porous polymer films. When a hygroscopic drop is placed on a surface, and dropwise condensation of water vapor is performed, a dry band is created around it. This is due to the fact that the drop acts as a humidity sink, which accumulates the evaporated water vapors from its zone of influence.

In **Chapter 6**, the dropwise condensation and contact line dynamics during the evaporation of water on and around a hygroscopic pendant glycerin droplet on a colder surface is studied. Two different surfaces viz. Polystyrene (PS) and Polydimethylsiloxane (PDMS) are used. PS made Petri-dishes are used to achieve a semi-closed system to condense moisture-laden air around a pendant glycerin droplet for investigating the dynamics of the dry band with different concentrations of a defined volume of central glycerin drops. Identical humid conditions are maintained inside the system by introducing a measured volume of water each time at a constant temperature. When the hygroscopic pendant glycerin droplet is exposed to water vapor, two physical processes occur in parallel. The glycerin droplet absorbs moisture to get saturated because of which partial vapor pressure around the spherical droplet is lowered down than the saturated vapor pressure. Due to the rapid kinetics of evaporation of condensed vapor droplets to get absorbed by the central glycerin droplet, the water droplets around the glycerin droplet shrink its contact line with the reduced volume. A hierarchical pattern of condensed water droplets is observed from the dry band to the further from the glycerin droplet. Due to mass loss γ_{sl} increases which often induces mobility to the condensed water droplets.

TH-2671_146153005

Depending on the interplay between the chemical and physical characteristics of the surface, the dynamics of the moving contact line vary. Surface imperfection induced pinning sites for enhancing the advancement of the contact line of glycerin droplet and also condenses water droplets of irregular sizes. The soft viscoelastic PDMS surface is patterned via the breath figure method using glycerin droplet. The dynamics of the dry band is feezed by lowering down the temperature of the PDMS surface using ice. UV-ozone treatment is performed simultaneously to harden the bare PDMS surface. The PDMS surface under the glycerin droplet or water droplets remains soft and deformable in nature.

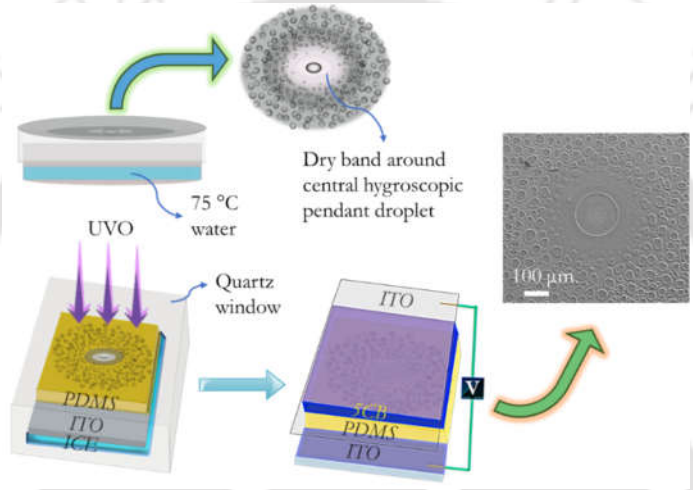

Figure 4: Schematic diagram of the experimental setup depicts the method of fabricating the breath figure assisted electrodynamic patterning process. A scanning electron micrograph of the final PDMS thin film morphology is shown.

A bilayer setup is formed using the keeping the breath patterned PDMS substrate on ITO as the bottom electrode, and on top of it, 5CB NLC is sandwiched by a top ITO electrode. When the electric field is applied, the pre-patterned PDMS surface morphology is further miniaturized with microwells' formation. The process is Electric field induced lithographic technique, and the wavelength of the formed microwells depends on the thickness of PDMS in that particular area. Finally, a multiscale patterned surface is fabricated using a simple breath figure technique and the stationary Electric Field-induced Lithography (EFL) method.

TH-2671_146153005

7. **Electric field induced Template directed Multiscale pattern formation in polymer liquid crystal confined bilayer**

Chapter 7 is an extension of work done in Chapter 3. The control of lateral length-scale of interfacial micro/nano-patterns is of substantial technological interest. In this work, a patterned bottom electrode is employed to vary the electrohydrodynamic stress on the PDMS-5CB interface to pattern the interface. The heterogeneous electric field focusing on the instability at the interface gives rise to different time scales of morphological evolution within the system. Viscoelasticity of the PDMS layer is tuned to get micropillars/microwells exclusively over the PDMS surface. By turning off the voltage supply at any moment, we can arrest the rapid patterning process at a particular voltage to get our desired pattern. Using liquid crystal in the patterning process lowers the threshold voltage and lowers down the feature sizes and wavelengths. Intricate lithographic patterns can be used as electrodes, and with the help of electric field and liquid crystal, multiple long and short scale patterns are achievable.

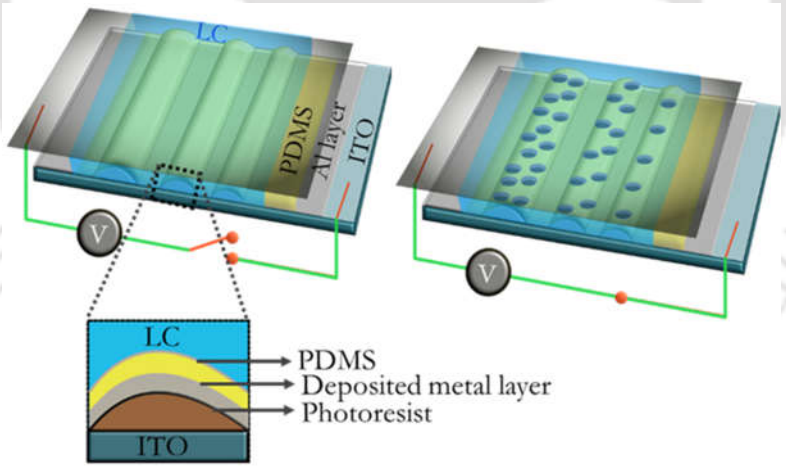

Figure 5: Schematic diagram of the experimental setup depicts the electric field induced multiscale patterning process on PDMS thin film

TH-2671_146153005

8. Conclusions and future scopes of the study

In summary, the novel findings from this thesis are as follows:

We have demonstrated experimentally for the first time that for a combination of bilayer undergoing EFL, not only the dielectric constant and the film thickness but also the rheology of the bilayer influences the morphology (micropillars or microwells) of the polymer film when instigated within concise time scale.

We reported the development of a single-step, template-less, and fast pathway, namely, Electrodynamic-Contact-Line-Lithography (ECLL), to write micro to nano-patterns on the surface of a soft polymer film.

We fabricated template-less square patterns on the surface of a soft polymer film experimentally. The method opens a new horizon of fabricating intricate geometric patterns with the electric field by a directional flow of the nematic liquid crystal.

A facile method is developed for multiscale hierarchical patterning on a soft surface using breath figure lithography and electrodynamic lithography.

A multiscale patterned PDMS thin film has been fabricated using lithographically patterned bottom electrode in PDMS/5CB confined bilayer system under electric field.

In the future, the reported works can be extended to i) The fabrication of complex patterns in composite soft films, ii) The manufacture of templated electrodes, iii) Patterning conducting polymers and block copolymers, iv) Fabricating porous films and calculating their drug loading efficiency, or using them as tissue culture matrix. By obtaining a complete knowledge of physical and chemical forces associated with these patterning processes, better control will be within reach.

TH-2671_146153005

References

[1] C. Dorrer, J. Rühe, *Soft Matter* **2009**, DOI 10.1039/b811945g.

[2] H. K. Raut, S. S. Dinachali, Y. C. Loke, R. Ganesan, K. K. Ansah-Antwi, A. Góra, E. H. Khoo, V. A. Ganesh, M. S. M. Saifullah, S. Ramakrishna, *ACS Nano* **2015**, DOI 10.1021/nn5051272.

[3] H. Bai, L. Wang, J. Ju, R. Sun, Y. Zheng, L. Jiang, *Adv. Mater.* **2014**, DOI 10.1002/adma.201400262.

[4] A. Majumder, A. Ghatak, A. Sharma, *Science (80-.).* **2007**, DOI 10.1126/science.1145839.

[5] M. Luo, T. H. Epps, *Macromolecules* **2013**, DOI 10.1021/ma401112y.

[6] A. Zhang, H. Bai, L. Li, *Chem. Rev.* **2015**, DOI 10.1021/acs.chemrev.5b00069.

[7] A. Karim, T. Slawecki, S. Kumar, *Macromolecules* **1998**.

[8] M. Anyfantakis, D. Baigl, *ChemPhysChem* **2015**, DOI 10.1002/cphc.201500410.

[9] N. Bhandaru, A. Das, R. Mukherjee, *Nanoscale* **2016**, DOI 10.1039/c5nr06690e.

[10] P. G. Oppenheimer, *Electrohydrodynamic Patterning of Functional Materials*, **2013**.

[11] L. J. Guo, *Adv. Mater.* **2007**, DOI 10.1002/adma.200600882.

[12] K. Y. Suh, Y. S. Kim, H. H. Lee, *Adv. Mater.* **2001**, *13*, 1386.

[13] E. Schaffer, T. Thurn-Albrecht, T. P. Russell, U. Steiner, *Nature* **2000**, *403*, 874.

[14] P. Goldberg-Oppenheimer, U. Steiner, *Small* **2010**, DOI 10.1002/smll.201000060.

[15] R. V. Craster, O. K. Matar, *Phys. Fluids* **2005**, *17*, 0.

[16] P. D. S. Reddy, D. Bandyopadhyay, A. Sharma, *J. Phys. Chem. C* **2012**, *116*, 22847.

[17] M. D. Morariu, N. E. Voicu, E. Schaffer, Z. Q. Lin, T. P. Russell, U. Steiner, *Nat. Mater.* **2003**, *2*, 48.

[18] N. Arun, A. Sharma, P. S. G. Pattader, I. Banerjee, H. M. Dixit, K. S. Narayan, *Phys. Rev. Lett.* **2009**, DOI 10.1103/PhysRevLett.102.254502.

[19] J. Nase, A. Lindner, *Phys. Rev. Lett.* **2008**, *074503*, 1.

[20] P. S. G. Pattader, I. Banerjee, A. Sharma, D. Bandyopadhyay, *Adv. Funct. Mater.* **2011**, *21*, 324.

[21] N. Wu, W. B. Russel, *Ind. Eng. Chem. Res.* **2006**, *45*, 5455.

TH-2671_146153005

Publications and Conferences

Publications (From Thesis Work):

1. **P. Roy**, R. Mukherjee, D. Bandyopadhyay, P. S. Gooh Pattader, *Nanoscale* **2019**.
2. **P. Roy**, P. S. Gooh Pattader, *Bulletin of Material Sciences* **2020**. (Accepted)

Conferences:

1. **P. Roy**, P. S. Gooh Pattader, Electrodynamic Fabrication of Microstructures in Polymer-Liquid Crystal Confined Bilayer System, *1st National Student conference on Advances in Chemical Engineering, Department of Chemical Engineering*, Assam Engineering College, Assam, India. **(Best Oral in Oral Presentation).**
2. **P. Roy**, P. S. Gooh Pattader, Fabrication and Characterization of Electric Field Induced Microstructures in Polymer-Liquid Crystal Confined Bilayer System, *Characterization of Polymers and Polymeric Products 2019. (CPP-2019)*, Department of Polymer and Surface Engineering, ICT, Mumbai.
3. **P. Roy**, P. S. Gooh Pattader, Electric Field Induced Instability in Liquid Crystal-Polymer Confined Bilayer System, *2nd International Conference on Nanoscience and Nanotechnology (ICNAN '19),* Centre for Nanotechnology Research (CNR), Vellore Institute of Technology (VIT), India.
4. **P. Roy**, P. S. Gooh Pattader, Electric Field Induced Interfacial Pattern Formation in Viscoelastic Polymer-Liquid Crystal Confined Bilayer System, *6th International Conference Microfluidics and LAB-ON-A-CHIP*, Mumbai, India.
5. **P. Roy**, P. S. Gooh Pattader, Electric Field Induced Instability in Liquid Crystal-Polymer Confined Bilayer System, *Reflux-2018*, Department of Chemical Engineering, IIT Guwahati.

TH-2671_146153005

LIST OF FIGURES

Figure No.		Page No.
2.1	Schematic diagram of the spin coating process for the fabrication of flat polymer thin film.	15
2.2	The measured contact angles for 5CB on a) PDMS and b) ITO coated glass surfaces. The CA of 5CB on viscoelastic solid PDMS was found to lie within ≈ 51°, indicating lower wettability relative to ITO coated glass (CA ≈ 30.5°).	17
2.3	Spin-dewetted droplets of 5CB on PDMS thin film a) Optical bright field micrograph in reflective mode and b) Polarized optical micrograph in reflective mode. Scalebar ~ 50 μm	19
2.4	Alignment of nematic liquid near a solid surface with suitable alignment layers. In the (a) planar case, the director is parallel to the substrate, whereas it is perpendicular in the (b) homeotropic case.	20
2.5	Schematic of rubbing-roller in proximity of a surface where grooves are rubbed, LC molecules align along the direction of the grooves.	21
2.6	Schematics of the experimental processes during the EHD patterning technique under a homogeneous electric field. (a) When voltage is not applied to the system, the interface has only capillary waves. When an electric field is applied, (b) polarization of the dielectric layers occurs, leading to the same charge attraction and opposite charge attraction.	22
2.7	Polarized optical microscopic images of viscoelastic hard PDMS-5CB confined bilayer system between two ITO coated glass plates and under DC voltage. Morphological patterns developed on the PDMS (thickness ~3 μm) covered by LC at ramp bias (a) 0-100 V, (b) 100-150 V, (c) 150-200 V, (d) 200-250 V, (e) 250-300 V, (f) 300-350 V, (g) 350-400 V. (h)	24

TH-2671_146153005

Identical and uniform PDMS microwells formed at a relatively higher voltage (~ 400 V) under the LC.

2.8 The tip sample assembly of AFM. d is the actual tip-sample distance during scan and z is the distance between the sample and the cantilever in rest position. These two distances are different because of cantilever deflection δ_c and sample nonuniformity δ_z. (b)Corresponding line scan of the sample. 26

3.1 Schematic of the experimental set-up (a, b). 5CB – PDMS bilayer is sandwiched between two ITO electrodes, separated by spacers. Upon application of the voltage, the 5CB-PDMS interface destabilise. (c) Storage modulus (G') and Loss modulus (G'') as a function of angular frequency depicts viscoelastic "hard" PDMS has significantly higher storage modulus compared to viscoelastic "soft" PDMS. 33

3.2 AFM images of viscoelastic soft (a-d) and hard (e-h) PDMS film after the EFL experiment. The film thicknesses for (a), (e) are of 7.7 μm; (b), (f) are of 4 μm; (c), (g) are of 3 μm; (d), (h) are of 0.7 μm. (i) Characteristic wavelength (λ) of the morphology as a function of film thickness. Black dotted line represents estimated λ from equation (1). Open pink square (□) and filled dark blue circle (●) represents experimental data points for hard and soft film respectively. 37

3.3 Predominantly micropillar (soft PDMS film, a, b, c) and microwell (hard PDMS film, d, e, f) morphology after EFL experiments. (g) depicts the ratio of loss moduli of the LC layer to that of lower PDMS film against film thickness. The AFM images (a-f) were identified in the figure (g), which portray the morphological variation as a function of film thickness and the ratio of loss moduli. 39

TH-2671_146153005

3.4 Variation of feature (micropillars/microwells) diameter (a) and height (of micropillars) / depth (of microwells) (b) as a function of film thickness. Open pink square (□) and filled blue circle (●) represents experimental data points for hard and soft film respectively. 40

3.5 Morphology as observed in viscoelastic soft (a-c) and hard (d-f) PDMS film. (a, d) and (c, f) are the polarised optical micrographs (POM) during EFL experiments and after the EFL experiments respectively. (b, e) are the bright field image after the removal of the excess LC. (b, c) trace of LC adheres to the micropillars, which acts as the pinning sites while removing excess LC. (e, f) LC filled microwells after removal of the excess LC. 41

3.6 (a) Optical micrograph of the templated viscoelastic hard PDMS film (thickness ~11 μm). The box area remains undeformed during EFL experiment due to the formation of hard silica crust while exposed to UVO and array of single microwell is formed in the grid area (b). (c)-(d) Atomic force micrograph showing topography and the line scans (e) depicting the surface profile and the wavelength of the morphology. 42

3.7 (a) Polarised optical micrograph (POM) of the templated viscoelastic hard PDMS film (thickness ~3 μm) during EFL experiment. The bright-field image of the undeformed box area and an array of ~ 4 microwells in the grid area after removal of LC (b). (c)-(d) Atomic force micrograph showing topography and the line scans (e) portraying the surface profile and the wavelength of the morphology. 43

3.8 (a) Optical micrograph of the templated viscoelastic soft PDMS film (initial thickness ~3 μm). The POM of undeformed box area and of micropillars in the grid area during EFL experiment (b). (c)-(d) Atomic force micrograph showing the topography of the micropillars and the 44

TH-2671_146153005

line scans (e) depicting the surface profile and the wavelength of the morphology.

4.1 (a) Schematic diagram showing the effective distance distribution between the PDMS film to the top electrode. (b) Polarized optical micrograph of the patterned electrode in PDMS/5CB system at 40 V electric field bias. The PDMS film (thickness ~11 μm) is viscoelastic soft. (c) The same interface when the voltage is ramped to 150 V. 58

4.2 Polarized optical micrographs showing the evolution of morphology in the patterned viscoelastic soft PDMS substrate at different voltages, (a) ~ 70 V, (b) ~ 120 V, and (c) ~ 145 V, respectively. (d) Field emission scanning electron micrograph (FESEM) of micropillars formed outside the stripe pattern area. Image (e) shows the FESEM image of aligned rimmed structures from which micropillars are yet to develop. (f) FESEM image of a single developed micropillar in the physically patterned stripe. 60

4.3 Polarized optical micrographs showing the evolution of morphology in the patterned viscoelastic hard PDMS substrate (thickness ~ 3 μm) at different voltages, (a) ~ 180 V, (b) ~ 220 V, and (c) ~ 300 V, respectively. 61

4.4 (a)-(c) Polarized optical micrographs show the evolution of morphology in the patterned viscoelastic hard PDMS substrate (thickness ~ 11 μm) at different voltages, (a) ~ 280 V, (b) ~ 320 V, and (c) ~ 580 V, respectively. (d) FESEM micrograph shows the microwell decorated stripe patterns. 61

5.1 Schematic diagram of the experimental set-up: (a) stationary Electric Field induced Lithography (EFL), (b) Electrodynamic Contact Line Lithography (ECLL), for simplicity the spacers in Fig. (b) are not shown (see text for details). Predominantly hexagonal (a) and aligned (b) arrangement of microwells in the PDMS layer is obtained from EFL and ECLL, respectively. 68

5.2 (a) Schematic representation of the nematic domains in LC in the 73

TH-2671_146153005

absence of an electric field. (b) Schematic depiction of Fréedericksz phase transition in NLC in the presence of the electric field. (c) Deformed NLC-PDMS interface and the plausible LC molecular arrangement that gives rise to the radial structure in Polarized Optical Micrograph (POM). Fig. (d) represents POM of LC filled microwells fabricated by the EFL method at an applied electric potential of 300 V and PDMS film thickness of ~ 8 μm. EFL induced morphology depicts mostly hexagonal arrangement of microwells accompanied by some defects. (e) Bright-field image during ECLL experiment and (f) polarized optical micrograph (POM) of 5CB filled orderly arranged microwells (formed by ECLL method) after careful removal of the top electrode and excess LC. These microwells are spanning over a large area of the PDMS surface. The initial film thickness was ~ 4 μm. The yellow arrow shows the direction of the 5CB-PDMS-Air contact line motion (see text for the details). The magnified inset (50 μm × 50 μm) of fig 5e clearly shows the one-dimensional array of microwells.

5.3 Characteristic wavelength (λ) of the morphology against the PDMS film 76
thickness is shown in Fig. (a). The blue open circles with dotted line depict a theoretical estimation of λ_{max} based on Eq.1 corresponding to the experimental geometry of fixed electrode distance of d = 35 μm and applied voltage = 300 V. The red filled circles represent experimental EFL data for the viscoelastic PDMS films. Few representative AFM images of PDMS films having thickness ~ 11.2 μm (b), ~ 4 μm (c), ~ 3 μm (d), and ~ 0.7 μm (e) are shown, mean wavelengths of which are pointed out in Fig. (a). The green squares depict the separation distance between two neighboring lines of microstructures engendered from ECLL (see text). The Green dotted straight line is an aid to interpret the

TH-2671_146153005

discrete data with a slope of ~ 0.8, representing $\lambda_C \sim 0.8\ h$. Fig. (f) shows morphological patterns developed on the PDMS covered by LC only (EFL experiment). PDMS free surface under air remained stable in the presence of the same external electric field. AFM image (25 μm × 25 μm) of the topography of the PDMS surface, which was covered by LC during the EFL experiment, is shown in the inset. (g) Schematic of the experimental set-up for "E-writing" (see text for detail).

5.4 (a) Wavelength (λ) of the structures against the PDMS film thickness. The pink triangle with a pink dotted line depicts theoretical estimation based on equation 1 corresponds to the experimental geometry of fixed electrode distance of d = 35 μm and varying PDMS film thickness with an air gap instead of LC. The blue circle with a blue dotted line shows theoretical estimation with LC without any air gap. This reveals that LC-PDMS system can give rise to microstructures having a length scale ~ 100 times smaller than that by the air-PDMS system. The red circles are the experimental data for the viscoelastic solid PDMS film with relatively higher elastic component. The black open circles are the experimental data with viscoelastic liquid PDMS film having relatively lower elastic component. The green squares depict the separation distance between two neighboring lines of microstructures engendered from the electric field and dynamic contact line (EF-DCL) induced instability (see text). (b) The curved arrangement of the microwells is achieved by driving the contact line in the curved pathway. This shows the flexibility and versatility of the ECLL method for different micro/nano patterning on demand. 77

5.5 ECLL induced template-less pattern formation in LC-PDMS bilayer system. Figures (a-c) show the time series of a moving contact line and a 82

TH-2671_146153005

	one-dimensional array of microwell formation. (d) Reveals the formation of fingers and lobes, which eventually induce the formation of microwell on the PDMS interface. A schematic representation of the mechanism is depicted in Fig. (e) (see text). AFM image of the one-dimensional array of microwells formed by ECLL is shown in Fig. (f).	
5.6	(a) Microwell diameter against the initial film thickness is shown both for EFL (red circle) and ECLL (green square). (b) Distribution of microwell diameters obtained from 250 microwells fabricated by the EFL method using a PDMS film of thickness ~3 μm. In the inset, a FESEM image is showing the cross-section of a microwell from the same sample.	84
5.7	Polarized optical microscope image of 5CB filled array of microwells, serve as light-reflecting pixels. Upon exposure to the solvent (n-hexane), the nematic to isotropic (N-I) transition takes place at 120 s (fig. a, b, c) and withdrawing the solvent source kindles the array of reflecting lights again due to I-N phase transition (fig. c, d, e).	85
6.1	(a) Schematic diagram shows the EFL method and its characteristic wavelength. (b)-(c), Schematic diagrams depicting ECLL wavelengths (λ_c and λ_f) originated from it. (d) Polarized optical micrograph of advancing LC contact line under which equispaced fingers generated. (e) Schematic diagram showing the ECLL process. (f)AFM micrograph showing the morphology of ECLL patterned area.	99
6.2	(a)-(b) Schematics of the performed experiment imprinting lithographic patterning of viscoelastic solid PDMS thin film (thickness ~3 μm). (c) Optical micrograph of the patterns generated due to embossing and curing the substrate with the attached template of Su-8 in the glass. Scale bar is 50 μm (d) Schematics of the experimental set-up. (e) Optical micrograph of the patterns generated after the flow of 5CB. (f) Atomic force micrograph showing the topography of the PDMS thin film after the experiment.	101
6.3	The characteristic wavelength distribution of (a) EFL, ECLL, and (b) x-ECLL	102

TH-2671_146153005

7.1 (a) Schematic diagram of the first stage of patterning by micro-contact printing of glycerol droplets on viscoelastic hard PDMS thin film. Patterning wavelength (λ_1) is generated due to the patterned mask (b) Image of glycerol sessile droplet on PDMS showing contact angle ≈ 120°. (c) A schematic diagram shows the second stage of patterning. In the reflective mode, the optical micrograph shows the generation of tunable second patterning wavelength (λ_2) due to the formed dry band in breath figure. (d)Schematic diagram of the EFL experiment. (e)Optical micrograph of the breath patterned area after EFL. The magnified view of it shows predominantly uniform microwells having EFL wavelength (λ_3). 110

7.2 (a) Digital photograph of the master (Aluminium foil) and (b) FESEM imaging reveals the dimension and morphology of the open box pattern. (c) Schematic diagram of the process capillary force lithography to prepare the PDMS negative replica (stamp) of the master aluminium foil. (d) Digital photograph of the hard-baked PDMS stamp after releasing from the master. (e) The optical micrograph in the reflective mode showing the morphology of the stamp and (f) the magnified view of it showing predominantly uniform negative pattern replication. 114

7.3 (a)-(f) Schematic representation of the μCP of arrays of glycerol droplets on viscoelastic hard PDMS substrate. (g) The optical micrograph in the reflective mode shows the large are patterned PDMS surface. Schematic representations of (h) the UVO treatment of glycerol droplet masked PDMS surface and (i) the electric field induced lithographic technique. 115

7.4 (a) Optical micrograph in the reflective mode of the square patterned glycerol droplets on the ~3 μm PDMS thin film (b) Optical polarized micrograph of the same area during EFL experiment. The footprints of glycerol droplets on PDMS under the 5CB layer in the presence of 300 V DC shows the formation of distinct microwells. After the EFL experiment, (c) Optical micrograph in the reflective mode shows the glycerol spots after removing the 5CB layer and washing with DMSO. (d) 2D AFM image of the microwell-patterned single glycerol droplet footprint by EFL is shown. In figure (e), the line scans of the AFM image depict the surface profile and wavelength of the morphology for the ~3 μm PDMS thin film. (f) The 3D view of it shows the actual 116

TH-2671_146153005

topography of the footprint after EFL patterning.

7.5 Optical micrographs in the reflective mode breath figure process around the central pendant glycerol droplet on PS petridish surface in different time frames (a) 0 s, (b) 60 s, and (c) 120 s. The sequences also show the increment of dry band width with time. Variation of normalized dry band width against the time of 1 μL central glycerol droplet of different concentrations is shown in figure (d). Figure (e) shows the optical micrograph of the size distribution of evaporative water droplets in the immediate vicinity of the dry band. 118

7.6 (a) Schematic representation of the UVO treatment of breath figure pattern on viscoelastic hard PDMS substrate and EFL experiment using the UVO treated PDMS on ITO as bottom electrode (b) Optical polarized micrograph during EEL experiment. (c) FESEM image of patterned PDMS substrate after removing 5CB top layer. (d) FESEM image of PDMS substrate with breath figure experiment and UVO treatment. 119

TH-2671_146153005

TH-2671_146153005

NOMENCLATURE

Mw	molecular weight
e_r	the contant evaporation rate
v_h	vertical velocity at the surface of the film
P_c	capillary pressure
n_0	ordinary refractive index
n_e	extra ordinary refractive index
$n_{\|\|}$	refractive index parallel to director
$n_\perp$	refractive index perpendicular to the director
I_0	light intensity after polarizer
$\vec{P}$	polarization
$\vec{E}$	applied electric field
G'	storage modulus
G''	loss modulus
h	PDMS film thickness.
d	separation distance between the electrodes.
v_f	speed of the LC front
S_c	spreading coefficient
C	capacitance
A	the surface area of a capacitor
E_p	the induced electric field in PDMS
E_{lc}	the induced electric field in LC
p'_{el}	electrostatic pressure at the interface
r_1 and r_2	radii of curvature at the interface
f / f_0	free energy stored in a capacitor with/without constant voltage
D	dielectric displacement
I	observed intensity at the focal plane of the microscope
m	rate of evaporation
P_{el}	excess electrostatic pressure at the interface due to the application of the electric field
S	order parameter
T_c	clearing point

TH-2671_146153005

T_{mp}	melting point
V	applied bias voltage

Greek letters

ϱ_A	density of volatile liquid (Kg/m^3)
ε_o	dielectric permittivity of vacuum (N m^2/C^2)
φ	azimuthal angle
λ	wavelength of EFL instability
η_{abs}	fraction of optical absorption
θ	contact angle
ε	dielectric constant
$\varepsilon_2, \varepsilon_p$	dielectric constant of PDMS
θ	contact angle
$\vec{\chi}$	dielectric tensor
ω	growth coefficient
k	wave number
τ_d	time scale of instability
$\in$	amplitude of the initial perturbation
τ_w	the time scale of writing
v_w	writing speed for "E-writing"
λ_c	the average spacing between two adjacent parallel arrays of the micro-wells
k_c	critical wavenumber
ξ	electrostatic screening length
λ_f	the mean separation distance between two subsequent microwells in the same array
$\varepsilon_{\|}, \varepsilon_1, \varepsilon_{lc}$	dielectric constants of 5CB nematic
γ	interfacial tension (N/m)
γ	interfacial tension (N/m)
λ_C	periodicity of the pattern
μ	viscosity of fluid (Pa s)
ω	angular velocity

TH-2671_146153005

Acronyms

5CB	4-cyano-4'- pentylbiphenyl
AFM	Atomic force microscope
CFL	Capillary force lithography
d-BF	Dynanic breath figure
DC	Direct current
DI	De-ionized
DMSO	Dimethyl sulfoxide
ECLL	Electrodynamic-Contact-Line-Lithography
EFL	Electric field induced lithography
EHD	Electrohydrodynamic
EWOD	Electrowetting on a dielectric
FESEM	Field emission scanning electron microscope
ITO	Indium tin oxide
LB	Langmuir–Blodgett
LC	Liquid crystal
NLC	Nematic liquid crystal
PDMS	Poly-dimethylsiloxane
POM	Polarized optical micrograph
PS	Polystyrene
UVO	Ultra-violet ozone
x-ECLL	cross Electrodynamic-Contact-Line-Lithography
μCP	Micro-contact printing

TH-2671_146153005

TH-2671_146153005

CONTENTS

		Page No
	List of figures	XIX
	Nomenclature	XXIX
1	**Introduction**	
	1.1 Micro-nano patterning	2
	1.2 Electrohydrodynamic patterning	3
	1.3 Outline of the thesis	5
	References	8
2	**Background Theories & Tools**	
	2.1 Polymer	12
	2.2 PDMS	13
	2.2.1 Mixing the elastomer/oligomer with the curing agent/ reticular agent	14
	2.3 Spin coating	15
	2.4 Interface	15
	2.5 Wettability	17
	2.6 Nematic liquid crystal	18
	2.6.1 Properties of nematic liquid crystal	18
	2.7 Electrohydrodynamic (EHD) instabilities in PDMS/LC bilayer	22
	2.8 Breath Figure	23
	2.9 UVO cleaner	24
	2.10 Atomic force microscope	25
	References	27
3	**Electrohydrodynamic instability: effect of rheological characteristics on the morphological evolution of liquid crystal–polymer interface**	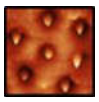
	Abstract	30
	3.1 Introduction	31
	3.2 Experimental	32
	3.2.1 Materials	34
	3.2.2 Methods	34
	3.3 Results and discussion	36
	3.3.1 Length scale and morphology	36
	3.3.2 Templated pattern with the viscoelastic hard film	42

TH-2671_146153005

3.3.3 Templated pattern with the viscoelastic soft film 43
3.4 Conclusions 44
3.6 References 46

4 **Electric field induced Template directed Multiscale pattern formation in polymer liquid crystal confined bilayer** 

Abstract 52
4.1 Introduction 53
4.2 Materials and methods 53
4.2.1 Materials 53
4.2.2 Electrode preparation 54
4.2.3 Patterning electrodes using photolithography 54
4.2.4 PDMS film coating 55
4.2.5 EFL experiment 55
4.2.6 Characterizations 56
4.3 Results and discussion 56
4.3.1 Evolution of morphology at the interface 56
4.3.2 Templated electrode for Spatio-temporal multiscale patterning 56
4.4 Conclusions 62
4.5 References 21

5 **Electrodynamic-Contact-Line-Lithography with Nematic Liquid Crystal for Template-Less E-writing of Mesopatterns on Soft Surfaces** 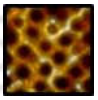

Abstract 66
5.1 Introduction 67
5.2 Experimental section 69
5.2.1 Sample preparation 69
5.2.2 Methods 70
5.2.3 Characterizations 71
5.3 Results and discussion 71
5.3.1 The phenomenon 71
5.3.2 Length and Time scales of EFL 75
5.3.3 Maskless patterning using ECLL 80
5.3.4 Solvent induced switching-pixelation 85
5.5 Conclusions 86
References 88

6 **Template-less Cross-Patterning of Soft Surfaces by the Field driven directed confined flow of nematic Liquid Crystal** 

TH-2671_146153005

Abstract 94
6.1 Introduction 95
6.2 Experimental 96
6.2.1 Materials 96
6.2.2 Methods 97
6.3 Results and discussions 98
6.3.1 Role of 5CB liquid crystal on underlying PDMS 98
6.3.2 Fingering instability in nematic flow 100
6.3.3 Mask-less cross patterning (x-ECLL) with a dominant wavelength 101
6.4 Conclusions 103
References 104
7 Multiscale Patterning of the Soft Interface: A Dynamic Breath Figure Template for Electrohydrodynamic Lithography 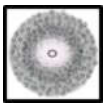
Abstract 108
7.1 Introduction 109
7.2 Materials and methods 111
7.2.1 Materials 111
7.2.2 PDMS substrate preparation 111
7.2.3 PDMS stamp preparation 111
7.2.4 Micro-contact printing (μCP) of glycerin droplets on soft PDMS substrate 112
7.2.5 EFL experiment 112
7.2.6 Dynamic Breath figure (d-BF) experiment 113
7.2.7 Characterizations 113
7.3 Results and discussion 114
7.3.1 Glycerol droplet templated evolution of pattern morphology on viscoelastic hard film 114
7.3.2 Condensation of water vapor on a single glycerol droplet 116
7.3.3 Electric field induced lithography using the d-BF mask 117
7.4 Conclusions 120
References 122
8 Conclusions and scope for future work 123
8.1 Conclusions 126
8.2 Future scopes 128
Appendix-A 130
Appendix-B 133

TH-2671_146153005

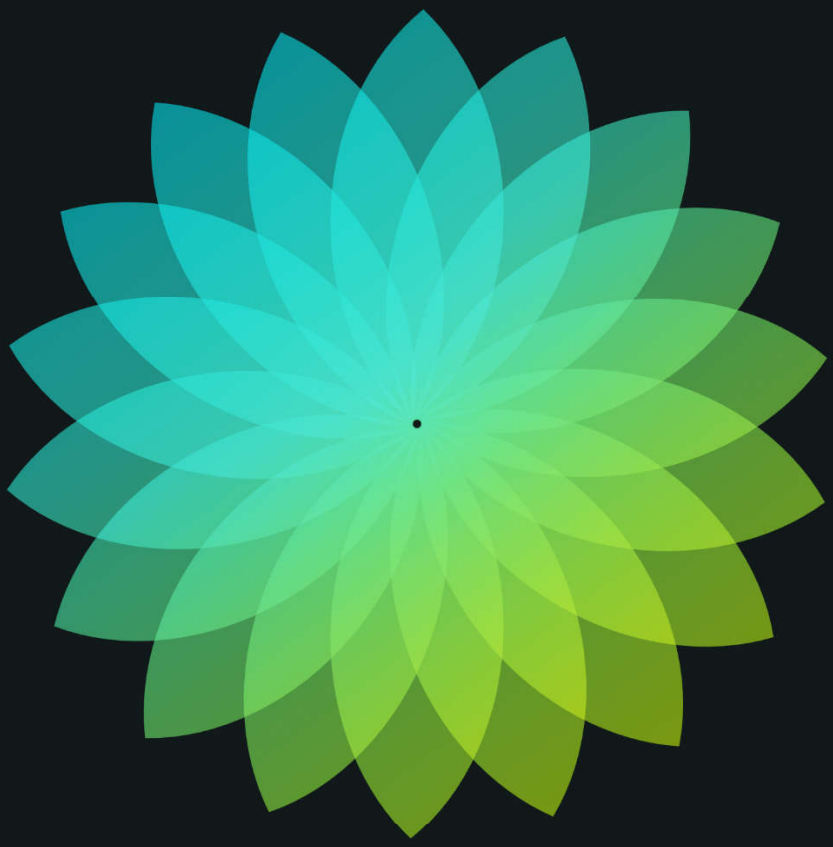

Introduction

TH-2671_146153005

Chapter 1

INTRODUCTION

1.1. Micro-nano patterning

Micro-nano patterns exist in nature for their purposeful use. Self-cleaning superhydrophobic surface,[1] anti-reflective coating,[2] fog collection system,[3] microfluidic adhesive,[4] etc., are some of the examples of structured surfaces with enhanced functionalities. A large number of applications may be formulated exploiting chemical, mechanical, electromagnetic responses to those organized structures. These structured surfaces can be fabricated by both bottom-up and top-down approaches. The bottom-up approaches are based upon atomic or molecular self-assembly and organizing elementary units to create patterns. Controlled self-assembly of the block copolymer,[5] controlled evaporative self-assembly in breath figure pattern,[6] phase separation of the polymer blend,[7] and coffee ring effect,[8] are highly promising bottom-up approaches to construct numerous surface structures. Among the top-down methods, template guided dewetting,[9] electrohydrodynamic patterning,[10] nanoimprint lithography,[11] capillary force lithography[12] are commonly known micro-manufacturing processes. In all these techniques to get aligned mesostructure it generally demands pre-patterned masks that are mostly fabricated using any of the conventional lithographic methods. Although photolithography, in this regard, is a routine job for creating sub-micron/nano patterned masks, it ties in with rigorous fabrication cycles using harsh chemicals. It is also not an economically friendly option. Another problem associated with templated structure fabrication is that intricate geometrical patterns are hard to generate in the experiment. Due to these constraints, soft lithographic techniques are getting popular day by day as it strongly relies on some fundamental physical forces. Replication of mesopatterns on flat soft surfaces without using any high-end instrumentation and tiresome sample preparation technique is a challenge for soft lithographic techniques.

A variety of soft lithographic technique is electric field induced lithography (EFL). It has its usual significance as by controlling the parameters, the dynamics of interface instabilities can be controlled as well as microstructures having a specific lateral wavelength can be generated. These instabilities can also be promoted

TH-2671_146153005

within a particular area of the film by either patterning the bottom polymer layer or the top electrode before applying the electric field. The electric field and hence the destabilizing forces will always be the most substantial where the distance between the polymer and top electrode is the least. Most reported literature includes a thin air gap between the thin polymer layer and the top electrode. Air, having a lower dielectric permittivity, can be easily replaced by the elongated periodic polymeric micro-columns from the interface. We introduce a degree of complexity by replacing the air gap with a 5CB nematic liquid crystal. Generally, in reported articles, polymer-air bilayer,[13,14] polymer-polymer bilayer[15] and polymer-polymer-air trilayer[16] under electric field bias, all are investigated widely theoretically and, in few cases, experimentally.[17,18] In the following chapters, we use both hard and soft viscoelastic films (PDMS) and nematic liquid crystal layer (5CB) to constitute the required confined bilayer systems.

The 5CB is a nematic liquid crystal at room temperature. 5CB nematic liquid crystal having high breakdown potential can be easily placed between PDMS and ITO under the high electric field. The large dielectric contrast of nematic 5CB-viscoelastic PDMS bilayer fastens up the processing time of rapid electrodynamic instability across the interface to perturb it into microwells filled with liquid crystal.

1.2. Electrohydrodynamic patterning

The fundamental area that stitched together this thesis's chapters includes the interfacial structure formation by electrohydrodynamic instability. The influence of the electrostatic field on a polymer surface was investigated widely both theoretically and experimentally. The effect of electrostatic pressure on deformable polymer solution and the formation of "Taylor cone" from polymer drop in the electrospinning technique brought attention to this area.[19][20][21] After that, studies came out revealing the dynamics of electric field induced instabilities where the surface possesses free charge. It was Herminghaus[22] who theoretically explained when a dielectric liquid film is sandwiched between two conducting media, the surface wave amplified in the presence of the electric field, generated across the film due to the difference of the electronic work functions of the adjacent conducting layers. Schaffer et al. successfully investigated the electrodynamic instability in the capacitor model, where no free charges were involved.[23,24] They choose polystyrene (PS), poly (methyl methacrylate)

TH-2671_146153005

(PMMA), and poly(1-bromostyrene)(PSBr) thin films under the electric field having air as the top layer. Chou et al. developed lithographically induced self-construction (LISC)[25], where patterned PMMA pillars were fabricated from spin-cast PMMA thin film on the silicon wafer. They also reported lithographically induced self-assembly (LISA)[26], where they choose poly(methyl methacrylate-co-methacrylic acid) (PMMA−MAA) thin film to get its columnar patterns. Though no external electric field was used, in LISA patterns, the internal electric field between the mask and the polymer layer had its role whereas, in the LISC, patterns were generated under a processing temperature. In LISC, a protruded mask of silicon and in LISA a thermally grown SiO_2 layer was used as a mask in the polymer-air bilayer settings. Deshpande et al.[27] recorded real-time optical microscopic observations of LISA, which showed that the formation of the initial column started first under the corners of the mask pattern, then along the edges. Same trend was followed in the interior of the lithographic pattern. In another of Deshpande et al., they changed the relative surface energies of the layers involved in the LISA process by removing the air gap with oil.[28] In this case, they found disordered patterns with nonuniform size.

Lin et al. extended Schaffer et al.'s work and included another polymeric liquid oligomeric dimethylsiloxane (ODMS) by replacing the air gap in the bilayer model.[29] They choose liquid thin films of polyisoprene (PI) and oligomeric styrene (OS) as the bottom layers. They showed that by introducing a new layer replacing air, the interfacial tension decreases, reducing the characteristic wavelength of the patterns. In another report, Lin et al. used an air/PS/PMMA trilayer system where the molecular weight of PMMA was varied, and a gradient of electrode spacing was used.[30] In the same trilayer, Leach et al. fabricated inverted pillar morphology where the buried PMMA displaced the PS.[31] They supported their observation that as PMMA has a higher dielectric constant than both PS and air, under the electrostatic field, the PMMA/air interface was pulled toward the glass electrode, and the PS/PMMA interface was pulled toward the substrate. Morariu et al. investigated the same air/PS/PMMA trilayer system and showed a combination of dewetting and electrostatic force in action. The induced dewetting of PS due to electrostatic column formation of PMMA was observed. The dewetted rim structure around each PMMA column confirmed the mechanism.[32]

The externally applied electric field effect on the stability and dynamics of the confined leaky dielectric fluid bilayer was theoretically explained using linear stability analysis.[33] The work was extended for a thin trilayer

TH-2671_146153005

system, where the top layer air acts as a bounding fluid.[34] The effect of rheological characteristics of a thin polymer film on the morphological structure evolution in the polymer-air bilayer system was explored by Arun et al.[18] The work was theoretically extended for purely viscous and purely elastic bilayer systems where the air is a top layer.[35] So far, the patterned electrode was used to align the microstructures based on the electric field's variation due to the patterned top electrode. Templated electrode and modulation in the electric field's increment can help fabricate hierarchical and multiscale patterns in rheologically controlled crosslinked PDMS films.[36] In the same scenario, the polymer's viscosity on electrohydrodynamic patterning was investigated experimentally using low viscosity polymers.[14] Different materials like conducting polymer,[37] block co-polymer,[38] crystalline organic material,[39] and inorganic material[40,41] were also patterned in electrohydrodynamic settings. Further, replacing a flat top electrode or patterned electrode with an AFM probe can fabricate nanoscale morphology on the PS surface.[42]

Considering the numerous possibilities EHD patterning techniques can offer, the choice to investigate liquid crystal covered PDMS thin film was rather multidirectional. We use an anisotropic fluid of high dielectric constant as a continuous film and flowing fluid, which could offer possibilities beyond patterning based on isotropic fluids.

1.3. Outline of the thesis

An electric field has always been used to amplify the interfacial capillary wavering. We studied the electric field induced instabilities for an isotropic/anisotropic interface with very high dielectric contrast of the two phases. Employing the observations, several straight forward and cost-effective pathways of patterning are introduced for the first time.

Following this introduction chapter, **Chapter 2** aims to provide a basic idea of the materials used and their underlying properties. It incorporates the fundamental concepts of working principles of tools employed for fabrication and characterizations. The physics of nematic liquid crystals, in general, is discussed.

In **Chapter 3**, it is shown that for viscoelastic polymer, by controlling the extent of crosslinking, one can tune the ratio of the viscous to the elastic component of the polymer. This gives a tuneable tool to pattern a

TH-2671_146153005

viscoelastic polymer in a significantly viscous state and to freeze the pattern by making it predominantly elastic at a later stage by inducing more crosslinking, which can be done by UVO treatment, depending on the type of the polymer used. To date, there is no experimental evidence on the morphological variations (pillars/holes) in EFL settings depending on the rheological properties of the film.

Chapter 4 details spatial variation of the electric field using physically patterned bottom electrode in the PDMS-5CB bilayer system. A multiscale pattern is obtained by using the patterned electrode. The distance variation between the stripe patterned PDMS to the top flat electrode determines the variation in the formed microstructures' length scales. The stripe periodicity, also a lateral length scale, tries to align the formed interfacial structures due to the homogeneous electric field across the stripe patterns. The rheological properties of PDMS can be varied to decorate the stripe patterns with micropillars and microwells.

Chapter 5 gives a comprehensive description of the development of a single-step, template-less, and fast pathway, namely, Electrodynamic-Contact-Line-Lithography (ECLL) technique to write micro to nanopatterns on the surface of a soft polymer film. The work also gives a proof of concept to use a pointed top electrode to confine the electrohydrodynamic stress to write patterns in any direction (E- writing))at one's will.

Chapter 6 describes the origin, theory, and experimental results for the pattern rectification technique in rapid electrohydrodynamic lithography settings. When the second stream of the liquid crystal is injected perpendicularly to the ECLL patterned microwells in air, they rearrange according to the wavelength of instability corresponding to the perpendicular liquid crystal stream. We can synthesize square patterns of microwells over a large area on PDMS.

Chapter 7 presents a novel route for the fabrication of multiscale and hierarchical structured substrate using breath figure lithography and electric field-induced lithography. In this study, a dynamic breath figure mask is fabricated by performing dropwise condensation around a hygroscopic droplet. The mask is fabricated on viscoelastic hard PDMS substrate for selective UVO treatment. Finally, EFL experiment with the substrate and 5CB liquid crystal gives us the desired patterned substrate. Herein, we fabricate, by unconventional lithographic methods, controlled micro-nano structured surfaces cost-effectively.

TH-2671_146153005

Finally, the thesis concludes with **Chapter 8**, highlighting the prospects for the future of the EFL and ECLL techniques and their application potential.

भारतीय प्रौद्योगिकी संस्थान गुवाहाटी • Indian Institute of Technology Guwahati •

TH-2671_146153005

References

[1] C. Dorrer, J. Rühe, *Soft Matter* **2009**, DOI 10.1039/b811945g.

[2] H. K. Raut, S. S. Dinachali, Y. C. Loke, R. Ganesan, K. K. Ansah-Antwi, A. Góra, E. H. Khoo, V. A. Ganesh, M. S. M. Saifullah, S. Ramakrishna, *ACS Nano* **2015**, DOI 10.1021/nn5051272.

[3] H. Bai, L. Wang, J. Ju, R. Sun, Y. Zheng, L. Jiang, *Adv. Mater.* **2014**, DOI 10.1002/adma.201400262.

[4] A. Majumder, A. Ghatak, A. Sharma, *Science (80-.).* **2007**, DOI 10.1126/science.1145839.

[5] M. Luo, T. H. Epps, *Macromolecules* **2013**, DOI 10.1021/ma401112y.

[6] A. Zhang, H. Bai, L. Li, *Chem. Rev.* **2015**, DOI 10.1021/acs.chemrev.5b00069.

[7] A. Karim, T. Slawecki, S. Kumar, *Macromolecules* **1998**.

[8] M. Anyfantakis, D. Baigl, *ChemPhysChem* **2015**, DOI 10.1002/cphc.201500410.

[9] N. Bhandaru, A. Das, R. Mukherjee, *Nanoscale* **2016**, DOI 10.1039/c5nr06690e.

[10] P. G. Oppenheimer, *Electrohydrodynamic Patterning of Functional Materials*, **2013**.

[11] L. J. Guo, *Adv. Mater.* **2007**, DOI 10.1002/adma.200600882.

[12] K. Y. Suh, Y. S. Kim, H. H. Lee, *Adv. Mater.* **2001**, *13*, 1386.

[13] E. Schaffer, T. Thurn-Albrecht, T. P. Russell, U. Steiner, *Nature* **2000**, *403*, 874.

[14] P. Goldberg-Oppenheimer, U. Steiner, *Small* **2010**, DOI 10.1002/smll.201000060.

[15] R. V. Craster, O. K. Matar, *Phys. Fluids* **2005**, *17*, 0.

[16] P. D. S. Reddy, D. Bandyopadhyay, A. Sharma, *J. Phys. Chem. C* **2012**, *116*, 22847.

[17] M. D. Morariu, N. E. Voicu, E. Schaffer, Z. Q. Lin, T. P. Russell, U. Steiner, *Nat. Mater.* **2003**, *2*, 48.

[18] N. Arun, A. Sharma, P. S. G. Pattader, I. Banerjee, H. M. Dixit, K. S. Narayan, *Phys. Rev. Lett.* **2009**,

TH-2671_146153005

DOI 10.1103/PhysRevLett.102.254502.

[19] J. Doshi, D. H. Reneker, *J. Electrostat.* **1995**, DOI 10.1016/0304-3886(95)00041-8.

[20] A. L. Yarin, S. Koombhongse, D. H. Reneker, *J. Appl. Phys.* **2001**, DOI 10.1063/1.1408260.

[21] D. H. Reneker, A. L. Yarin, *Polymer (Guildf).* **2008**, *49*, 2387.

[22] S. Herminghaus, *Phys. Rev. Lett.* **1999**, DOI 10.1103/PhysRevLett.83.2359.

[23] E. Schaffer, T. Thurn-albrecht, T. P. Russell, S. Ullrich, *Nature* **2000**, *403*, 874.

[24] E. Schäffer, T. Thurn-Albrecht, T. P. Russell, U. Steiner, *Europhys. Lett.* **2001**, *53*, 518.

[25] S. Y. Chou, L. Zhuang, L. Guo, *Appl. Phys. Lett.* **1999**, *75*, 1004.

[26] L. Chen, L. Zhuang, P. Deshpande, S. Chou, *Langmuir* **2005**, DOI 10.1021/la047674y.

[27] P. Deshpande, X. Sun, S. Y. Chou, *Appl. Phys. Lett.* **2001**, DOI 10.1063/1.1398616.

[28] P. Deshpande, S. Y. Chou, *J. Vac. Sci. Technol. B Microelectron. Nanom. Struct.* **2001**, DOI 10.1116/1.1414015.

[29] Z. Lin, T. Kerle, S. M. Baker, D. A. Hoagland, E. Schärfer, U. Steiner, T. P. Russell, *J. Chem. Phys.* **2001**, *114*, 2377.

[30] Z. Lin, T. Kerle, T. P. Russell, E. Schäffer, U. Steiner, *Macromolecules* **2002**, *35*, 6255.

[31] K. A. Leach, S. Gupta, M. D. Dickey, C. G. Willson, T. P. Russell, *Chaos* **2005**, *15*, DOI 10.1063/1.2132248.

[32] M. D. Morariu, N. E. Voicu, E. Schäffer, Z. Lin, T. P. Russell, U. Steiner, *Nat. Mater.* **2002**, *2*, 48.

[33] V. Shankar, A. Sharma, *J. Colloid Interface Sci.* **2004**, *274*, 294.

[34] K. Mondal, P. Kumar, D. Bandyopadhyay, *J. Chem. Phys.* **2013**, *138*, DOI 10.1063/1.4773857.

[35] D. Bandyopadhyay, A. Sharma, U. Thiele, D. S. Reddy, *Langmuir* **2009**, *25*, 9108.

TH-2671_146153005

[36] P. S. G. Pattader, I. Banerjee, A. Sharma, D. Bandyopadhyay, *Adv. Funct. Mater.* **2011**, *21*, 324.

[37] J. J. S. Rickard, I. Farrer, P. Goldberg Oppenheimer, *ACS Nano* **2016**, *10*, 3865.

[38] P. Goldberg-Oppenheimer, D. Kabra, S. Vignolini, S. Hüttner, M. Sommer, K. Neumann, M. Thelakkat, U. Steiner, *Chem. Mater.* **2013**, DOI 10.1021/cm3038075.

[39] P. Goldberg-Oppenheimer, P. Kohn, R. M. Langford, U. Steiner, *Small* **2012**, DOI 10.1002/smll.201200194.

[40] N. E. Voicu, M. S. M. Saifullah, K. R. V Subramanian, M. E. Welland, U. Steiner, *Soft Matter* **2007**, DOI 10.1039/b616538a.

[41] H. N. Kim, S. O. Lee, D. J. Kang, J. J. Lee, *J. Nanosci. Nanotechnol.* **2012**, DOI 10.1166/jnn.2012.6335.

[42] X. N. Xie, H. J. Chung, D. Bandyopadhyay, A. Sharma, C. H. Sow, A. T. S. Wee, *J. Appl. Phys.* **2008**, DOI 10.1063/1.2832761.

TH-2671_146153005

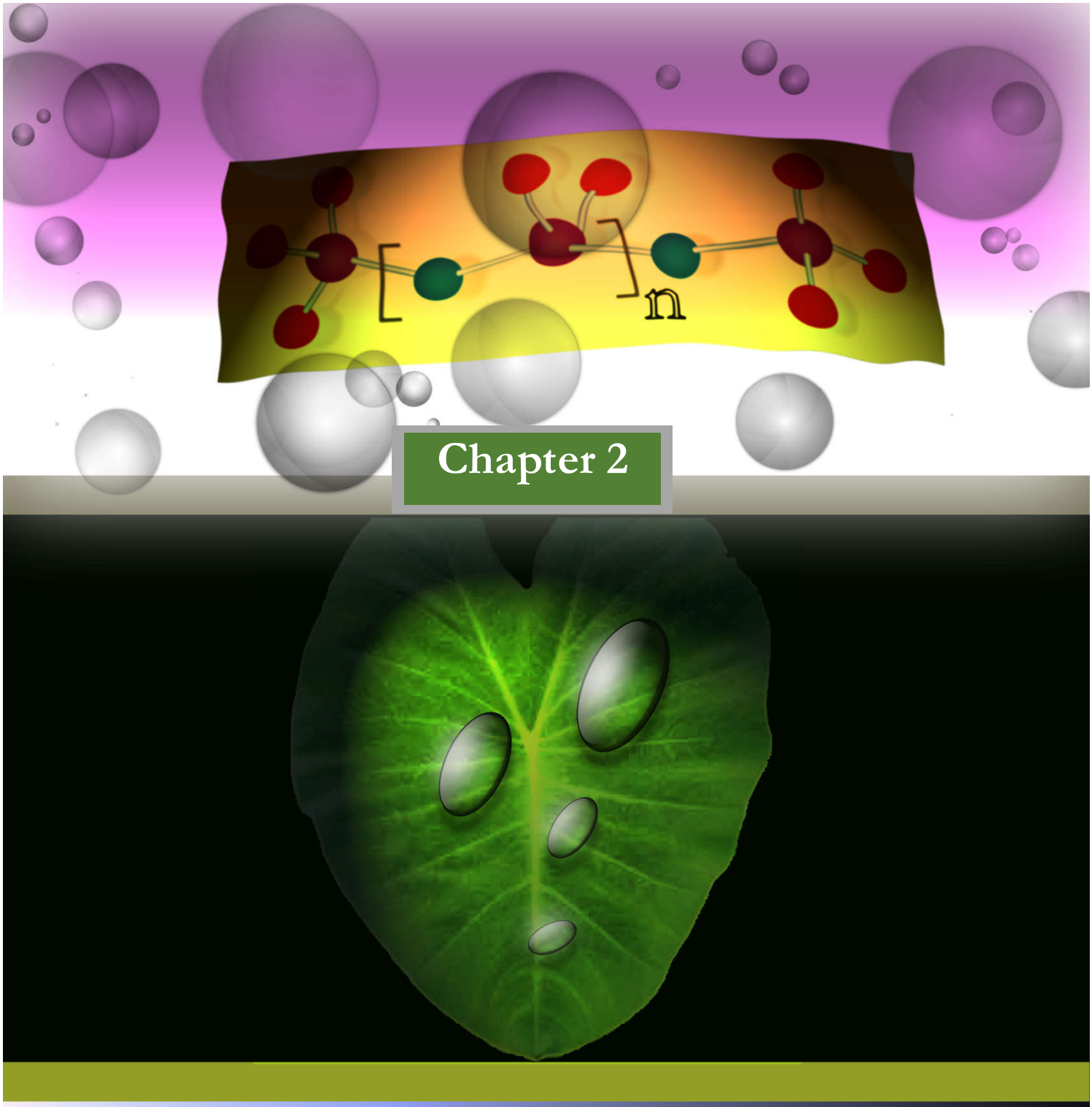

Chapter 2

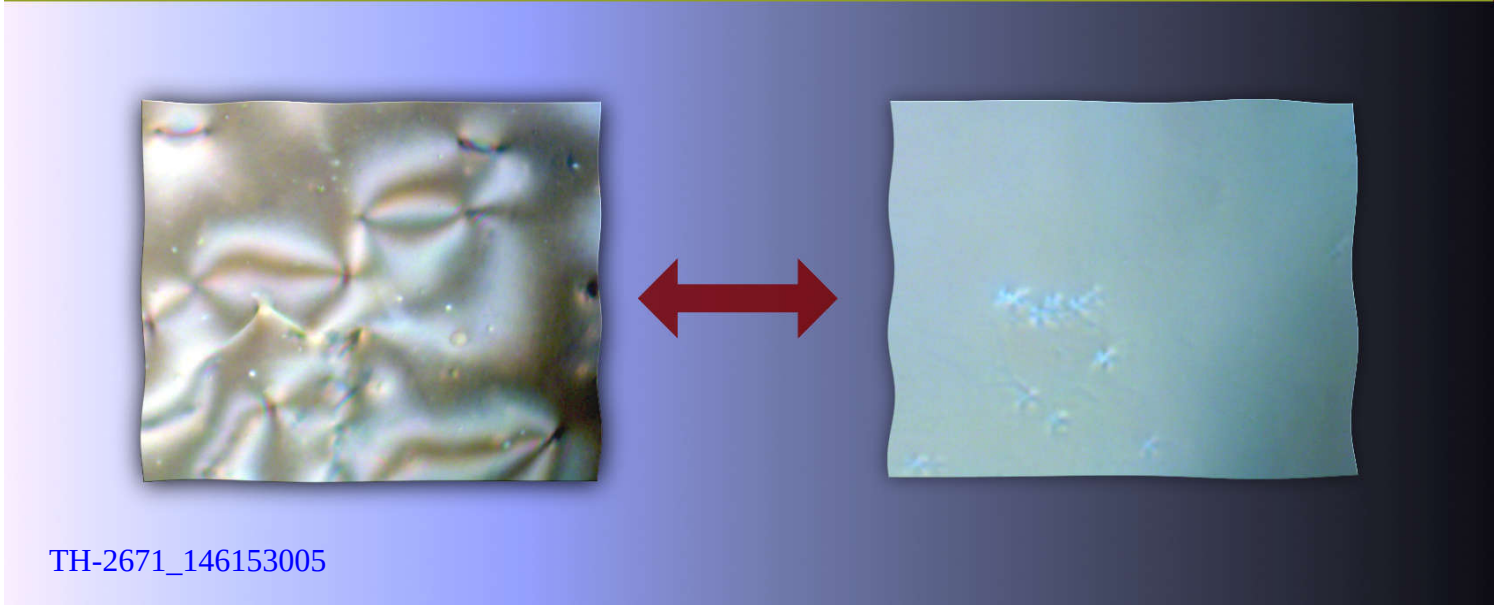

Chapter 2

BACKGROUND THEORIES & TOOLS

2.1. Polymer

Polymers are abundant and are heavily used in science and technological applications. There is a long list of products that we employ on a daily basis that are made up of polymers. These polymers are chain-like long molecules (molecular mass 10^3-10^7g/mol) composed of atomically connected repeating structural units, called monomers. The name "polymer" is derived from the Ancient Greek, πολύς (*polús*, "many, much") and μέρος, (*méros*, "part"). Based on the source material's origin, polymers can be natural (e.g., DNA) or synthetic (e.g., Polyethylene). Polymers also have other classifications based on their structure and mode of polymerization. In other aspects, molecular forces and response to heat treatment categorize polymers into 1) Thermosets, 2) Thermoplastics, and 3) Elastomers. The properties and molecular characteristics of all these types of polymers are different and are well defined. A detailed description of these types would go beyond the scope of this chapter. Among them, elastomers are polymeric molecules for which molecular interactions are the weakest, and the glass transition temperature lies below the room temperature. In this context, elastomers have distinct elasticity that is reversible.

A liquid polymer (based on a hydrocarbon like a butene or propylene) would typically contain up to a dozen monomer units. Thermoplastics such as "Polythene" would contain the order of 1000 monomer units. Commercial Rubbers would typically have 10's thousands of units. When a polymer is cross-linked, such as vulcanized tire rubber or cured epoxy resin, it is just one big molecule of indeterminate length. After a critical chain length, these molecules show entanglement. When crosslinker is added, entanglement increases and free chain mobility reduces. When heat is supplied to this mixture, the elastomer becomes vulcanized (cross-linked). If it is exposed to tremendous heat, it decomposes without fusing.

To define the molecular weight of polymers, two approaches are followed. The total number of units n multiplied by their monomer weight represents the *polymer's molecular weight Mw*. The molecular weight, together

TH-2671_146153005

with the monomer's attributes, determines the physical properties of the polymer. While some properties have a strong dependence on M_w (e.g., melt viscosity), others are only weakly dependent on it (e.g., density). Ideally, one would like to have a *monodisperse* polymer, where molecules should have the same chain length. However, due to the statistical mechanics in the polymerization process, the chains have different lengths. They are *polydisperse*. A polydispersity close to unity indicates a narrow size distribution, which is essential for quantitative analysis of experiments.

2.2. PDMS

Polymers with a controlled molecular organization in all three dimensions are of interest because of their unusual but very accurately adjustable and addressable viscoelastic properties.

The transparent (in the visible region of the spectrum absorption ~ 0.04% and transmission above 95%) elastomer Polydimethilsyloxane (PDMS) Sylgard 184 is routinely used silicone elastomer (*Q-elastomer*) in lubricating agents and waterproofing and heat redundant compounds. It is non-flammable and inert; it is also known as dimethicone. The chemical formula of PDMS is $(CH_3)_3$-Si-O-$[Si(CH_3)_2O]_n$-$Si(CH_3)_3$, where n, the number of repeating $[SiO(CH_3)_2]$ unit of monomer, represents the degree of polymerization. Chemically PDMS falls into the category of silicone oils. The methyl groups attached to the siloxane (-Si-O-) chain are responsible for its thermal stability, hydrophobicity, and transparent nature.

Commercially Sylgard 184 is supplied in two components, a lot-matched base (vinyldimethylsiloxane with a platinum catalyzer) and a curing agent (hydridedimethylsiloxane dione). The addition of the platinum catalyzer helps to the reaction to the functional vinyl group of the monomer base ($SiCH=CH_2$) and the functional hydride group (SiH) that is present in the catalyzer (curing agent), and it results in the curing of the mixture of the two components. This reaction is known as catalytic hydrosilation. The molecular weight of the PDMS's repeating unit is 207.4 g/mol, with an average numeral molecular weight of 27000, a density of 0.982g/mL. The base has a viscosity of 5.1 Pa-s, and when it is mixed with crosslinker in a 10:1 ratio, the viscosity changes to 3.1 Pa-s.

TH-2671_146153005

2.2.1. Mixing the elastomer/oligomer with the curing agent/ reticular agent

a. A required amount of oligomer is measured out into a clean graduated stoppered tubular vial with the help of a plastic disposable graduated dropper. We use the Citizen CX 320 analytical balance for the measurement.

b. The vial is made vertically stand by for a moment such that all the highly viscous oligomer that is adhered to in the container's inner walls to settle down at the bottom to measure the amount obtained.

c. The oligomer and curing agent are usually mixed at a 10:1 ratio for microfluidic applications. The cross-linking concentration must not be so high that the elastic properties hamper as the chains' mobility becomes heavily restricted. We determine the $1/10^{th}$ volume of the amount of oligomer used, and the same volume of crosslinker (curing agent) is pipetted out. Manual mixing (stirring by the pipette tip) of the two components is done until a homogenous phase (prepolymer) is obtained (a disposable plastic cup is used for this step).

d. Extraction of the trapped microbubbles in the mixture (we use a vacuum pump and a vacuum desiccator for this process) is vital. Otherwise, the bubbles will solidify in the cured sample. The vacuum is applied and withdrawn alternately for a total of 10 cycles keeping the elastomer filled cup inside the desiccator with a duration of 3 minutes each. Finally, when all the bubbles disappear, the prepolymer is ready for molding or other microfluidic applications.

e. The curing process is done inside a vacuum oven letting the PDMS rest in a horizontal position overnight at 120 °C to ensure complete curing. The vacuum is used to avoid contamination from solid particles. It is worth mentioning that the baking time may vary when the temperature is modified, or we require a substrate of specific elasticity.

f. If peeling from the mold is needed, then freezing the sample for a few minutes is a good idea that will shrink the PDMS a little, which helps the peeling process. A scalpel blade is useful to get smooth chunk PDMS walls while cutting in one try.

The degassing step (step d) is avoided when we dissolve the PDMS solution in an organic solvent (like n-hexane) to prepare aliquot for spin coating PDMS thin films on solid substrates. To alter the PDMS films'

TH-2671_146153005

viscoelastic behavior, we may vary one of the following parameters: i) concentration of curing agent, ii) curing temperature, and iii) curing time.

2.3. Spin coating

Spin coating is a regular lab procedure of fabricating uniform polymer thin film using centrifugal force and liquid-vapor interface. The relatively inexpensive instrument used for spin coating is known as spin coater. First, the substrate is held to the rotating chuck by suction made by a vacuum pump. The chuck spins around the spinning axis, which is perpendicular to the substrate. The polymer solution is dispensed on top of the substrate surface by a micropipette. When the substrate is rotated at a set frequency (~ 1000–5000 rounds per minute), the excess solution (95%-98%) spins off, and the rest of the solution spreads all over the substrate.

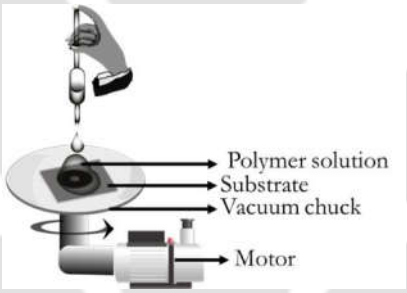

Figure 2.1 Schematic diagram of the spin coating process for the fabrication of flat polymer thin film

During rotation the liquid flows radially to outwards, and consequently, thickness reduces. The spin coating consists of four steps, deposition, spin up, spin-off, and evaporation. The evaporation step runs throughout the spin coating process. After coating, the substrates are baked when the trapped solvents or other low volatile compounds are evaporated. The spin coating generally produces film thickness in micron, which is difficult to obtain in LB technique. One major advantage of the spin coating technique is that it can tune the desired thickness of the polymer film as the film thickness h is related to the controllable parameters as,[1]

$$h = \left(1 - \frac{\varrho_A}{\varrho_{A_0}}\right).\left(\frac{3\eta.m}{2\varrho_{A_0}\omega^2}\right)^{1/3}$$

TH-2671_146153005

where, ϱ_A is the density of the volatile liquid, η is the viscosity of the solution, m is the rate of evaporation, and ω is angular velocity.

The thinning rate of the film is expressed as,[2]

$$\frac{\partial h}{\partial t} = v_h - e_r$$

where, e_r is the constant evaporation rate and v_h is the vertical velocity at the surface of the film.

2.4. Interface

Electromagnetic forces that act between atoms and molecules—the source of all intermolecular interactions—determine the properties of solids, liquids, and gases.

The concept of interface comes when two different condensed (bulk) phases are coexisting on one another. An interface separates them. If a condensed solid phase is exposed to air, it forms solid/air or solid/vapor interface, and in the case of liquid, it will be a liquid/vapor interface. When one of the two bulk phases of an interface is air/vapor, conventionally, it is termed a surface rather than an interface.

In other words, on crossing through a boundary or a region of space, i.e., an interface, a system changes from one phase (liquid/solid) to another (solid/liquid/gas). The thickness of an interface usually ranges from one to several tens of unit (atomic or molecular) diameters.

Whether a surface is hydrophilic or hydrophobic, surface wettability can be assessed by measuring the contact angle, θ, of a sessile water droplet on a smooth surface. The contact angle is a consequence of the surface tensions (γ) at the liquid-vapor (LV), solid–vapor (SV), and solid-liquid (SL) interfaces, as shown by the Young equation,

$$\gamma_{SL} = \gamma_{SV} - \gamma_{LV} \cos\theta$$

TH-2671_146153005

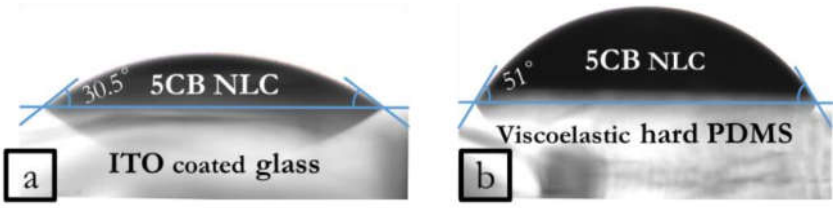

Figure 2.2 The measured contact angles for 5CB on a) PDMS and b) ITO coated glass surfaces. The CA of 5CB on viscoelastic solid PDMS was found to lie within ≈ 51°, indicating lower wettability relative to ITO coated glass (CA ≈ 30.5°).

2.5. Wettability

In the bilayer arrangement of polymers, where one of them is liquid in nature, the wettability plays an important parameter in determining the contact line geometry. When a liquid is introduced on a solid surface, providing the surface is not of dissolving substrate, the liquid spreads. For a drop of liquid resting on a substrate, we get the force balance equation, which is the famous Young equation.

$$\gamma_{SL} = \gamma_{SV} - \gamma_{LV} \cos\theta$$

When $\gamma_{SL} > \gamma_{SV}$, the drop will not spread, and the contact angle(θ) will be larger than 90°. However, if $\gamma_{SL} < \gamma_{SV}$, the drop will spread, minimizing the surface energy and contact angle will be less than 90°.

For a bilayer interface (e.g., liquid-air), the pressure shows a discontinuity across the curvature. The magnitude of this pressure difference is called the capillary pressure P_c, and it is represented as:

$$P_c = \left(\frac{1}{r_1} + \frac{1}{r_2} \right)$$

where, r_1 and r_2 are the radii of curvature of the interface and P_c is higher on the concave area of the interface. The above equation is known as Laplace's law.

TH-2671_146153005

2.6. Nematic liquid crystal

Thermotropic liquid crystals are those for which phase transition occurs in a thermal process. The temperature range of a thermotropic liquid crystal phase lies between the melting point(T_{mp}) and clearing point(T_c). One of the most common mesogenic phases in the thermotropic liquid crystal is the nematic. The word nematic derived from the Greek ('nema' means thread). This term comes from the thread-like topological defects observed in nematics, which are formally called disclinations.[3] Molecular orientation of a typical nematic liquid crystal phase in which the rod-shaped molecules have no positional order; however, they have a long-range orientational order.

2.6.1. Properties of nematic liquid crystal

2.6.1.1. Birefringence

The working principle of liquid crystal display is based on the phenomenon of double refraction of light which is recorded a long time ago (ErusmusBertholinus, Denmark, 1670).

The nematic liquid crystal material that we have used for performing experiments is chemically cyano-compound. The material has two benzene rings in the middle with one hydrocarbon end chain. Due to its typical structure, the molecules in the nematic phase show two values of the refractive index – one along the axis is named the extraordinary refractive index, n_e and the other along the short axis and is called ordinary refractive index n_0. Between these two, the ordinary refractive index n_0 follows the Snells law of refraction. When light rays experience extraordinary refractive index, it travels at a variable speed which depends on the angle between the optic axis and the direction of light propagation. Both of the refractive indices are expressed as:

$$n_e = \frac{n_\perp n_\parallel}{\sqrt{{n_\parallel}^2 \cos^2\varphi + {n_\perp}^2 \sin^2\varphi}}$$

$$n_0 = n_\perp$$

For 5CB, $n_\parallel$ is ~1.73 and $n_\perp$ is ~1.5.

TH-2671_146153005

If we consider uniform planer alignment, then $n_e = n_{\parallel}$ and $n_0 = n_{\perp}$. The intensity of transmitted light coming out of the analyzer is given by:

$$I = I_0 \sin^2 2\varphi \sin^2 \delta/2$$

where, 'I_0' is the light intensity after polarizer. 'φ' is the azimuthal angle (angle between the analyzer and the projection of the optic axis on the same plane). 'I' is the observed intensity at the focal plane of the microscope. The transmitted intensity depends on the orientation of the liquid crystal molecules on the surface. The alignment of liquid crystal molecules thus determines the intensity of transmitted light in the focal plane of the optical microscope. Reversely, the intensity of light can be used to determine the orientation of liquid crystal molecules on the substrate surface (Figure 2.3).

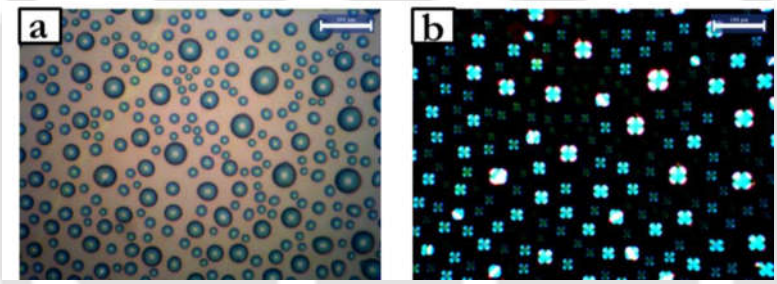

Figure 2.3 Spin-dewetted droplets of 5CB on PDMS thin film a) Optical bright field micrograph in reflective mode and b) Polarized optical micrograph in reflective mode. Scalebar ~ 50 μm

2.6.1.2. Alignment of liquid crystals

The alignment of liquid crystals is an important topic to understand the physics of anisotropic fluids used in display applications. The arrangement of nematic liquid crystal molecules is such that they align parallel to each other. As a result, their mean direction is represented by a directional vector $\hat{n}$. The order parameter is used to quantify the overall orientation of the liquid crystal phase. In the liquid crystal phase, such as nematic, the molecules are aligned along with the director. All the molecules are not parallel to that long molecular axis.

TH-2671_146153005

Most of the molecules are tilted at an angle θ from the nematic director. Mathematically the order parameter, '*S*' can be expressed as:

$$S = \frac{1}{2}\left\langle 3\cos^2\theta - 1 \right\rangle$$

where the symbol $\langle . \rangle$ indicates an ensemble average. For perfectly crystalline solid, $\cos^2\theta = 1$, and hence S = 1. For a completely random system, as in the case of isotropic phase, $\cos^2\theta = \frac{1}{3}$, and S = 0.[4] In a typical nematic phase, the value of '*S*' lies between 0.4 and 0.7, indicating that the molecules have a certain degree of disorder.

In general, there are two approaches to influence the LC alignment within a single architecture:

• Alignment Layer: Either a new material could be investigated, or some properties of the alignment layer could be used to influence liquid crystal molecules. Two basic geometries exist: the planar (or homogeneous) one, where $\hat{n}$ is parallel to the surface, and the homeotropic one, where $\hat{n}$ is normal to the surface, as shown in Figure 2.4.

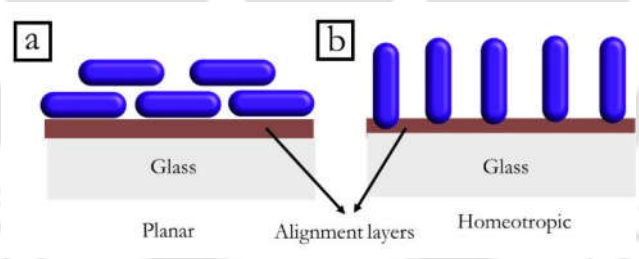

Figure 2.4 Alignment of nematic liquid near a solid surface with suitable alignment layers. In the (a) planar case, the director is parallel to the substrate, whereas it is perpendicular in the (b) homeotropic case.

A simple and widely used process to achieve planar alignment is rubbing. A coated polymer layer (e.g., polyimide, nylon, or polyvinyl alcohol) is deposited on the glass surface and repeatedly rubbed in the same

TH-2671_146153005

direction (about 100 times) with soft tissue (cotton/velour cloth). In this manner, micro-grooves are created in the surface, which aligns the director of the near LC molecules parallel to the direction of rubbing, as depicted in Figure 2.5

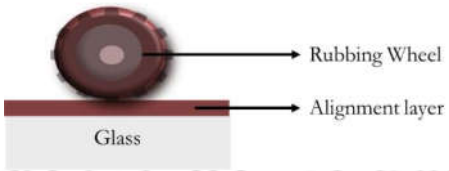

Figure 2.5 Schematic of rubbing-roller in the proximity of a surface where grooves are rubbed, LC molecules align along the direction of the grooves.

It is prominent that rubbing gives a 'pretilt' to the liquid crystal molecules; that is, one end of the molecule is slightly lifted to some degrees. This speeds up and homogenizes the liquid crystal realignment under an electric field (ignoring the occurrence of reverse tilt and reverse twist, which creates different domains).

• Liquid Crystal: This approach involves either synthesizing new materials or modifying existing liquid crystal through the addition of particles such as dyes, nanorods, and nanotubes.

2.6.1.3. Effects of electric and magnetic fields on liquid crystals

Liquid crystals are generally affected by the application of an electric field. The applied electric field produces the polarization $\vec{P}$ (dipole moment per unit volume). It varies linearly with the electric field, but the anisotropic liquid crystal molecules restrict it to have the same values in all directions. $\vec{P}$ is related to $\vec{E}$ by the dielectric tensor $\vec{\chi}$.[5]

$$\vec{P} = \varepsilon_0 \vec{\chi} \vec{E}$$

TH-2671_146153005

$$\begin{pmatrix} P_x \\ P_y \\ P_z \end{pmatrix} = \begin{pmatrix} \chi_{e\perp} & 0 & 0 \\ 0 & \chi_{e\perp} & 0 \\ 0 & 0 & \chi_{e\parallel} \end{pmatrix} \begin{pmatrix} E_x \\ E_y \\ E_z \end{pmatrix}$$

Where ε_0 is the permittivity of free space = 8.854×10^{-12} C/m^2.

Here, in this equation, it is assumed that the orientation of the director along the Z-axis.

2.7. Electrohydrodynamic (EHD) instabilities in PDMS/LC bilayer

This thesis's essential part is the EHD patterning technique, which manipulates interfacial instabilities exhibited by an external electric field. We have studied the EHD instabilities in confined PDMS/LC bilayer.

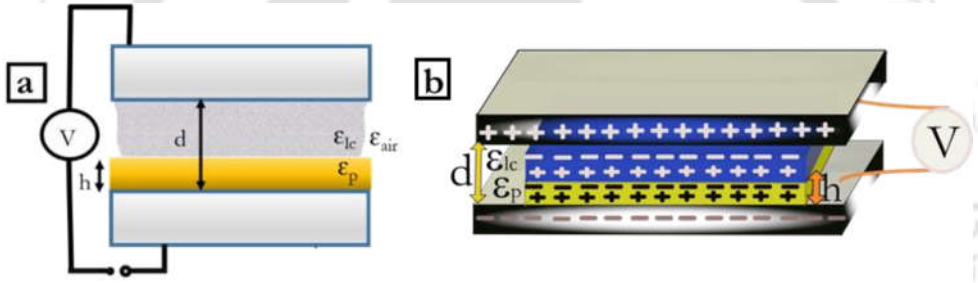

Figure 2.6 Schematics of the experimental processes during the EHD patterning technique under a homogeneous electric field. (a) When voltage is not applied to the system, the interface has only capillary waves. When an electric field is applied, (b) polarization of the dielectric layers occurs, leading to the same charge attraction and opposite charge attraction.

The capacitance of the dielectric can be written in general as: $C_i = \frac{\varepsilon_0 \varepsilon_i A}{d_i}$, where, ε_0 is the permittivity of vacuum, ε_i is the dielectric constant of layer i, and A is the effective surface area.

TH-2671_146153005

The total capacitance for PDMS/LC confined dielectric bilayer can be represented by a series of two capacitors:

$\frac{1}{C}=\frac{1}{C_p}+\frac{1}{C_{lc}}=\frac{h}{\varepsilon_0\varepsilon_p A}+\frac{(d-h)}{\varepsilon_0\varepsilon_{lc}A}$ or, $\frac{1}{C}=\frac{\varepsilon_p d+h(\varepsilon_{lc}-\varepsilon_p)}{\varepsilon_0\varepsilon_p\varepsilon_{lc}A}$, where, ε_p and ε_{lc} are the dielectric constants of PDMS and liquid crystal, respectively. d is the distance between two electrodes, h is the thickness of the PDMS film.

Now, the applied voltage sums up to: $V=E_p h+E_{lc}(d-h)$, where E_p and E_{lc} are the induced electric fields of PDMS and LC layers, respectively.

Considering both PDMS and LC to be perfect dielectrics, we can assume dielectric displacements are equal.

i.e., $D=\varepsilon_0\varepsilon_{lc}E_{lc}=\varepsilon_0\varepsilon_p E_p$.

Replacing this expression to the previous equation yields, $V=\frac{D}{\varepsilon_0}\left\{\frac{h}{\varepsilon_p}+\frac{(d-h)}{\varepsilon_{lc}}\right\}$ or,

$E_p=\frac{V\varepsilon_{lc}}{\varepsilon_p d+h(\varepsilon_{lc}-\varepsilon_p)}$.

The free energy stored in the capacitor at a constant voltage V is given by, $f=f_0-\frac{1}{2}CV^2$ where, f_0 is the free energy stored when no field is applied.

The variation of f with respect to h per unit area of the interface gives the electrostatic pressure at the interface

$p'_{el}=\frac{\partial_h f}{A}=-\frac{V^2}{2A}\partial_h C=\frac{(\varepsilon_{lc}-\varepsilon_p)\varepsilon_0\varepsilon_p\varepsilon_{lc}V^2}{2\{\varepsilon_p d+h(\varepsilon_{lc}-\varepsilon_p)\}^2}$.

From the polymer/air bilayer system, the dominant wavelength of instability at the interface can be written as[6,7] $\lambda_{\max}=2\pi\sqrt{\frac{2\gamma}{-\partial p'_{el}/\partial h}}$.

TH-2671_146153005

Replacing the value of p'_{el} yields $\lambda_{max} = \frac{2\pi\sqrt{2\gamma\{\varepsilon_p d + h(\varepsilon_{lc} - \varepsilon_p)\}^3}}{\sqrt{V^2\varepsilon_0\varepsilon_{lc}\varepsilon_p(\varepsilon_{lc} - \varepsilon_p)^2}}$.

The effect of voltage on λ_{max} can be well understood from the micrographs listed below.

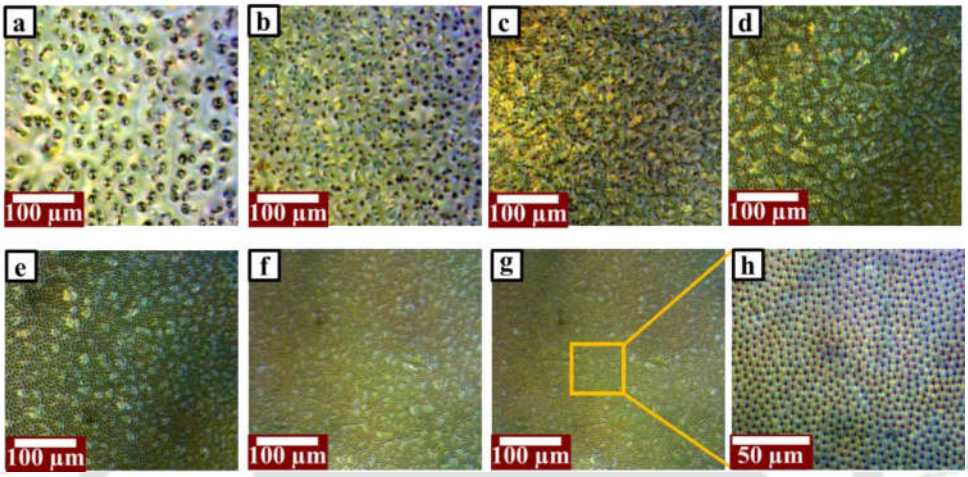

Figure 2.7 Polarized optical microscopic images of viscoelastic hard PDMS-5CB confined bilayer system between two ITO coated glass plates and under DC voltage. Morphological patterns developed on the PDMS (thickness ~3 µm) covered by LC at ramp bias (a) 0-100 V, (b) 100-150 V, (c) 150-200 V, (d) 200-250 V, (e) 250-300 V, (f) 300-350 V, (g) 350-400 V. (h) Identical and uniform PDMS microwells formed at a relatively higher voltage (~ 400 V) under the LC.

2.8. Breath figure

To clean their spectacles, people often breathe out on glasses to make them wet. Then they use linen cloth to clean it. Both the processes are repeated until a clear vision is obtained. When the glasses are wet, some whitish patches developed due to moisture from breath, and it is popularly known as "breath figure." It occurs as the moisture/steam condenses as microdroplets on the colder glass surface. However, on uncleaned glass, the droplets consisting of the breath figure is irregular in size due to particulates and organic contaminants/pollutants present on the glass surface. Repeated cleaning with a linen cloth makes the surface

TH-2671_146153005

smooth, and the corresponding breath figure becomes finer and finer with more uniform and detailed morphology. The microdroplets covering the glass surface is hexagonally closed packed to utilize the maximum surface area with a single layer of condensed water microdroplets. Hexagonal closed pack arrangement is preferred as hexagon has the maximum surface/perimeter ratio among all other polygon.[8]

The same breath figure is unavoidable when a cold lid covers a boiling water pot. The same is seen as unwanted or undesirable fogging in the windshield of a car, which hampers the clear vision by diffracting light. However, this breath figure can be used to fabricate micropatterns on polymer films.[9][10]

2.9. UVO cleaner

A short-range UV radiation (< 300 nm) is being regularly used in depolymerization of polymers, in cleaning metal and glass surfaces, decomposition of surface contaminants(to NO_x+CO_2+H_2O), and hydroxylation of the surface.

The low-pressure Hg discharge ultraviolet (UV) lamp irradiates two types of wavelengths (185 and 254 nm). Each wavelength has different roles for a chemical reaction. 185-nm UV light is absorbed by oxygen, and it dissociates molecular oxygen O_2 into triplet atomic oxygen $O(^3P)$. Triplet atomic oxygen $O(^3P)$ combines with molecular oxygen O_2 and generates ozone O_3.

On the other hand, 254-nm UV light is not absorbed by molecular oxygen, but most organic contaminants and ozone absorb it. It dissociates ozone O_3 and forms molecular oxygen O_2 and singlet atomic oxygen $O(^1D)$. Thus, ozone is destroyed inside the cleaner chamber itself. Singlet atomic oxygen $O(^1D)$ has strong oxidation power, and it reacts with substrate surfaces. In this reaction, the surfaces were oxidized on inorganic substrates such as silicon wafers. In the case of organic materials, chain scission of molecules happens, and organic residue contaminants are gently removed from the substrates as volatile byproduct molecules such as NO_x, CO_2, H_2O, and O_2.

TH-2671_146153005

2.10. Atomic force microscope

Optical microscopes make use of light to achieve a high magnification of the sample. In contrast, electron microscopes use electrons to magnify even further into the atomic structure of materials. Both optical and electron microscope can quickly generate 2D images of a sample surface with the magnification of about 1000X for an optical microscope and 100,000X for an electron microscope. However, these microscopes cannot measure the vertical dimension (z-direction) of the sample, the height (e.g., particles), or depth (e.g., holes, pits) of the surface features.

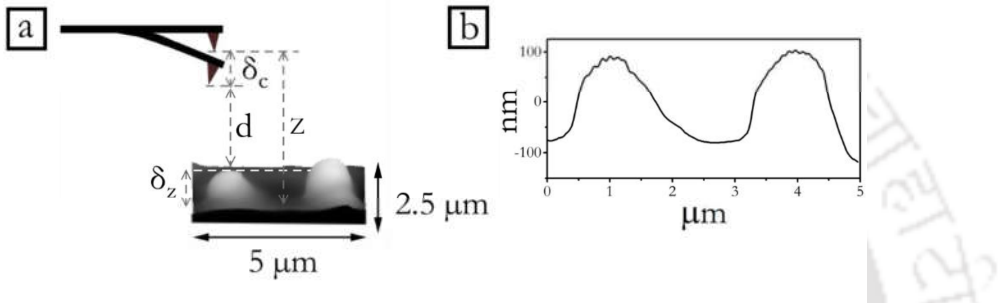

Figure 2.8 (a) The tip sample assembly of AFM. d is the actual tip-sample distance during scan and z is the distance between the sample and the cantilever in rest position. These two distances are different because of cantilever deflection δ_c and sample nonuniformity δ_z. (b)Corresponding line scan of the sample.

Scanning Probe Microscopes (SPM) represent another class of microscopes that allows us to achieve very high magnification images of samples. It was developed as an essential technique to characterize the surface properties of materials, primarily the micro and nano features. This class of microscopes works using a different principle. Imagine yourself in a room that is completely pitch dark so that nothing is visible. Your instinct in navigating in such a place would be to reach out your hands and feel your way around the room. SPMs work in a very similar manner where the world of small tiny objects is revealed by "feeling" around a sample's surface by a sharp sensor.

AFM operates by "contact mode", the instrument lightly touches a tip at the end of a "cantilever" to the sample like a raster measuring attractive or repulsive forces between a tip and the sample (Binnig et aI., 1986). In its

TH-2671_146153005

repulsive scan drags the tip over the sample, some sort of detection apparatus measures the cantilever's vertical deflection, which indicates the local sample height. Thus, in contact mode, the AFM measures hard-sphere repulsion forces between the tip and sample. In non-contact mode, the AFM derives topographic images from measurements of attractive forces; the tip does not touch the sample, and it does not allow the imaging of samples underwater.

The measurement of an AFM is made in three dimensions, the horizontal X-Y plane, and the vertical Z dimension. Resolution (magnification) at Z-direction is normally higher than X-Y. AFMs can achieve a resolution of 10 pm, and unlike electron microscopes, can image samples in air and under liquids. In principle, AFM resembles the record player as well as the stylus profilometer. It should be noted that in a typical AFM scan, the cantilever exhibits a tiny deflection. For example, with a force of 1 nN and a spring constant of 0.5 N/m, the cantilever's deflection would be only 2 nm. A typical silicon AFM cantilever with k between 0.01–100 N/m has a resonant frequency ω of 10–200 kHz.

The AFM can also be combined with various optical microscopes and spectroscopic techniques like Raman/infrared spectroscopy and fluorescent microscopy.

TH-2671_146153005

References

[1] A. Mishra, N. Bhatt, A. K. Bajpai, in *Nanomater. Coatings Fundam. Appl.*, **2019**.

[2] Y. Mouhamad, P. Mokarian-Tabari, N. Clarke, R. A. L. Jones, M. Geoghegan, *J. Appl. Phys.* **2014**, DOI 10.1063/1.4896674.

[3] D. Demus, J. Goodby, G. W. Gray, H. -W. Spiess, V. Vill, *Handbook of Liquid Crystals*, **1998**.

[4] P.-G. de Gennes, J. Prost, *The Physics of Liquid Crystals*, Oxford University Press, USA, **1995**.

[5] T. Scharf, *Polarized Light in Liquid Crystals and Polymers*, **2006**.

[6] P. G. Oppenheimer, *Electrohydrodynamic Patterning of Functional Materials*, **2013**.

[7] S. Harkema, U. Steiner, *Adv. Funct. Mater.* **2005**, *15*, 2016.

[8] F. Nazzi, *Sci. Rep.* **2016**, DOI 10.1038/srep28341.

[9] S. Shojaei-Zadeh, S. R. Swanson, S. L. Anna, *Soft Matter* **2009**, *5*, 743.

[10] L. Li, Y. Zhong, J. Li, J. Gong, Y. Ben, J. Xu, X. Chen, Z. Ma, *J. Colloid Interface Sci.* **2010**, *342*, 192.

TH-2671_146153005

Chapter 3

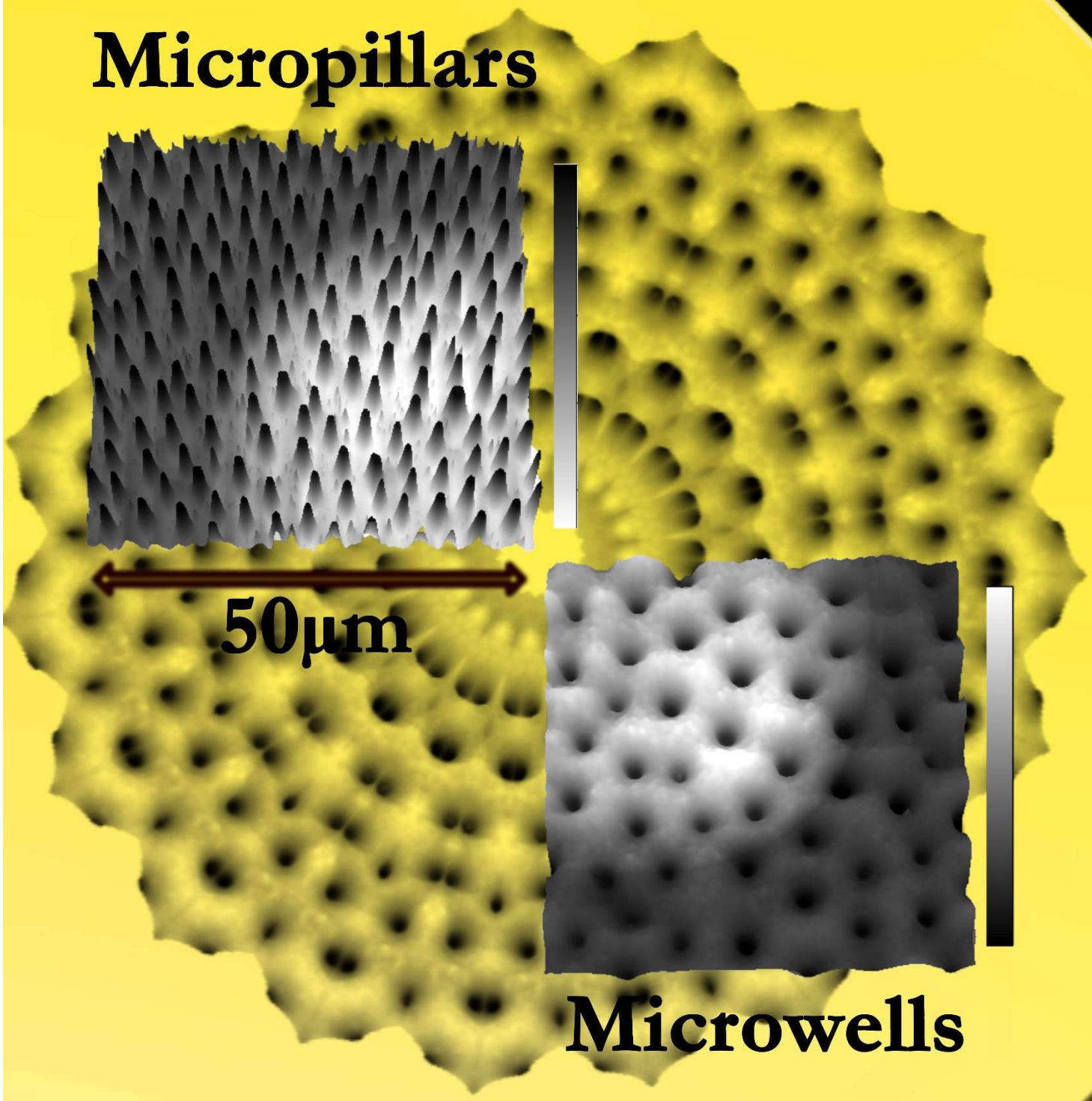

TH-2671_146153005

Chapter 3

ELECTROHYDRODYNAMIC INSTABILITY: EFFECT OF RHEOLOGICAL CHARACTERISTICS ON THE MORPHOLOGICAL EVOLUTION OF LIQUID CRYSTAL-POLYMER INTERFACE

Abstract

Electrohydrodynamic instability, in a polymer-air or polymer-polymer bilayer settings, gives rise to the formation of the ordered micro-pillars or micro-wells at the initial planar interface. It is well known that the complex interplay among the controlling parameters such as the intensity of the electrostatic field, film thickness, interfacial tension, and dielectric constants of the layers determine the morphology of the interface. In this report, for the first time, experimentally it is shown that rheological property of the lower polymer layer (here polydimethylsiloxane (PDMS)) has a significant influence on the morphological evolution. We probe the kinetic time scale of the evolution by inducing rapid destabilization of the interface due to the high dielectric contrast between two layers (liquid crystal – PDMS) and reduced interfacial tension. At this time scale, it was demonstrated that micropillars are formed for thin viscoelastic "soft" PDMS film, whereas microwells were observed for viscoelastic "hard" film in similar settings. A transition from micropillar to microwell was observed for viscoelastic "soft" film when the thickness of the film increased from ~ 4 μm to 11 μm. Based on this observation, by controlling the rheological properties, different patterns were developed from similar templated PDMS substrates.

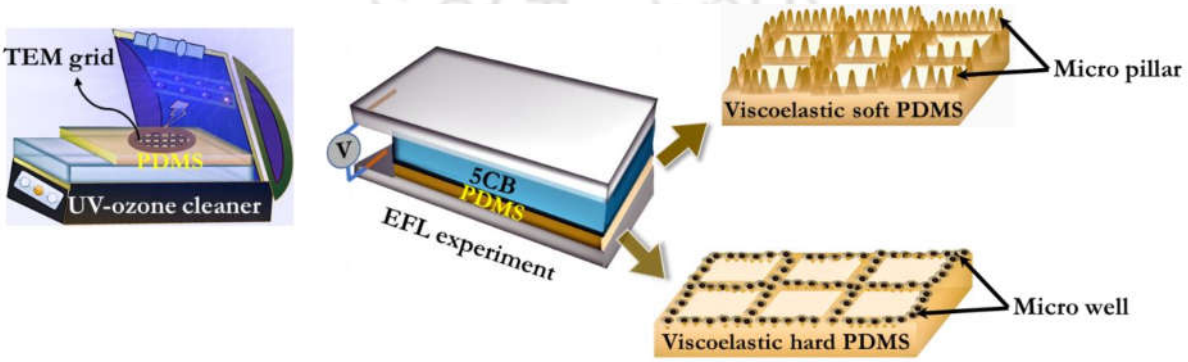

This work is published in *Bull Mater Sci* **43,** 169 (2020).https://rdcu.be/b5Qr6

TH-2671_146153005

3.1. Introduction

The formation of micro/nanopatterns from a thin polymer film has scientific and technological importance. It has many potential uses in electronics,[1–3] material industries and micro/nano-optics,[4,5] microfluidics,[6,7] biomedical applications,[8,9] and so on. Controlling the organisation of the patterns in a soft polymer can be achieved by various lithographic techniques such as photolithography, electron beam lithography, Nano Imprint Lithography (NIL),[10] soft lithography,[11] Capillary Force Lithography (CFL),[12,13] etc. Most of the soft lithographic processes demand the control of the rheological properties of the polymer film. Initially, in the pattern formation stage, the viscosity of the polymer has to be low enough to facilitate the flow of the polymer, and at a later stage, the polymer needs to be hardened to freeze the pattern formed[14,15]. The thermoplastic polymers such as polystyrene (PS), poly(methyl methacrylate) (PMMA), etc. become liquid-like low viscous materials when heated above their glass transition temperature and hence satisfy the requirement of the pattern formation stage in NIL, soft lithography or CFL. Upon cooling to the room temperature, these polymers become hard again and freeze the patterned morphology.

It has been reported earlier that when a charged thermoplastic film is softened by raising the temperature, the surface undergoes wrinkling deformation beyond a critical surface charge density[16]. Later, electric field induced instability of thin viscoelastic polymer film is well exploited to create patterns. In classical experiments of electric field induced lithography (EFL), an air-polymer bilayer arrangement is placed in between two parallel plate electrodes emulating a capacitor and is subjected to an electric field. The planer air-polymer interface reorganises into micro/nano columns or wells to minimise the global energy of the system. This phenomenon happens when the destabilising electrostatic force at the interface is high enough to overcome the stabilising surface tension and/or restoring elastic force and induce interfacial perturbation. Eventually, this perturbation grows following a dominant wavelength and leads to the topographically patterned landscape at the interface. Later, different variations of this classical EFL are investigated experimentally[17–20] as well as in numerical framework[21–23]. For viscoelastic polymer, by controlling the extent of crosslinking, one can control the viscous and elastic component[24] of the polymer. This gives a tunable tool to pattern a viscoelastic polymer in significantly viscous

TH-2671_146153005

state and to freeze the pattern by making it predominantly elastic, by inducing more crosslinking among the monomers or oligomers[15]. This enhancement of crosslinking can be induced either by raising the temperature or by UV curing, depending on the type of the polymer used. The effect of rheological properties of a viscoelastic polymer film on controlling the pattern height, due to the partial relaxation of the applied stress, was reported in case of transient imprint lithography[25]. The wavelength (λ) of the EFL instability in the viscoelastic liquid-like film (i.e., storage modulus (G') < loss modulus (G'')) is reported to be dependent on the applied electric field, film thickness and the interfacial tension nonlinearly and is the long wave in nature. Whereas, for a viscoelastic solid like film, i.e., when $G' > G''$, the film obeys short wave length-scale of deformation and beyond a threshold applied electric field, the wavelength is only linearly dependent on film thickness ($\lambda \propto 4h$), the scaling of which is similar to that of elastic contact instability observed in debonding of an elastic adhesive from a rigid surface. In both the viscoelastic liquid-like regime as well as in solid-like regime, it was found that the wavelength (λ) of the morphology is insensitive to the rheological properties of the polymer film except the narrow transition regime from liquid-like to solid-like film[26].

It is also reported that in a bilayer system, undergoing EFL, if the dielectric constant of the relatively thin bottom layer is smaller than that of the thick upper layer, holes are formed within the bottom layer.[27] This was predicted numerically as well by solving the nonlinear kinematic equation for the evolution of the interface.[28] Numerical study of Wu et al. also suggested that hole pattern is only possible when the ratio of dielectric constants (ε) of lower film to that of the upper film is less than unity, and for a fixed ratio of ε, there exists a critical film thickness below which pillars instead of holes will be formed.[28] Hence, the EFL of soft viscoelastic polymer with different controlling parameters provides tunable and rich morphological evolution, which may end up in patterned polymer thin film with potential applications.

In the view of the above discussion, in this article, we report an experimental investigation of EFL of viscoelastic liquid-like polydimethylsiloxane (PDMS) films with two distinct rheological characteristics. In the first case, the $G' \approx G''$ and is in the range of ~ 60 Pa at a frequency of 1 rad/s with G' marginally higher than G'' and in the

TH-2671_146153005

second case, $G' << G''$, having G' 100 times smaller than G'' which is ~ 1.5 Pa at a frequency of 1 rad/s. From now on, we will refer the first type of sample as the "hard" sample and the second one as "soft" sample respectively, although both types of samples are in liquid-like regime (with the hard sample, marginally close to the liquid-solid transition regime) as defined in reference[26]. Instead of the classical air-polymer bilayer arrangement, we have used nematic liquid crystal (NLC) – polymer bilayer for the EFL experiments (Figure 3.1a and 3.1b). The bilayer was sandwiched between two transparent Indium Tin Oxide (ITO) coated glass slides with the help of spacers and for different thickness of the hard and soft viscoelastic PDMS films, the experiments were performed. In these experiments, we have chosen 4-Cyano-4'-pentylbiphenyl (5CB) as the upper NLC layer to induce small length and time scale of destabilisation [29] due to the smaller interfacial tension of 5CB-PDMS ($\gamma_{PDMS/LC} \approx 4.5$ mN/m)[30] compared to the air-PDMS ($\gamma_{PDMS/Air} \approx 20$ mN/m)[31] and very high dielectric contrast between the two layers (dielectric constant of nematic 5CB is, $\varepsilon_{\parallel}$ =19.7,[32] whereas, that of PDMS is $\varepsilon \sim 2.65$ [33]). In this chapter, we have shown that within a very small time scale of destabilisation, which is kinetically controlled, the morphology of the interface is also dependent on the rheology of the viscoelastic film.

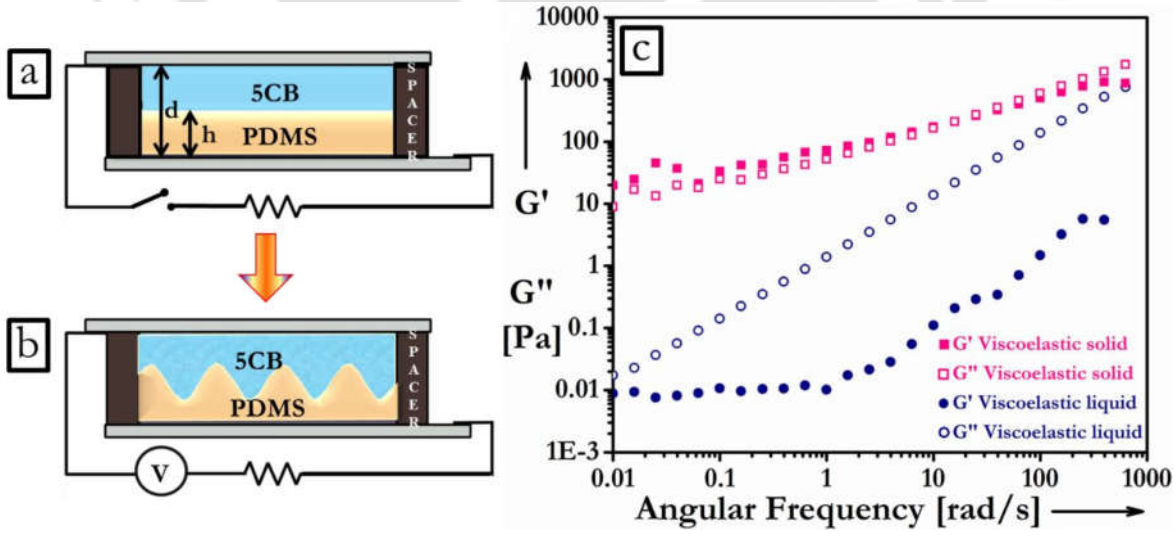

Figure 3.1 Schematic of the experimental set-up (a, b). 5CB – PDMS bilayer is sandwiched between two ITO electrodes, separated by spacers. Upon application of the voltage, the 5CB-PDMS interface destabilise. (c) Storage

TH-2671_146153005

modulus (G') and Loss modulus (G'') as a function of angular frequency depicts viscoelastic "hard" PDMS has significantly higher storage modulus compared to viscoelastic "soft" PDMS.

3.2. Experimental

3.2.1. *Materials*

Indium tin oxide coated glass plates (ITO, 10Ω /sq.) were obtained from Macwin India, India. A common poly (dimethylsiloxane) (PDMS) precursor having cross-linkable oligomer and crosslinker was procured from Dow Corning, Mumbai, India (SYLGARD 184 kit). Analytical grade solvent n-hexane was procured from Sisco Research Laboratories Pvt. Ltd., India. 4-Cyano-4'-pentylbiphenyl nematic liquid crystal was obtained from Sigma-Aldrich (99.99% pure, 5CB NLC, N-I transition temperature ~ 34.5 ± 0.5 °C). All of these chemicals were used without any further purification.

3.2.2. *Methods*

3.2.2a PDMS substrate preparation

Viscoelastic PDMS thin film substrates were prepared on properly cleaned 15 mm × 15 mm ITO coated glass substrates (bottom electrode) by spin coating the PDMS precursor solution. For viscoelastic soft films, 1% (weight percentage) crosslinker and for viscoelastic hard films 2% crosslinker was mixed with oligomer. This sticky semisolid mixture was then dissolved in n-hexane to prepare a homogeneous solution. The thickness of the spin-coated PDMS film was controlled by varying the concentration of the oligomer-crosslinker mixture in n-hexane. Before spin coating on a cleaned ITO surface, provision for spacers and electrical contacts were ensured by covering the ITO electrode with magic tape(Scotch Magic Tape-810 series, 3M India Ltd). After spin-coating at a spin speed of 2500 rpm for 120 s, the magic tape was removed, and the samples were baked in a vacuum oven. For viscoelastic hard samples, the baking was done at 120 °C for 12 h, whereas for the soft samples, the baking temperature was maintained at 80 °C for 1 h. After removing the samples from the vacuum oven, they were cooled to room temperature before performing the EFL experiments. The thickness of the PDMS film was

TH-2671_146153005

measured with a stylus contact profilometer (Dektak Veeco). The rheological properties of the viscoelastic hard and soft samples were measured using cone and plate assembly (Physica MCR 301, Anton Paar). The storage G' and loss modulus G'' of the samples were plotted against the frequency of the oscillation of the cone and is shown in Figure 3.1c.

3.2.2b Electric Field-induced Lithography (EFL) experiment:

After fabricating the PDMS sample on the bottom ITO electrode, a commercial hard polyimide tape having ~ 35 μm thickness was fixed to the uncoated part of the ITO. This polyimide tape served the purpose of the spacers. A drop of 5CB was deposited on the PDMS film, and a bare cleaned ITO glass slide was placed carefully over the spacers with the conducting side facing 5CB layer so that no air bubble was trapped inside. This arrangement formed a parallel plate capacitor geometry with 5CB-PDMS film bilayer sandwiched between two ITO coated glass slides (Figure 3.1a and 3.1b). The copper wires were attached to the two ITO plates with the help of copper tape and clips. These wires were connected to a DC voltage source (SES Instruments Pvt. Ltd., EHT-II) and the voltage was applied at a ramping speed of ~2 V/s until a potential of 300 V (until otherwise stated) was reached. The morphology was observed and recorded using an optical microscope (Leica DM2500 M) equipped with a CCD camera (Leica DFC450 C). The temperature during the EFL experiments was maintained at 23 °C, at which the 5CB remained at nematic state.

3.2.2c Pattern fabrication using templated substrate:

Initially, the viscoelastic hard and soft film was prepared following the procedure described in section 2.2a. To pattern the homogeneous and uniform PDMS film, a TEM sample holder (CF300-Cu, Carbon film on Cu 300 sq. mesh, Electron Microscopy Sciences), having box-grid pattern was placed on the PDMS substrate to use it as a mask, and the arrangement was kept inside the UV Ozone chamber (Novascan PSDP Pro system) for 1 h. The open box pattern has a dimension of (55 μm × 55 μm) and covered grid region has a width of (25 μm). Due to UV Ozone (UVO) exposure, the silicone was oxidised to silica and formed a hard, rigid crust on the open box area of the PDMS surface[34][35]. The covered grid area maintained the softness (rheological properties) of the

TH-2671_146153005

original viscoelastic film. Here a point to be noted that in the viscoelastic soft films, while placing the TEM grid, a significant amount of the polymer material was dislodged from underneath the mask due to the slightest pressure applied. The pressure reduced the initial film thickness underneath the mask. This reduction of film thickness happened because of the significantly low viscosity and low elastic modulus of the soft film.

3.2.2d Characterisations

To investigate the morphology of the PDMS thin film after the EFL experiment, first, the top ITO electrode was removed carefully. Excess 5CB NLC was then removed using a filter paper without disturbing the morphology developed on the PDMS surface. To petrify the morphology on the PDMS surface, the film was then exposed in UVO for 20 min, which imparts a stiff silica layer on the film. Then the substrate was washed with DMSO (Merck, India) and dried under the nitrogen flow. DMSO, a polar aprotic solvent, removed 5CB molecules preferentially without swelling the PDMS[36]. As the deformed PDMS surface became hard and rigid due to the silica crust formation, it facilitated the characterisation of the surface morphology using an Atomic Force Microscope (AFM; Innova Iris, Bruker-Icon Analytical Equipment).

3.3 Results and Discussion:

3.3.1. *Length scale and morphology:*

As mentioned earlier, ~ 5 µl of 5CB was placed on viscoelastic PDMS thin film, coated on a clean bottom ITO electrode, and sandwiched by another top ITO electrode (Figure 3.1a). These two electrodes when connected with a voltage source, due to the electric field generated, the nematic 5CB domains tried to align its directors towards the direction of applied electric field and thus, Fréedericksz phase transition took place[37,38]. At this point, it should be noted that the 5CB molecules maintained its homeotropic anchoring on the PDMS surface, i.e., the long axis of the 5CB molecule remained perpendicular to the PDMS surface[39,40]. Whereas the 5CB molecules anchored in planner fashion on ITO surface at the top, i.e., 5CB molecular long axis remained parallel to the ITO surface[41]. Apart from these two boundaries, the bulk of the 5CB molecules aligned towards the direction of the electric field, leading to a director gradient near the top ITO electrode. At this point, Maxwell stress, generated at

TH-2671_146153005

the interface of LC-PDMS, induced destabilisation by overcoming the stabilising interfacial tension and restoring elastic force. This destabilisation grows within a very short time and leads to the formation of micro/nanostructures at the interface.

In all these experiments, the separation distance (d) between two ITO electrodes was maintained at 35 μm using the polyimide spacers. The PDMS film thickness (h) was varied by choosing proper condition during spin coating as described in the experimental section. The length scale of the morphological evolution was found to be governed by the short time kinetics, and the fastest growing wavelength (λ_{max}) survived. Although the final morphology was governed by the global energy minimisation of the system, i.e., thermodynamically favourable energy state, here we focused on the short time scale morphological evolution of the interface.

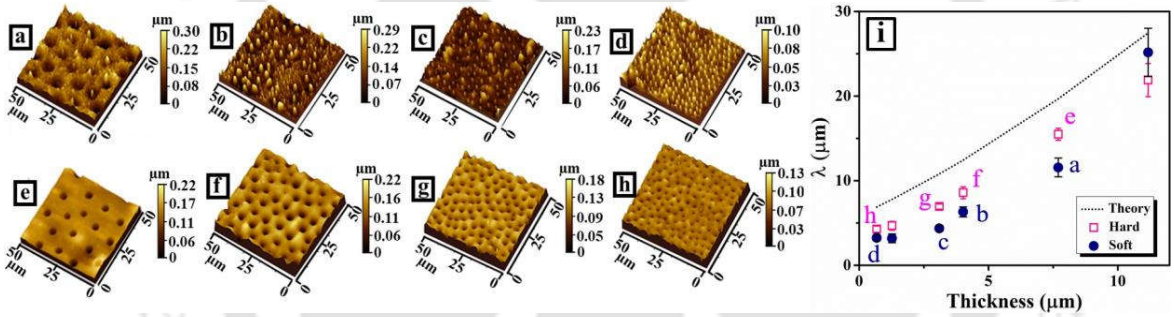

Figure 3.2 AFM images of viscoelastic soft (a-d) and hard (e-h) PDMS film after the EFL experiment. The film thicknesses for (a), (e) are of 7.7 μm; (b), (f) are of 4 μm; (c), (g) are of 3 μm; (d), (h) are of 0.7 μm. (i) Characteristic wavelength (λ) of the morphology as a function of film thickness. Black dotted line represents estimated λ from equation (1). Open pink square (□) and filled dark blue circle (●) represents experimental data points for hard and soft film respectively.

Upon application of electric field, LC-PDMS interface was readily destabilised, and viscoelastic 'hard' samples gave rise to the formation of microwells in the PDMS film irrespective of the film thickness. Whereas, micropillars were formed when thin viscoelastic 'soft' PDMS samples (h ranging from ~ 680 nm to ~ 4 μm) were used. On relatively thick viscoelastic soft film in the range of ~ (4 μm - 11 μm), an intermediate mixed morphology of micropillars within microwells was observed (Figure 3.2). Figure 3.2i shows the wavelength, λ_{max} (i.e., average

TH-2671_146153005

centre to centre distance) of the microwells or micropillars against the PDMS film thickness. Theoretical estimation of λ_{max} for an isotropic bilayer system is well established[15,22,26,42–44]. Although the 5CB layer is anisotropic and molecular fluctuation may play a significant role, in the present scenario, we resort to a very simplistic approach assuming LC and PDMS are both Newtonian fluid, and the continuum approximation is applied to the system. Hence, although the LC molecule is anisotropic, we will assume that nematodynamic has a negligible effect on the morphological evolution and λ_{max} can be estimated as:

$$\lambda_{max} = \frac{2\pi\sqrt{2\gamma\{\varepsilon_2 d + h(\varepsilon_1 - \varepsilon_2)\}^3}}{\sqrt{V^2\varepsilon_0\varepsilon_1\varepsilon_2(\varepsilon_1 - \varepsilon_2)^2}} \quad (1)$$

Where V is the applied bias voltage, ε_0 is the dielectric permittivity of the vacuum (8.854×10^{-12} F/m), $\varepsilon_1, \varepsilon_2$ are the dielectric constants of 5CB and PDMS respectively, γ is the interfacial tension at PDMS -5CB interface. From Figure 3.2i, it is evident that equation (1) (represented by the black dotted line) successfully predicts the trend as well as the magnitude of the λ_{max} with experimental value marginally lower than the theoretical estimation. This may be due to the simplistic approach we have adopted by neglecting the anisotropic behaviour of the upper LC layer. At this juncture, another interesting point to note is that, although the spatio-temporal average direction of the NLC molecules aligns with the applied electric field, due to the thermal noise, they always fluctuate locally. This imparts local director fluctuations along with the physical properties associated with the anisotropic nature of the molecules. The incident is reminiscent of noise activated escape from a trapped state due to attenuated effective energy barrier[45–49]. The local fluctuation of the NLC molecules, thus diminishes the effective energy barrier of destabilisation and may results in the marginally smaller wavelength than predicted by the equation (1).

In the viscoelastic hard sample, it was observed that the size of the microwell and the wavelength had low standard deviation and narrow distribution. Whereas, for the soft viscoelastic sample, the distribution of the size and wavelength of the micropillars were relatively wide, except at the very low thickness of the film. In fact, for a soft film having the thickness of ~ 4 μm (Figure 3.2b), the size distribution of the micropillars was bimodal in nature.

TH-2671_146153005

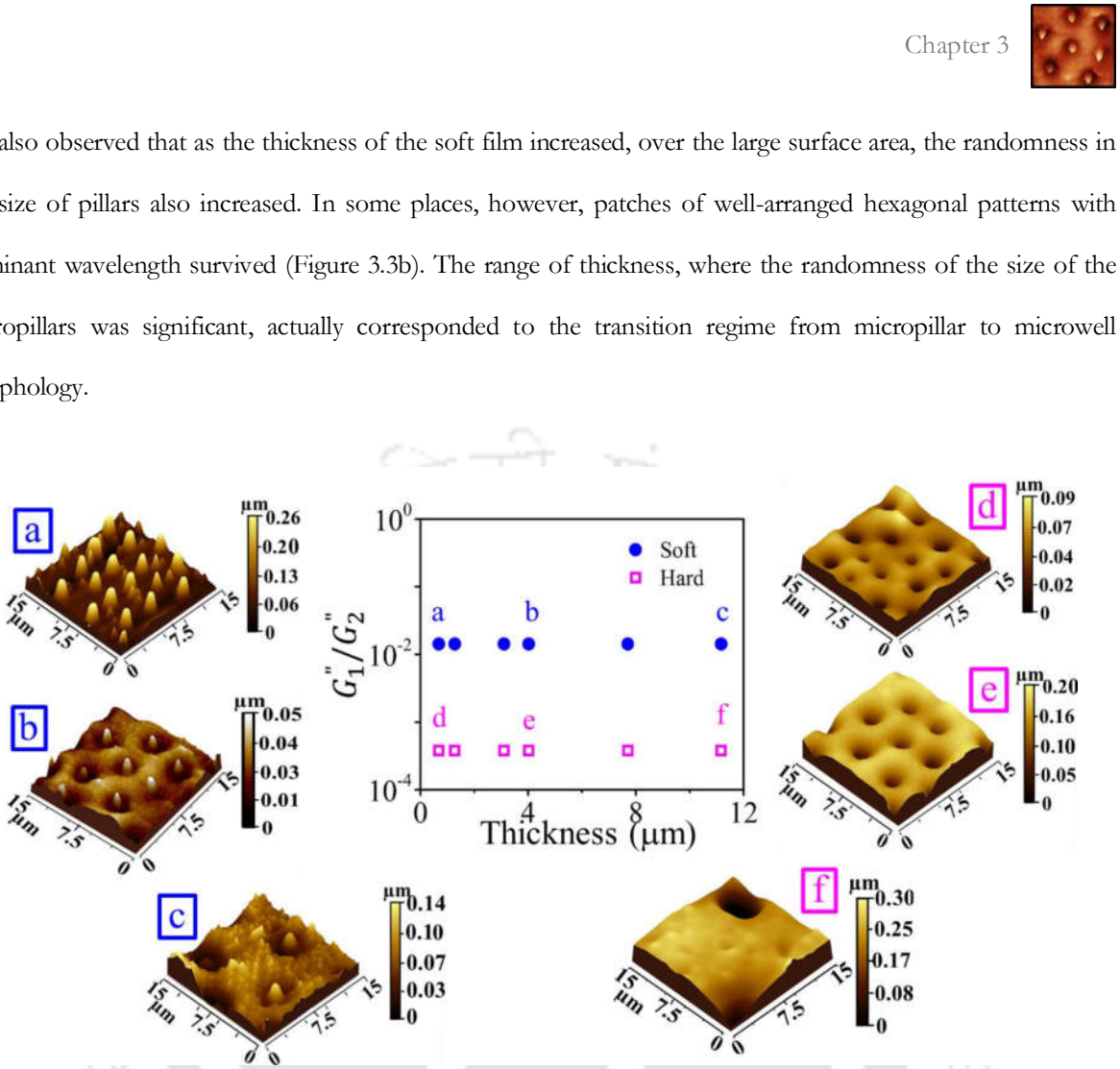

We also observed that as the thickness of the soft film increased, over the large surface area, the randomness in the size of pillars also increased. In some places, however, patches of well-arranged hexagonal patterns with dominant wavelength survived (Figure 3.3b). The range of thickness, where the randomness of the size of the micropillars was significant, actually corresponded to the transition regime from micropillar to microwell morphology.

Figure 3.3 Predominantly micropillar (soft PDMS film, a, b, c) and microwell (hard PDMS film, d, e, f) morphology after EFL experiments. (g) depicts the ratio of loss moduli of the LC layer to that of lower PDMS film against film thickness. The AFM images (a-f) were identified in the figure (g), which portray the morphological variation as a function of film thickness and the ratio of loss moduli.

Numerical simulation by Wu et al.[28] demonstrated that irrespective of the elastic modulus of the polymer film, if the upper layer has higher dielectric permittivity compared to the lower polymer layer, the later must have microwell instead of pillar for a film thickness larger than a critical value. Here, we have experimentally established that indeed there exists a critical film thickness below which pillar structure survives but rheological properties (G' and G'') of the film also influence the morphology of the film (Figure 3.3). The ratio of loss moduli of upper

TH-2671_146153005

LC layer (G_1'') to that of lower PDMS film (G_2'') for both hard and soft films were plotted as a function of film thickness and the morphology (i.e., micropillar or microwell) of the film after the EFL experiment was identified in Figure 3.3g. The transition regime from microwell to micropillar might be influenced by the rheological property of the film and shifted towards the much lower film thickness regime in case of the hard film having relatively high G'' value. To verify this, we performed one experiment with hard PDMS film having a thickness as low as 26 nm. Surprisingly, at this low thickness also, we found microwells instead of micropillars in the EFL experiments.

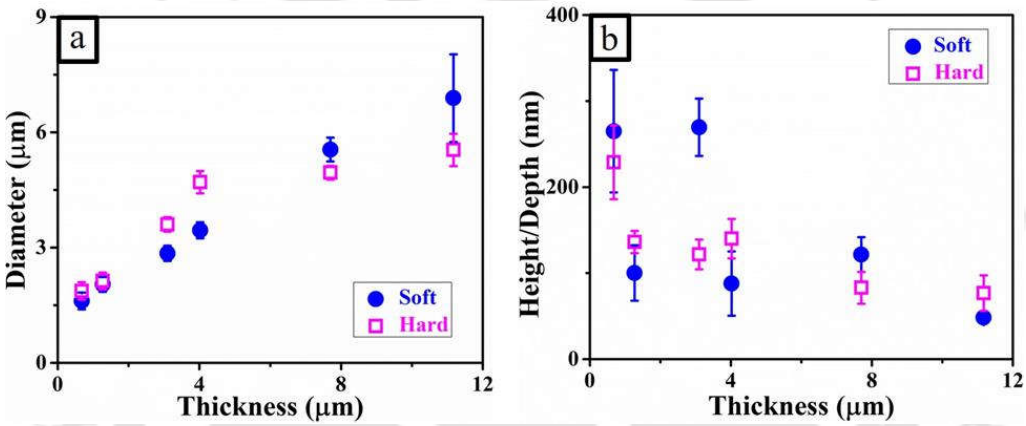

Figure 3.4 Variation of feature (micropillars/microwells) diameter (a) and height (of micropillars) / depth (of microwells) (b) as a function of film thickness. Open pink square (□) and filled blue circle (●) represents experimental data points for hard and soft film respectively.

Figure 3.4 shows the feature diameter (3a) and the height (depth) (3.4b) of the pillars (wells) formed by EFL for both the hard and soft films. The diameter and the height/depth of the feature were measured from the AFM images. Alt-hough the feature size (diameter) increases from ~ 1.5 μm to ~ 7 μm monotonically with the film thickness (~ 680 nm to ~ 11 μm), the height/depth are scattered within the range of ~ 300 nm to ~ 30 nm resulting high standard deviation.

TH-2671_146153005

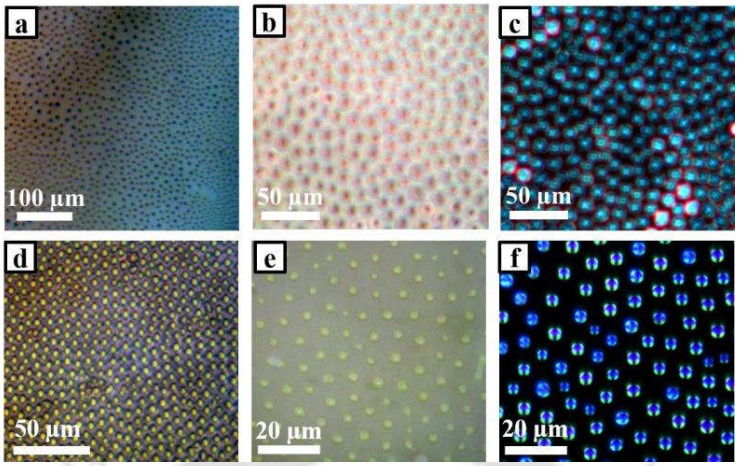

Figure 3.5 Morphology as observed in viscoelastic soft (a-c) and hard (d-f) PDMS film. (a, d) and (c, f) are the polarised optical micrographs (POM) during EFL experiments and after the EFL experiments respectively. (b, e) are the bright field image after the removal of the excess LC. (b, c) trace of LC adheres to the micropillars, which acts as the pinning sites while removing excess LC. (e, f) LC filled microwells after removal of the excess LC.

Figure 3.5a and 3.5d depict the polarised optical micrograph (POM) of the LC-PDMS interface during the EFL experiment with viscoelastic soft and hard PDMS sample, respectively. After the EFL experiment, the top electrode was removed carefully, and the excess LC was soaked with filter paper, leaving the trace of the LC on the sample. Corresponding bright-field images (Figure 3.5b, 3.5e) and POM (Figure 3.5c, 3.5f) of the soft (Figure 3.5b, 3.5c) and hard sample (Figure 3.5e, 3.5f) are shown in Figures 3.5.

In the next sections, we demonstrate the fabrication of two different patterned multi-length scale morphology by tuning the rheological properties of the PDMS film.

TH-2671_146153005

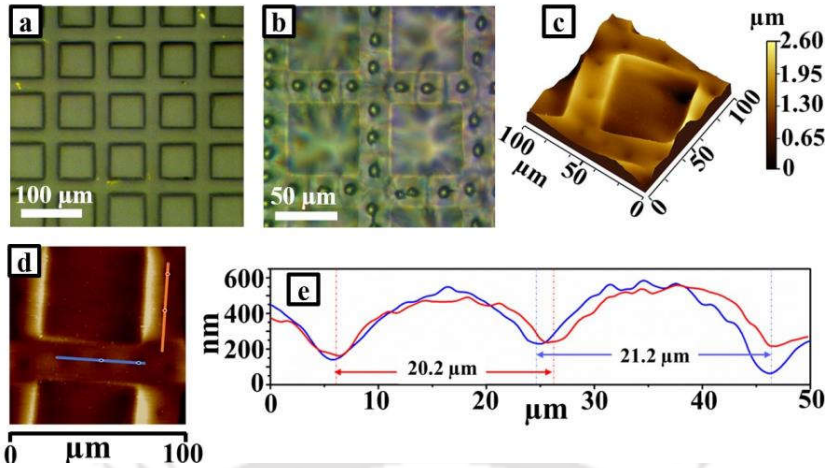

Figure 3.6 (a) Optical micrograph of the templated viscoelastic hard PDMS film (thickness ~11 µm). The box area remains undeformed during EFL experiment due to the formation of hard silica crust while exposed to UVO and array of single microwell is formed in the grid area (b). (c)-(d) Atomic force micrograph showing topography and the line scans (e) depicting the surface profile and the wavelength of the morphology.

3.3.2. *Templated pattern with the viscoelastic hard film:*

We used a templated PDMS substrate to fabricate multi-length scale patterns using EFL. A viscoelastic hard sample on ITO bottom electrode was masked with a copper TEM sample holder and kept under UV ozone chamber for 60 min. TEM sample holder has open square box (55 µm × 55 µm) pattern separated by the copper grid (width W = 25 µm). Due to the exposure with UV ozone, the open box area of PDMS surface was transformed into stiff and rigid SiO_2 crust leaving the unexposed covered grid area as the unmodified viscoelastic sample. Once the chemical modification of the open box area was achieved, the TEM sample holder was removed. On top of this modified templated PDMS substrate, 5CB was placed, and another top ITO coated glass slide was placed as the top electrode, and the usual EFL experiments were performed. A viscoelastic hard PDMS film with thickness ~ 11 µm underwent such EFL experiment led to the formation of an array of single microwell within the unexposed and unmodified grid area of the PDMS sample (Figure 3.6). The UVO exposed square box area remained flat and undeformed due to its high rigidity. As the width of the unmodified PDMS surface (covered grid area), $W(\approx 25\ \mu m)$, follows the relation $\lambda_{11} < W < 2\lambda_{11}$, only an array of single microwell was observed.

TH-2671_146153005

Here, λ_{11} ($\approx$22 μm) is the natural wavelength of the destabilisation of a flat homogeneous viscoelastic hard sample having a thickness of 11 μm.

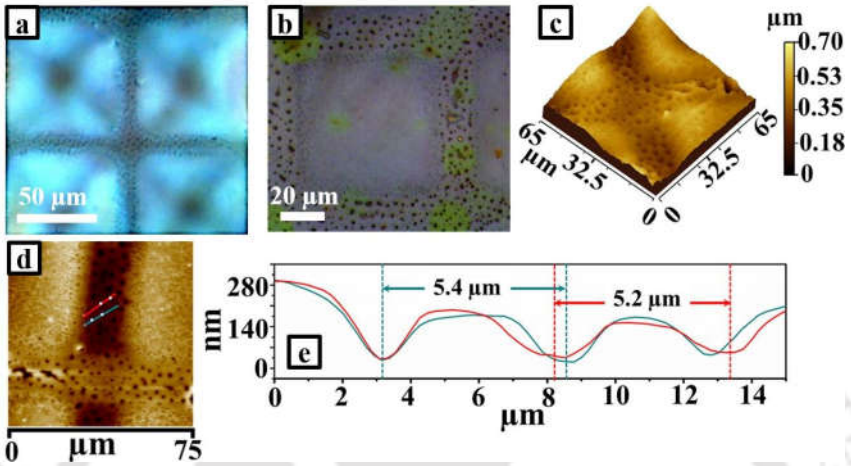

Figure 3.7 (a) Polarised optical micrograph (POM) of the templated viscoelastic hard PDMS film (thickness ~3 μm) during EFL experiment. The bright-field image of the undeformed box area and an array of ~ 4 microwells in the grid area after removal of LC (b). (c)-(d) Atomic force micrograph showing topography and the line scans (e) portraying the surface profile and the wavelength of the morphology.

For a thin hard film of ~ 3 μm, an array of ~ 4 microwells in a single grid width was observed (Figure 3.7). The result is reminiscent of the patterned electrode induced EFL[15] or template induced elastic debonding [50] where commensuration of template dimension and natural wavelength of the instability of a viscoelastic film dictates the final morphology of the surface.

3.3.3. *Templated pattern with the viscoelastic soft film:*

Similar experiment as that of the previous section was performed with viscoelastic soft PDMS film of ~ 3 μm and micropillar morphology with wavelength ~ 1 μm was obtained (Figure 3.8) within the unmodified grid covered area of the film. The obtained wavelength was much smaller than that expected as per equation (1). As the film was significantly liquid-like, the slightest pressure dislodged the materials from underneath the TEM grid and

TH-2671_146153005

rendered the effective film thickness (h ~ 700 nm) much less than the initial thickness. Hence, a reduced wavelength of the morphology was observed.

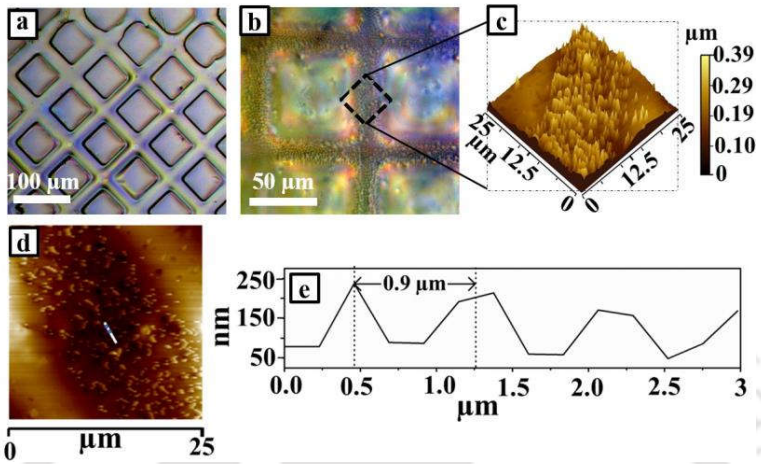

Figure 3.8 (a) Optical micrograph of the templated viscoelastic soft PDMS film (initial thickness ~3 µm). The POM of undeformed box area and of micropillars in the grid area during EFL experiment (b). (c)-(d) Atomic force micrograph showing the topography of the micropillars and the line scans (e) depicting the surface profile and the wavelength of the morphology.

3.4. Conclusions:

In summary, we have demonstrated experimentally for the first time that for a combination of bilayer undergoing EFL, not only the dielectric constant and the film thickness but also the rheology of the bilayer influences the morphology (micropillars or microwells) of the polymer film when instigated within very short time scale. The short time scale of the evolution was achieved using 5CB liquid crystal as an upper layer to realise high dielectric contrast across the LC-PDMS interface and low interfacial tension between 5CB and PDMS. Earlier, morphological variation during EFL was predicted numerically by Wu et al.[28] in a combination of the dielectric contrast and the film thickness ratio. In the present experimental study, we demonstrate that for viscoelastic hard sample, with relatively higher elastic modulus compared to the soft viscoelastic sample, irrespective of film thickness, microwells were obtained. Whereas for soft viscoelastic sample, micropillars were obtained for relatively

TH-2671_146153005

thin films and a combination of micropillars and microwells were observed for a film of ~ 11 μm. Lastly, we have demonstrated a pathway to fabricate multiscale patterns of planer box and grids, decorated with micropillars or microwells by tuning the rheological properties of the polymer films.

भारतीय प्रौद्योगिकी संस्थान गुवाहाटी • Indian Institute of Technology Guwahati •

TH-2671_146153005

References

[1] P. L. Burn, A. Kraft, D. R. Baigent, D. D. C. Bradley, A. R. Brown, R. H. Friend, R. W. Gymer, A. B. Holmes, R. W. Jackson, *J Am. Chem Soc.* **1993**, *115*, 10117.

[2] A. Salleo, W. S. Wong, M. L. Chabinyc, K. E. Paul, R. A. Street, *Adv. Funct. Mater.* **2005**, *15*, 1105.

[3] S. R. Forrest, *Nature* **2004**, *428*, 911.

[4] J. Y. Lee, B. H. Hong, W. Y. Kim, S. K. Min, Y. Kim, M. V Jouravlev, R. Bose, K. S. Kim, I. Hwang, L. J. Kaufman, C. W. Wong, P. Kim, K. S. Kim, *Nature* **2009**, *460*, 498.

[5] A. Verma, A. Sharma, *Adv. Mater.* **2010**, *22*, 5306.

[6] A. R. Kabir, D. Inoue, Y. Kishimoto, J. Hotta, K. Sasaki, N. Kitamura, J. P. Gong, H. Mayama, A. Kakugo, **2015**, 1.

[7] P. Nghe, E. Terriac, M. Schneider, Z. Z. Li, M. Cloitre, B. Abecassis, P. Tabeling, *Lab Chip* **2011**, *11*, 788.

[8] B. Jose, P. McCluskey, N. Gilmartin, M. Somers, D. Kenny, A. J. Ricco, N. J. Kent, L. Basabe-Desmonts, *Langmuir* **2016**, acs. langmuir.5b03540.

[9] P. Shivapooja, Q. Wang, B. Orihuela, D. Rittschof, G. P. López, X. Zhao, *Adv. Mater.* **2013**, *25*, 1430.

[10] L. J. Guo, *Adv. Mater.* **2007**.

[11] D. Qin, Y. Xia, G. M. Whitesides, *Nat. Protoc.* **2010**.

[12] J. Kong, M. G. Chapline, H. Dai, *Adv. Mater.* **2001**.

[13] K.-Y. Suh, M. C. Park, P. Kim, *Adv. Funct. Mater.* **2009**, *19*, 2699.

TH-2671_146153005

[14] S. Harkema, U. Steiner, *Adv. Funct. Mater.* **2005**, *15*, 2016.

[15] P. S. G. Pattader, I. Banerjee, A. Sharma, D. Bandyopadhyay, *Adv. Funct. Mater.* **2011**, *21*, 324.

[16] P. J. Cressman, *J. Appl. Phys. 34*, 2327.

[17] M. D. Morariu, N. E. Voicu, E. Schäffer, Z. Lin, T. P. Russell, U. Steiner, *Nat. Mater.* **2003**, *2*, 48.

[18] H. Xiang, Y. Lin, T. P. Russell, *Macromolecules* **2004**, *37*, 5358.

[19] M. D. Dickey, S. Gupta, K. A. Leach, E. Collister, C. G. Willson, T. P. Russell, *Langmuir* **2006**, *22*, 4315.

[20] Z. Lin, T. Kerle, T. P. Russell, E. Schäffer, U. Steiner, *Macromolecules* **2002**, *35*, 3971.

[21] R. V. C. K. Matar, **2017**, *032104*.

[22] D. Bandyopadhyay, A. Sharma, U. Thiele, D. S. Reddy, *Langmuir* **2009**, *25*, 9108.

[23] P. D. S. Reddy, D. Bandyopadhyay, A. Sharma, *J. Phys. Chem. C* **2012**, *116*, 22847.

[24] J. Nase, A. Lindner, *Phys. Rev. Lett.* **2008**, *074503*, 1.

[25] S. Roy, N. Bhandaru, R. Das, G. Harikrishnan, R. Mukherjee, *Appl. Mater. Interfaces* **2014**, *6*, 6579.

[26] N. Arun, A. Sharma, P. S. G. Pattader, I. Banerjee, H. M. Dixit, K. S. Narayan, *Phys. Rev. Lett.* **2009**.

[27] Z. Lin, T. Kerle, T. P. Russell, *Macromolecules* **2002**, *35*, 6255.

[28] N. Wu, W. B. Russel, *Ind. Eng. Chem. Res.* **2006**, *45*, 5455.

[29] P. Roy, R. Mukherjee, D. Bandyopadhyay, P. S. Gooh Pattader, *Nanoscale* **2019**.

TH-2671_146153005

[30] P. K. Rai, M. M. Denn, C. Maldarelli, *Langmuir* **2003**, *19*, 7370.

[31] S. Chae, C. Lee, H. Lee, T. Kim, Y. J. Kang, *Lab Chip* **2009**, *9*, 1957.

[32] L. M. Blinov, *Structure and Properties of Liquid Crystals*; Springer, 2011.

[33] R. Dey, U. U. Ghosh, S. Chakraborty, S. DasGupta, *Langmuir* **2015**, *31*, 11269.

[34] S. Subramanian, M. Gonuguntla, A. Sharma, R. Mukherjee, *Langmuir* **2006**, *22*, 7066.

[35] R. Mukherjee, R. Pangule, A. Sharma, I. Banerjee, *J Chem. Phys.* **2007**, *127*, 064703.

[36] T. Honda, M. Miyazaki, H. Nakamura, H. Maeda, *Lab Chip* **2005**, *5*, 812.

[37] V. Freedericksz, V. Zolina, *Trans. Faraday Soc.* **1933**, *140*, 919.

[38] P.-G. de Gennes, J. Prost, *The Physics of Liquid Crystals*; 2nd Editio.; Oxford University Press, U.S.A., 1995.

[39] P. Dhara, N. Bhandaru, A. Das, R. Mukherjee, *Sci. Rep.* **2018**, *8*, 1.

[40] Y. Xia, E. Lee, H. Hu, M. A. Gharbi, D. A. Beller, E.-K. Fleischmann, R. D. Kamien, R. Zentel, S. Yang, *ACS Appl. Mater. Interfaces* **2016**, *8*, 12466.

[41] H. Dreyfus-lambez, D. Stoenescu, I. Dozov, P. Martinot-Lagarde, *Mol. Cryst. Liq. Cryst. Sci. Technol. Sect. A. Mol. Cryst. Liq. Cryst.* **2000**, *352*, 19.

[42] V. Shankar, A. Sharma, *J. Colloid Interface Sci.* **2004**, *274*, 294.

[43] R. Verma, A. Sharma, K. Kargupta, J. Bhaumik, *Langmuir* **2005**.

[44] S. Srivastava, P. D. S. Reddy, C. Wang, D. Bandyopadhyay, A. Sharma, *J. Chem. Phys.* **2010**.

TH-2671_146153005

[45] P. S. Goohpattader, M. K. Chaudhury, *Eur. Phys. J. E. Soft Matter* **2012**, *35*, 67.

[46] B. Carmeli, A. Nitzan, *J. Chem. Phys.* **1983**, *79*, 393.

[47] P. Hänggi, P. Talkner, M. Borkovec, *Rev. Mod. Phys.* **1990**, *62*, 251.

[48] M. K. Chaudhury, P. S. Goohpattader, *Eur. Phys. J. E* **2013**, *36*, 15.

[49] M. K. Chaudhury, P. S. Goohpattader, *Eur. Phys. J. E* **2012**, *35*.

[50] N. Bhandaru, A. Sharma, R. Mukherjee, *ACS Appl. Mater. Interfaces* **2016**, acsami.6b09127.

TH-2671_146153005

TH-2671_146153005

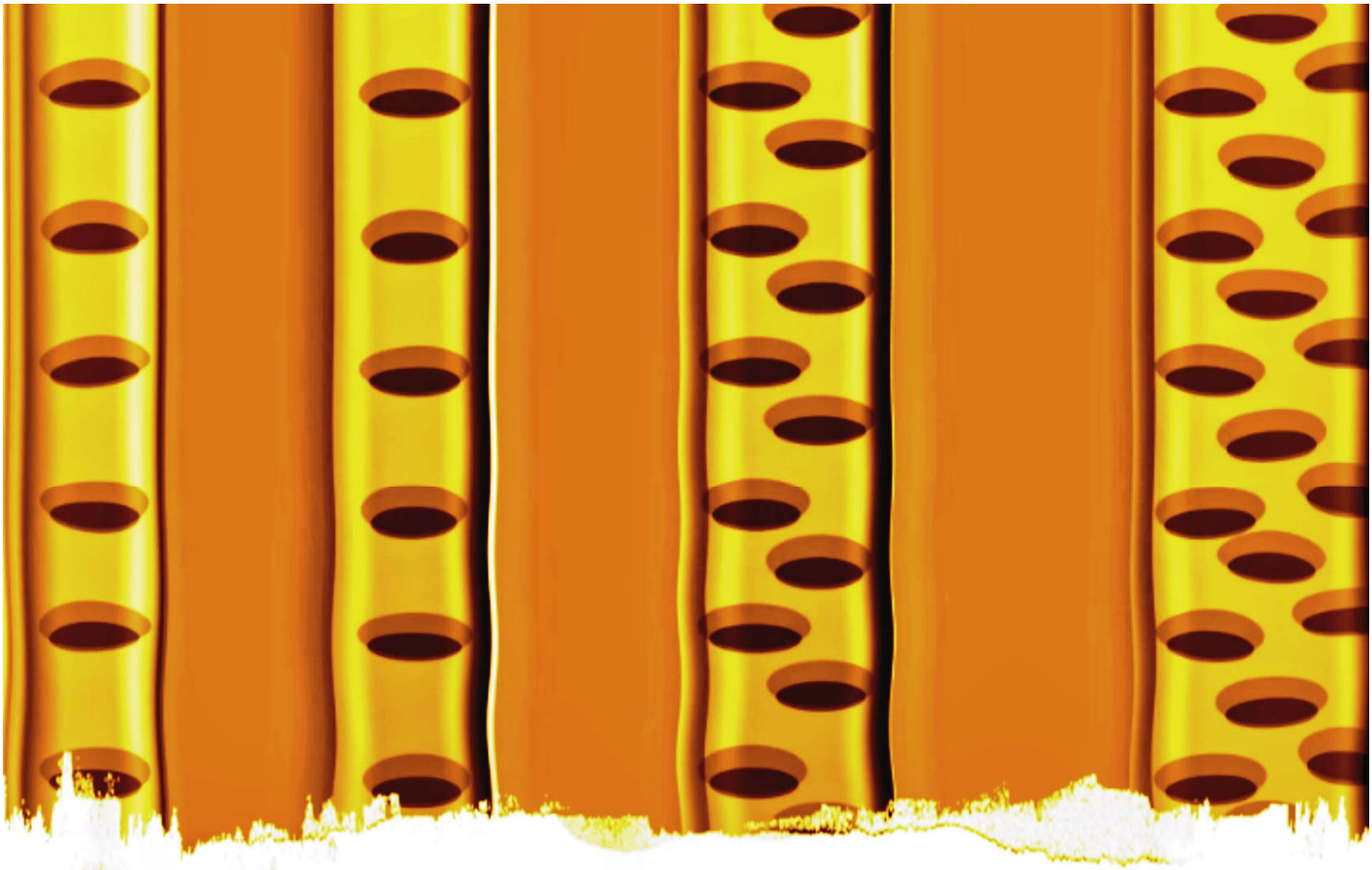

Chapter 4

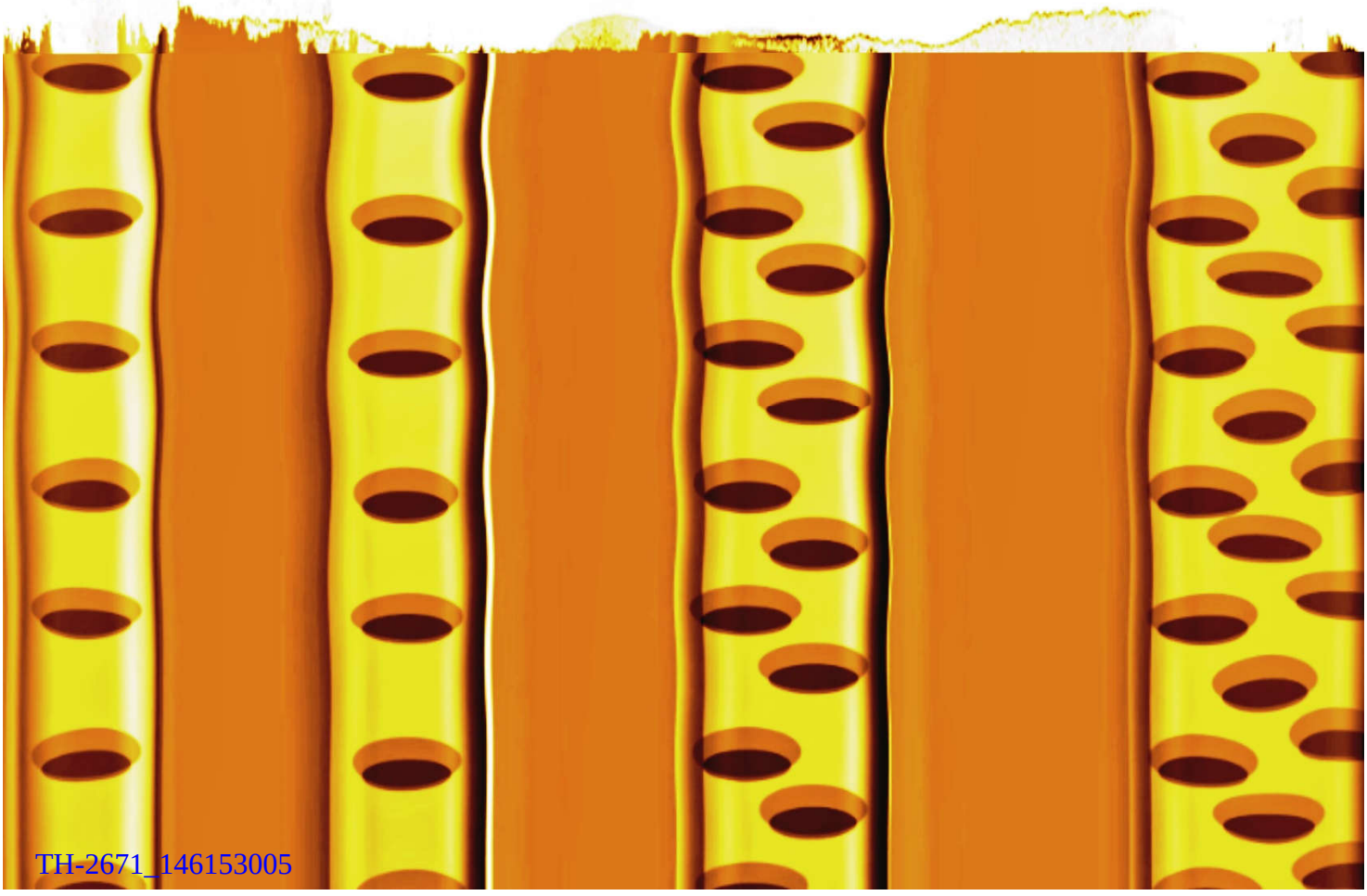

TH-2671_146153005

Chapter 4

ELECTRIC FIELD INDUCED TEMPLATE DIRECTED MULTISCALE PATTERN FORMATION IN POLYMER LIQUID CRYSTAL CONFINED BILAYER

Abstract

Controlling interfacial structure formation on microscale and mesoscale has been investigated extensively. One way to bring about such control demands manipulation of the instabilities at the interfaces. Our previous studies show that the electrohydrodynamic instability in the case of a polymer-liquid crystal bilayer system can fabricate micropillars or microwells at ease. This work will demonstrate the method to control the mesostructure formation in the PDMS-5CB nematic liquid crystal interface. Sufficient viscous or elastic component of PDMS plays a significant role to the shape of the deformation at the PDMS-5CB interface. Here we introduced a patterned bottom electrode to confine the electrical stress to specific regions at an instance based on the separation distance to that region from the top flat electrode. The electric field's spatial variation due to lithographically fabricated striped bottom electrode enables us to align formed micropillars/microwells. Since the wavelength of formed mesostructures depends linearly on the PDMS thin film thickness, we get a multiscale pattern at a higher electric field.

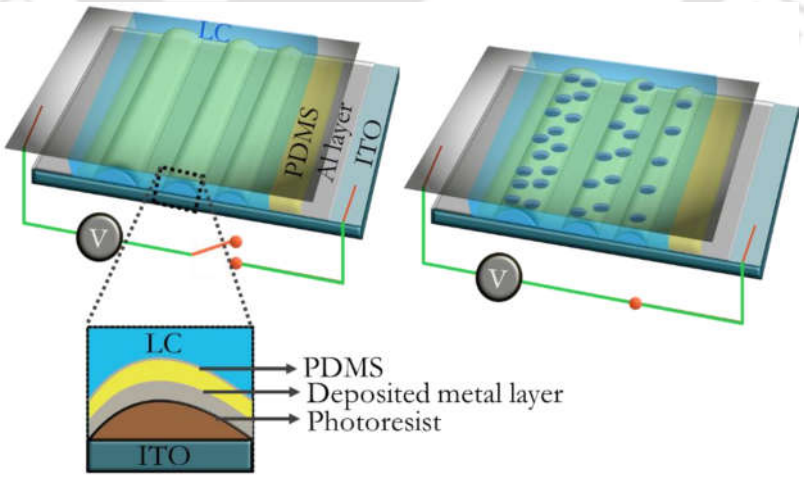

TH-2671_146153005

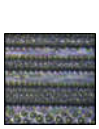

4.1. Introduction

Mesostructure formation at the interface has utmost scientific and technological importance. Fabrication of mesostructured interface, therefore, a subject of intense research for decades. Besides conventional lithographic techniques and other soft lithographic techniques, an electric field induced lithography (EFL) technique has propitious potential. When an external electric field is applied normal to the confined polymer-air[1] or polymer-polymer[2] bilayer system between two flat electrodes, the interface gets destabilized due to the originated Maxwell stress.[3,4] After a specific threshold voltage, this stress overpowers interfacial tension, restoring force, etc. Thus, the initial flat interface turns into large-scale periodical structures. These structured interfaces are naturally filled with hexagonally closed packed pattern with a wavelength determined by the process parameters.

Many successful attempts were made to align these formed mesostructures. The use of a templated top electrode gives the liberty to modulate the electric field within the system spatially. Thus, the EFL process has been investigated as a pattern replication process in the presence of a templated electrode. When an electric field is applied normal to a polymer thin film, resting on the bottom electrode, micropillars appear from the film surface that elongates with the increase of effective electric field within the parallel plate electrodes.[5–7] Now, replacing air with another fluid change the polymer's surface tension to the interfacial tension between the fluidic interfaces.

4.2. Materials and methods

4.2.1. Materials

Indium tin oxide coated glass plates (ITO, 10 Ω sq^{-1}) were obtained from Macwin India, India. Hexamethyldisilazane (HDMS) primer was purchased from HiMedia Laboratories Pvt. Ltd. The SU-8 negative photoresist (SU-8, 2007) and SU-8 developer were obtained from Micro.Chem, Pvt.Ltd. A Sylgard 184 elastomer kit having two components as oligomer and crosslinker, was procured from Dow Corning Mumbai, India. Analytical grade n-hexane and isopropanol were obtained from Sisco Research Laboratories

TH-2671_146153005

Pvt. Ltd India. 5CB Nematic liquid crystal was obtained from Sigma-Aldrich. All these chemicals were used without further purification.

4.2.2. Electrode preparation

We prepared the substrates used as a top and bottom electrode for performing the EFL experiment from indium tin oxide (ITO) coated glass (10 Ω sq^{-1}, Macwin India). The indium tin oxide (ITO) coated glass plate was cut into 15 mm × 15 mm pieces with a glass cutter. Firstly, these ITO coated glass pieces were washed in boiling acetone and boiling isopropanol in each for 15 min duration. After each washing step, ITO glass pieces were rinsed with deionized water to remove the adhered solvent. The cleaned substrates were stored under DI water. Finally, before the experiment, the cleaned substrates were dried using a stream of dry nitrogen gas.

4.2.3. Patterning electrodes using photolithography

The physically patterned substrates (bottom electrodes) were fabricated in Maskless photolithography using SU-8 negative photoresist. Initially, a Hexamethyldisilazane (HDMS) primer (HiMedia Laboratories Pvt. Ltd) was spin-cast on the cleaned ITO substrate using a spin coater (Apex instruments, model: spin NXG-P1) with a spin speed of 400 rpm for 60 s. This primer is used to increase the adhesion of photoresist during a spin coating on the ITO substrate surface. Subsequently, to remove moisture content, the spin-coated photoresist on the substrates was heated (known as soft baking) at 175 ℃ on a hot plate for 15 min. A 2:1 solution of negative photoresist (SU-8) and SU-8 developer was prepared. The prepared solution was spin-coated on the soft-baked substrates with a spin speed of 3537 rpm and 5 m/s acceleration for 60 seconds. The thickness of the photoresist film was 20 μm. Then the spin-coated substrates were soft baked at a temperature of 80 ℃ for 3 min and 110 ℃ for 6 minutes step by step.

The required pattern to be written on the soft-baked substrate was designed using KLayout editor. The designed pattern was written on the spin-coated substrate using KLOE LaserWriter (Dilase 250) by exposure to the UV light at the 0.5 modulations and 0.6 m/s velocities**.** After exposure to the UV light, the substrates were heated (known as post exposed bake) at a temperature of 80 ℃ for 1 min and 110 ℃ for 5 min step by step. This post expose bake is used to complete photoreaction initiated during exposure of

TH-2671_146153005

UV light. Developing is a step for removing the exposed area in a positive photoresist and the unexposed area in a negative photoresist. After UV exposure and baking, the substrates were dipped into the SU-8 developer for 6 min to dissolve the substrates' unexposed parts. The developed substrates were rinsed by dipped into the isopropanol for 15 s. The rinsed substrates were dried with nitrogen gas, and they were hard-baked at a temperature of 175 ℃ for 10 minutes. Since SU-8 negative photoresist has a very high dielectric constant, a 100 nm thick aluminum metal film was deposited onto the SU-8 film surface (HHV Lab Coater Auto500).

4.2.4. PDMS film coating

A spin coating aliquot of PDMS was prepared by first mixing the crosslinker with the oligomer and then diluting it with n-hexane (analytical grade, Sisco Research Laboratories Pvt. Ltd India). For fabrication of viscoelastic hard films, 2% crosslinker was mixed in the oligomer, and for viscoelastic soft films, 1% crosslinker was used. The volume of n-hexane was varied to get PDMS films of different thicknesses. For example, 1:2.5 and 1:10 volume ratios of PDMS to n-hexane produced 11 μm and ~3 μm thick PDMS films, respectively. The physically patterned and metal deposited bottom ITO electrode was masked with magic tape (Scotch Magic Tape-810 series, 3M India Ltd) for leaving spaces required for spacers and electrical contact. The spin coating aliquot was pipetted out to the center of the physically patterned ITO electrode, and the spin coating was performed (2500 rpm, 120 s).

After the spin coating, the magic tapes were removed, and the films were cured in a vacuum oven. For the viscoelastic hard sample, the films were cured at 120 °C for 12 h, whereas for the soft films, the curing temperature and time were 80 °C and 1 h respectively. Subsequently, the cured films of both hard and soft films were removed from the vacuum oven and cooled to room temperature before doing the next step (EFL). The thickness of the spin-coated PDMS film was obtained with a stylus contact profilometer (Dektak Veeco).

4.2.5. EFL experiment

Commercial polyimide tape (thickness ~35 μm) was used as spacers to maintain uniform gap distance between the top and bottom electrode. Around 5-6 μl of 5CB liquid crystal was pipetted out and dispensed

TH-2671_146153005

on the PDMS thin film. The top flat ITO electrode was used to confine the system. Both the electrodes were connected to the DC voltage source (SES Instruments Pvt. Ltd., EHT-II) through copper wire. In this set up the 5CB liquid crystal- PDMS film bilayer was sandwiched between the physically patterned (bottom), and flat (top) ITO coated glass substrates.The voltage was applied at a ramping speed of ~2 Vs^{-1} until the microstructures were formed on the PDMS thin film. The structures formed on the PDMS film were observed and recorded with an optical microscope (Leica DM2500 M) having a CCD (Leica DFC450 C) camera.

4.2.6. Characterizations

At the high voltage, the microstructures were formed at the 5CB liquid crystal- PDMS interface and the voltage supplied was switched off. For further exploration of the morphology of the PDMS film, the top electrode was removed carefully, and the 5CB liquid crystal was removed from the viscoelastic PDMS film by using filter paper for the hard film and by blowing using nitrogen gas for the soft film. After removing the liquid crystal, the PDMS films were exposed to UV- ozone for up to 20 min for the hard film and 5 minutes for the soft film. After the UV-ozone treatment, the viscoelastic thin films were washed with dimethyl sulfoxide (DMSO, Merck, India) to remove excess 5CB liquid crystal without swelling the PDMS. Finally, the PDMS film surface's topography was characterized using a field emission electron microscope (Jeol Ltd., JSM-761 OF).

4.3. Results and discussion

4.3.1. Evolution of morphology at the interface

Polydimethylsiloxane (PDMS) is isotropic in nature and has a very low positive dielectric constant (2.65).[8] On the other hand, liquids crystals (LCs) have anisotropic dielectric constants related to the alignment of the director of the LC molecules that can be controlled with the application of the electric field. Because of the anisotropy of 5CB NLC, it has two different magnitudes of dielectric constant depending on the direction ($\varepsilon_{||}$ = 15.70 and $\varepsilon_{\perp}$ = 7.50).[9] In general, 5CB is a naturally twisted nematic liquid crystal, which, on the application of voltage, untwist itself in varying degrees depending on the magnitude of an applied voltage.

TH-2671_146153005

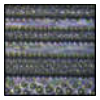

Initially, without the electric field, the liquid crystal in bulk is in a nematic state, and directors mostly parallel to the top electrode with a lateral variation of the director field of the LC and might be influenced by the local hydrodynamics. Upon application of the electric field, two interesting phenomena occur in the system. Firstly, the LC layer undergoes Fréedericksz transition, i.e., the 5CB molecules, having very high positive dielectric anisotropy, try to align themselves along the applied electric field direction. Supported by the homeotropic anchoring at the PDMS interface, the LC molecules then try to maintain their vertical alignment (as the electric field is applied in the vertical z-direction) in bulk. Only near the top ITO electrode, the LC layer exhibits a large director gradient. Secondly, due to electric pressure induced by the applied electric field, the PDMS-LC interface deforms to minimize the system's overall energy.

In the PDMS-LC bilayer, sandwiched between two electrodes, upon application of electric field, the PDMS-LC interface destabilizes, and the fastest-growing dominant wavelength λ_{max} gives the length scale of this instability. The theoretical derivation of the characteristic wavelength of instability is well established for isotropic bilayer systems, be it polymer-air or polymer-polymer.[10–17] In the present case, we resort to a simplistic approach assuming LC and PDMS are both Newtonian fluids, and the continuum approximation is applied to the system. From there, we deduce the corresponding dominant wavelength applicable to our confined bilayer system, which is given by:

$$\lambda_{max} = \frac{2\pi\sqrt{2\gamma\{\varepsilon_2 d + h(\varepsilon_1 - \varepsilon_2)\}^3}}{\sqrt{V^2\varepsilon_0\varepsilon_1\varepsilon_2(\varepsilon_1 - \varepsilon_2)^2}} \qquad (1)$$

Here, λ_{max} is the fastest growing wavelength of electrohydrodynamic instability. V is the applied voltage, ε_0 is the dielectric permittivity of the vacuum, ε_1 and ε_2 are the dielectric constants of 5CB and PDMS, γ is the interfacial tension at PDMS-5CB interface, h is the PDMS film thickness, and d is the separation distance between electrodes.

Although we have assumed LC as a homogeneous liquid with no special consideration of the director fluctuations, equation 1 successfully predicts the variation of the λ with film thickness.

TH-2671_146153005

Experimental data for the viscoelastic hard film shows a slightly smaller length scale than the theoretically predicted value. When all other geometrical parameters are constant in an air-PDMS bilayer arrangement, theoretical estimation reveals that the characteristic length scale is about two orders of magnitude higher than the LC-PDMS system. While scaling down the feature size of formed micro-wells, it was possible to get lateral wavelengths as low as that of 1.05 μm.[4]. In one of our previous works (Chapter 4), it was shown that substrate rheology plays an essential role in predicting the nature of destabilization at the interface. For this study also, the PDMS's viscoelastic nature is varied to get micropillar or microwell morphology.

4.3.2. Templated electrode for Spatio-temporal multiscale patterning

4.3.2.1. Viscoelastic soft PDMS film

First, we consider the EFL process for viscoelastic soft PDMS film, which occurs in the presence of an electric field. The electric field and hence the destabilizing forces will always be the most substantial where the distance between the polymer and top electrode is the least. In our system, the patterned bottom electrode makes the effective electric field heterogeneous in three different zones. Consequently, the region's highest effective electric field density will be experienced where the distance between the PDMS film to top electrode distance is the least(d_1 in Figure 4.1). Microstructures will appear at a relatively higher voltage, where the distance between the PDMS film to the top electrode is maximum. Here according to Figure 4.1a, $d_1 < d_2$.

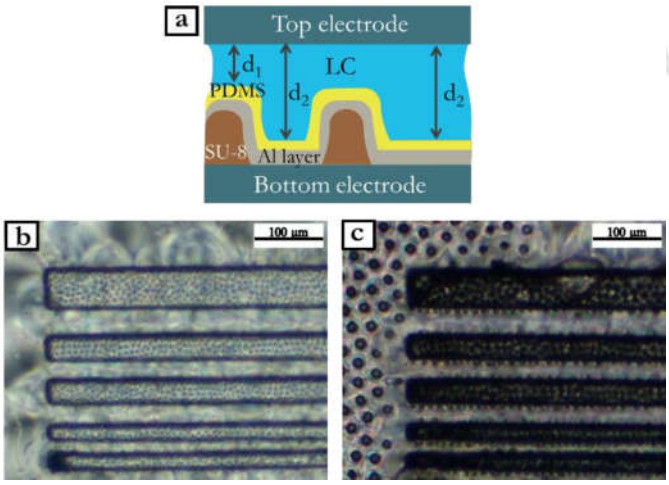

TH-2671_146153005

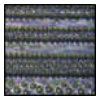

Figure 4.1 (a) Schematic diagram showing the effective distance distribution between the PDMS film to the top electrode. (b) Polarized optical micrograph of the patterned electrode in PDMS/5CB system at 40 V electric field bias. The PDMS film (thickness ~11 μm) is viscoelastic soft. (c) The same interface when the voltage is ramped to 150 V.

Figure 4.1a shows that two more zones in the system are there where the distance between the PDMS film to the top electrode is equal (d_2). Ideally, the micropatterns should appear at the same time and the same voltage. But experimentally, after the stripe, the patterns appeared at the pattern's outside area. A gradient of electrostatic pressure is created from the outside to the patterned area, and with the ramping of voltage, the formation of microstructure followed the path. The reason is the variation of electric field lines in these two areas is different. Since the number of field lines is proportional to the magnitude of the charge, in the pattern's outside area, charge distribution is homogeneous due to uniformity in planer electrodes' surface area. However, inside the pattern, due to allocated charges, electric field lines are dispersed. The number of field lines starts emerging and amplifies its number density at a relatively higher voltage in the narrow grooved area between two stirpes. So, the micropatterns appeared at the last moment inside the grooved area when micropatterning in all the other regions is completed.

Figure 4.1b shows that for an ~11 μm viscoelastic soft PDMS film, the microstructures arise at a very low voltage (40 V) on top of the stripe patterns. With ramping of voltage, the electric field tries to order the microstructures to attain the system's maximum dominant wavelength. At 150 V, microstructures appear both in and outside the patterned stripes. There works a heterogeneous electric field at the edges of the stripes, which induces the structure formation at the immediate vicinity outside the stripe.

TH-2671_146153005

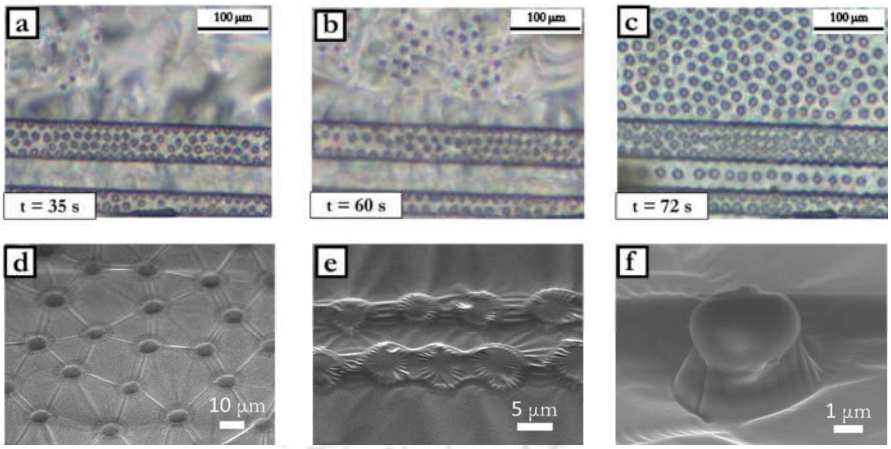

Figure 4.2 Polarized optical micrographs showing the evolution of morphology in the patterned viscoelastic soft PDMS substrate at different voltages, (a) ~ 70 V, (b) ~ 120 V, and (c) ~ 145 V, respectively. (d) Field emission scanning electron micrograph (FESEM) of micropillars formed outside the stripe pattern area. Image (e) shows the FESEM image of aligned rimmed structures from which micropillars are yet to develop. (f) FESEM image of a single developed micropillar in the physically patterned stripe.

Figure 4.2a-4.2c shows the different stages of multiscale pattern formation on the physically patterned soft PDMS. When 40 V voltage is applied on an 11 µm thick PDMS film, the distance between the top electrode and the polymer film is the least, so the microstructures form exclusively on the stripes. In this process, the number of microstructures' array depends on the width (w) of the stripe, e.g., the w = 30 µm stripe accommodated 3 arrays of the microstructures, and where w = 50, the number of arrays also increased. At 70 V, when the stripes were saturated with microstructures, then the outside area of the pattern begins to alter its morphology (Figure 4.2a). When the voltage is raised to 120 V, the microstructures' number density at the outside region saturates. Figure 4.2c shows the formation of structures in the grooves of the pattern when the voltage is close to 150 V. FESEM characterization (Figure 4.2d-4.2f) confirms the microstructures as micropillars of soft viscoelastic PDMS.

4.3.2.2. Viscoelastic hard PDMS film

As discussed previously, the EFL experiment was repeated with the patterned viscoelastic hard PDMS films(thickness ~ 3 µm and ~ 11 µm). The 11 µm shows the same multiscale patterning trend as the

TH-2671_146153005

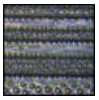

corresponding soft film of equal thickness (Figure 4.4a-4.4c). The only difference is that we get microwells instead of micropillars like viscoelastic soft PDMS film (Figure 4.4d). The reason behind getting micropillars or microwells is detailed in Chapter 3. For hard PDMS film, the threshold voltage of microstructure formation is higher than the soft film. But for hard PDMS film, microwells can withstand higher voltage, and microstructure coalescence does not happen like the soft film.

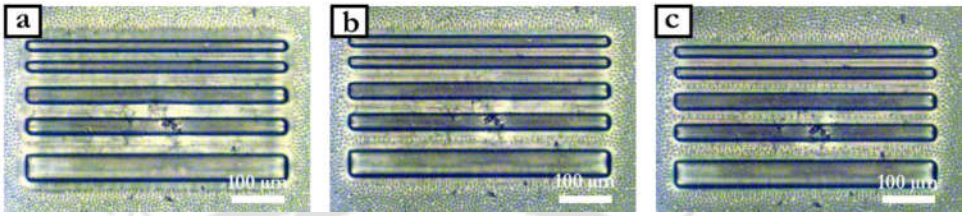

Figure 4.3 Polarized optical micrographs showing the evolution of morphology in the patterned viscoelastic hard PDMS substrate (thickness ~ 3 µm) at different voltages, (a) ~ 180 V, (b) ~ 220 V, and (c) ~ 300 V, respectively.

For ~ 3 µm hard viscoelastic film, the micropatterning started with the outside area far from line patterns. Gradually the microwells approached the stripe pattern, but on top of the pattern, microwells never formed. At relatively higher voltage (~ 300 V), the microgrooves were also filled with arrays of microwells. The probable reason behind this is, PDMS films were spin-cast on the Al-metal coated patterned photoresist, and for getting ~ 3 µm film, the spin coating aliquot of PDMS is enough diluted. On the patterned area, it never formed uniform film rather, the PDMS material was dislodged from the top and deposited to the immediate microgroove while spinning. This gives rise to such unexpected observation in EFL patterning.

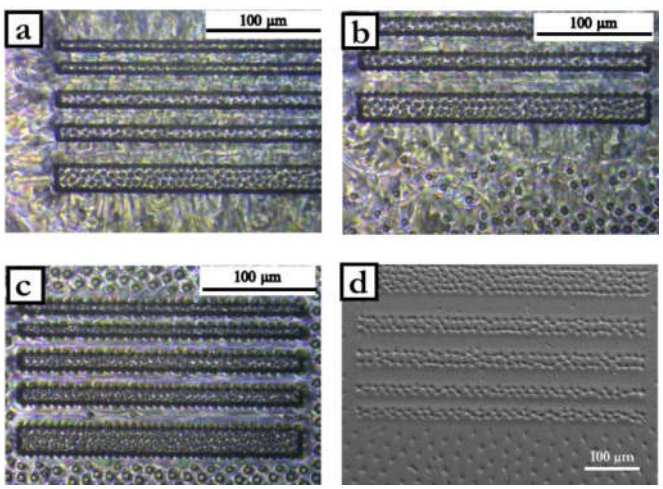

TH-2671_146153005

Figure 4.4 (a)-(c) Polarized optical micrographs show the evolution of morphology in the patterned viscoelastic hard PDMS substrate (thickness ~ 11 μm) at different voltages, (a) ~ 280 V, (b) ~ 320 V, and (c) ~ 580 V, respectively. (d) FESEM micrograph shows the microwell decorated stripe patterns.

4.4. Conclusions

We fabricated a multiscale patterned PDMS substrate with four distinct wavelengths in the pattern. Three of them correspond to the electric field's spatial variation in the EFL experiment, and another one generated while physically patterning the substrate. By changing the rheological characteristics of the PDMS film, we created micropillar/microwell morphology. It was also noticed that the stripe width also contributed mostly to electrohydrodynamic patterning. By switching off the voltage supply at any moment, we can cease the patterning process to get our desired pattern. Using liquid crystal in the patterning process lowers the threshold voltage and lowers down the feature sizes and wavelengths. More complex patterns can be fabricated lithographically, and with the help of electric field and liquid crystal, multiple long and short scale patterns can be achieved.

TH-2671_146153005

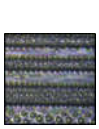

References

[1] N. E. Voicu, S. Harkema, U. Steiner, *Adv. Funct. Mater.* **2006**, *16*, 926.

[2] Z. Lin, T. Kerle, T. P. Russell, E. Schäffer, U. Steiner, *Macromolecules* **2002**, *35*, 6255.

[3] N. Wu, M. E. Kavousanakis, W. B. Russel, *Phys. Rev. E* **2010**, *81*, 026306.

[4] P. Roy, R. Mukherjee, D. Bandyopadhyay, P. S. Gooh Pattader, *Nanoscale* **2019**, DOI 10.1039/c9nr05729c.

[5] M. D. Morariu, N. E. Voicu, E. Schaffer, Z. Q. Lin, T. P. Russell, U. Steiner, *Nat. Mater.* **2003**, *2*, 48.

[6] P. S. G. Pattader, I. Banerjee, A. Sharma, D. Bandyopadhyay, *Adv. Funct. Mater.* **2011**, *21*, 324.

[7] B. N. Wu, L. F. Pease, W. B. Russel, **2006**, 1992.

[8] R. Dey, U. U. Ghosh, S. Chakraborty, S. DasGupta, *Langmuir* **2015**, *31*, 11269.

[9] S. Chandrasekhar, *Liquid Crystals*, **1992**.

[10] N. Arun, A. Sharma, P. S. G. Pattader, I. Banerjee, H. M. Dixit, K. S. Narayan, *Phys. Rev. Lett.* **2009**, DOI 10.1103/PhysRevLett.102.254502.

[11] R. Verma, A. Sharma, K. Kargupta, J. Bhaumik, *Langmuir* **2005**, *21*, 3710.

[12] N. Arun, A. Sharma, V. B. Shenoy, K. S. Narayan, *Adv. Mater.* **2006**, *18*, 660.

[13] G. Tomar, V. Shankar, A. Sharma, G. Biswas, *J. Nonnewton. Fluid Mech.* **2007**, *143*, 120.

[14] V. Shankar, A. Sharma, *J. Colloid Interface Sci.* **2004**, DOI 10.1016/j.jcis.2003.12.024.

[15] S. Srivastava, P. D. S. Reddy, C. Wang, D. Bandyopadhyay, A. Sharma, *J. Chem. Phys.* **2010**, DOI 10.1063/1.3400653.

[16] N. Wu, L. F. Pease, W. B. Russel, *Langmuir* **2005**, *21*, 12290.

[17] D. Bandyopadhyay, A. Sharma, U. Thiele, D. S. Reddy, *Langmuir* **2009**, *25*, 9108.

TH-2671_146153005

TH-2671_146153005

Chapter 5

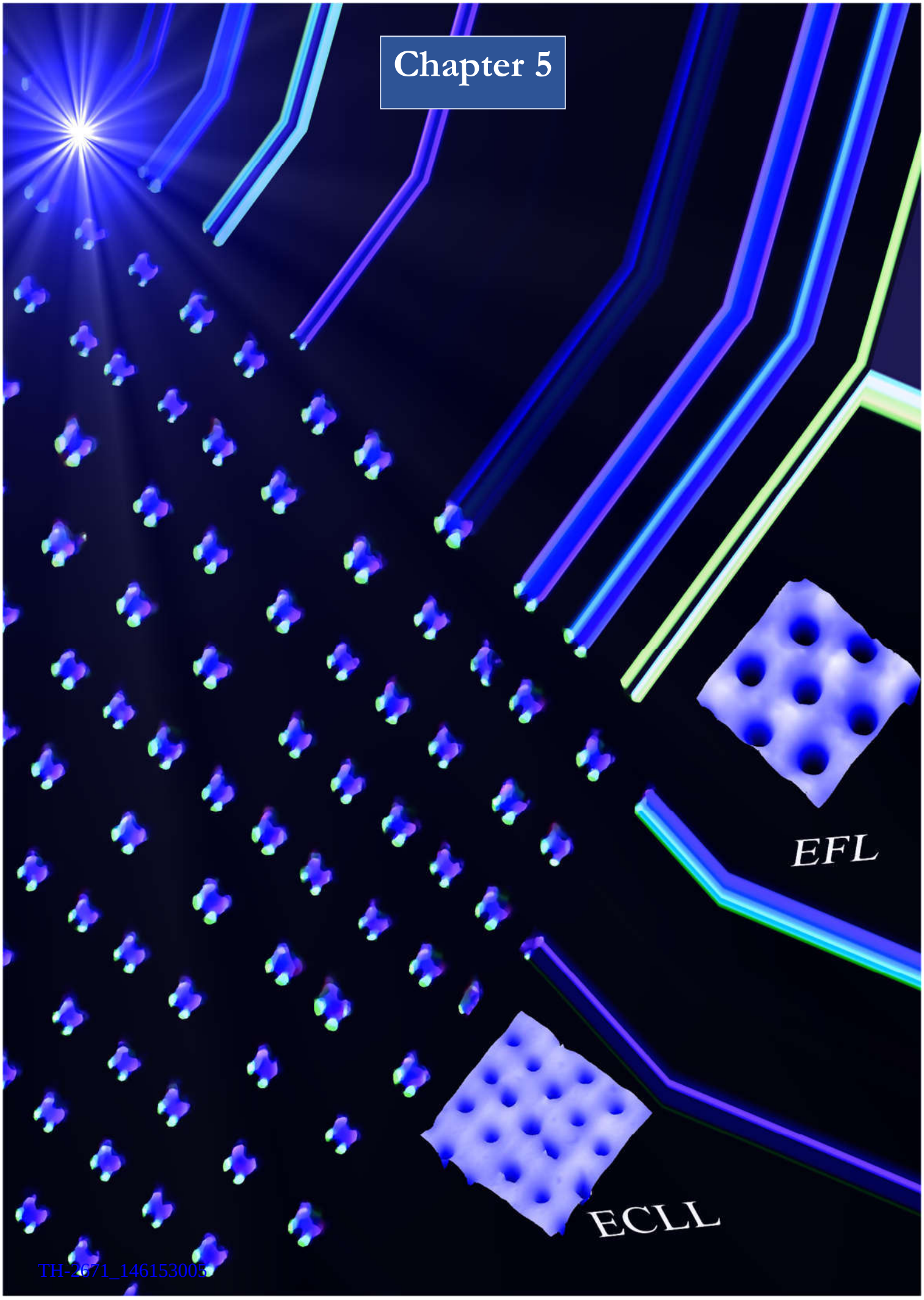

TH-2671_146153003

Chapter 5

ELECTRODYNAMIC-CONTACT-LINE-LITHOGRAPHY WITH NEMATIC LIQUID CRYSTAL FOR TEMPLATE-LESS E-WRITING OF MESOPATTERNS ON SOFT SURFACES

Abstract

We report the development of a single-step, template-less and fast pathway, namely, Electrodynamic-Contact-Line-Lithography (ECLL), to write micro to nanopatterns on the surface of a soft polymer film. As a model system, a layer of nematic liquid crystal (NLC), resting on a polymer thin film, was sandwiched between a pair of electrodes emulating the electrowetting on a dielectric (EWOD) set-up. Upon application of electric field, the Maxwell stresses thus generated at the NLC-polymer interface due to the high dielectric contrast, stimulated an unprecedented fingering instability at the advancing NLC-polymer-air contact line. In the process, the advancing electrospreading front of NLC left the footprint of an array of micro to nanoscale wells on the polymer surface with a long-range ordering, thus unveiled a pathway for maskless patterning of a soft elastic film. Unlike the conventional electric field induced lithography (EFL), the meso-scale morphology was found to follow the short wave length-scales as the periodicity of the patterns (λ_C) varied linearly with the thickness of the film (h), ($\lambda_C \propto h$). The high dielectric contrast at the NLC-polymer interface and the local fluctuation of the NLC directors ensured a time scale much faster than the same observed for the polymer-air systems.

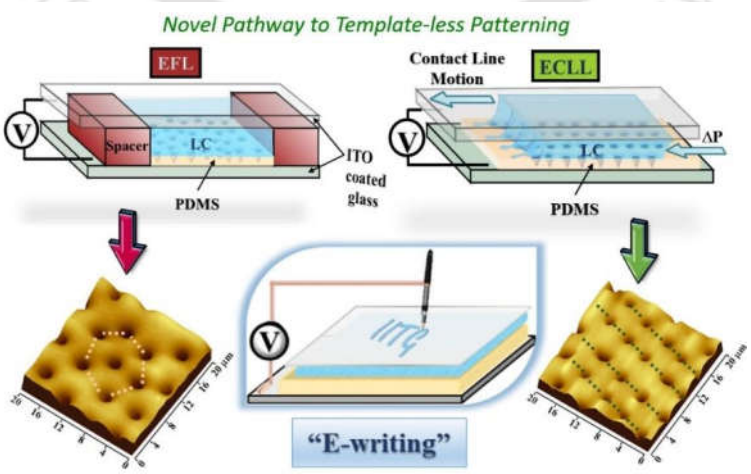

This work is published in ***Nanoscale***, 2019,**11**, 16523-16533 https://doi.org/10.1039/C9NR05729C

TH-2671_146153005

5.1. Introduction

Patterned surfaces with long-range order are ubiquitous in all the natural products and processes. While the fir-waves, phyllotaxy, fish-scales, or sand-dunes are some examples of large-area patterns at the macroscopic length scales, the lotus leaf, chameleon-skin, fingerprint, butterfly wing, or compound eye is known for hosting exotic mesoscale patterns.[1–3] Of late, biomimetics of such micro or nanoscale patterns has helped in improving the efficiency of various applications, which include superhydrophobic surfaces,[4] structural colors,[5] micro or nanoelectronics,[6] health care devices,[7] and quantum technologies.[8] In this regard, one of the long-standing challenges has been the invention of various engineering pathways to decorate large-area ordered patterns on soft to hard polymeric surfaces. In this direction, traditionally, the 'top-down' approaches such as lithography, replica-molding, machining, or milling have served the purpose of miniaturizing the macroscale architectures.[9] In recent years, multifarious 'bottom-up' techniques have also emerged to develop such scaled-down patterns in the form of sol-gel processing,[10] self-assembly,[9] physical or chemical vapor deposition,[11] or molecular beam epitaxy.[12] Largely, in this approach, a cluster of molecules is allowed to assemble or organize under a controlled environment of molecular interactions and/or external stimuli.[13,14] However, most of these engineering methodologies of micro or nanofabrication are found to be either complex or costly or multi-step processes, which in some way restricts their applicability for a wide range of applications.

As an alternative, in recent years, the stimuli-responsive self-organized dewetting of thin polymer films has emerged as a low-cost and reliable top-down approach to pattern soft polymeric surfaces.[9] In particular, a few seminal contributions indicate that the polymer surfaces can also be destabilized by the application of electric field, termed electric field induced lithography (EFL).[15,16] In such processes, initially, a polymer film is sandwiched between a pair of electrodes with a small air gap above the free surface of the film, making a polymer-air parallel plate capacitor configuration.[16–22] Thereafter, when the electric field is applied, the destabilizing electrohydrodynamic (EHD) stress at the polymer-air interface due to the accumulation of the bound[16] or free[23] charges overpower the stabilizing effects of surface tension and elastic forces to form periodic columnar, stripe, or cavity patterns.[22] Interestingly, the use of patterned electrodes[22,24] in EFL has

TH-2671_146153005

helped in imposing a long-range order to the patterns developed. Further, complex patterns with unique morphologies such as hierarchical,[25] cage-like,[26] core-shell[27], etc. have been obtained in different settings such as patterned electrode, bilayer/trilayer of polymers,[28,29] or leaky dielectric bilayers,[23],[30] electrolyte/polymer[31] systems. Notably, a transition from microscale to the nanoscopic patterns has also been achieved by reducing the restoring interfacial tension.[32] It is noteworthy that another alternative pathway to reduce the length scale of EFL patterns can be the use of high dielectric contrast across the interface.[33] However, such systems are so far very less studied owing to the difficulty in identifying isotropic polymers with high dielectric constants (ε). Interestingly, the liquid crystals (LCs) are not only known to have higher dielectric constants ($\varepsilon \sim 5 - 25$) but also well known for their dielectric anisotropy.[34–39] Thus, a polymer-LC interface is expected to have a very high dielectric contrast, which can be suitable for the generation of high EHD stresses. Further, the influence of the homeotropic, planer, or angular orientations of the LC molecules near the boundaries[40] and their consequences to the EHD instabilities is also an unexplored area of research.

In view of this background, herein, we make an attempt to study the interfacial EHD instabilities of a nematic liquid crystal (NLC) layer on a polymer surface emulating the electrowetting on a dielectric (EWOD) experimental set-up.[41] For this purpose, initially, a drop of 4-Cyano-4'-pentylbiphenyl (5CB) liquid crystal of high dielectric constant ($\varepsilon_{\parallel} \sim 19.7$)[40] is placed on a poly-dimethylsiloxane (PDMS) film of low dielectric constant ($\varepsilon \sim 2.65$)[42] before sandwiching them between a pair of ITO-glass electrodes, so that a bilayer arrangement of LC-PDMS is formed, as schematically shown in Figure 5.1a.

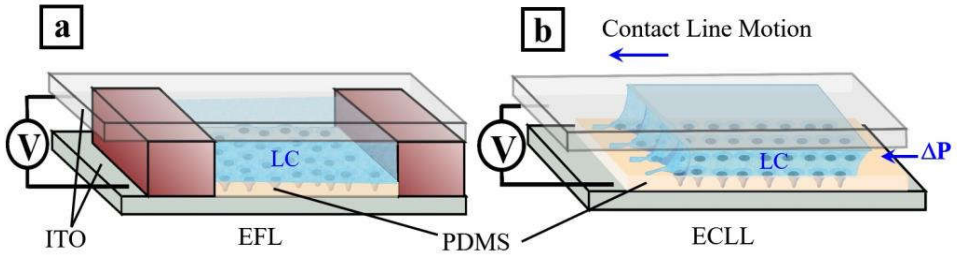

Figure 5.1 Schematic diagram of the experimental set-up: (a) stationary Electric Field induced Lithography (EFL), (b) Electrodynamic Contact Line Lithography (ECLL), for simplicity the spacers in Figure (b) are not

TH-2671_146153005

shown (see text for details). Predominantly hexagonal (a) and aligned (b) arrangement of microwells in the PDMS layer is obtained from EFL and ECLL, respectively.

For such a set-up, the generation of a high-intensity electric field of the order of a few MV/m through the electrodes leads to two phenomena. Firstly, at the 5CB-PDMS interface, away from the 5CB-PDMS-air contact line, conventional electric field induced instability is exhibited that results in the formation of micro/nanoscale wells with specific length scale. Secondly, rapid spreading of the 5CB layer on the PDMS surface takes place till an equilibrium is reached, and the three-phase dynamic contact line becomes stationary again. The Maxwell stresses developed, stimulated the formation of periodic 5CB fingers at the 5CB-PDMS-air contact line, and eventually form micro to nanoscale wells beneath the fingers. Due to the high dielectric contrast at the NLC-PDMS interface and the local fluctuation within the NLC layer, the time scale of the formation of these micro/nanoscale wells is very small. As the micro/nanoscale wells form beneath the periodic fingers of 5CB at the contact line, we attempt to drive the contact line to obtain the well-ordered periodically aligned micro/nano-structures by exploiting the "Electrodynamic Contact Line Lithography (ECLL)" Figure 5.1b. This leads to the template less long-range ordering of micro to nanoscale wells on the PDMS surface. The instability shows a strictly short-wavelength scale as the periodicity of the aligned patterns (λ_C), measured as the distance between two adjacent parallel arrays of micro/nano-wells, varied linearly with the thickness of the film (h) as, $\lambda_C \propto h$. The size and periodicity of the patterns can be tuned from micro to nanoscale by varying the film thickness. The reported Electrodynamic-Contact-Line-Lithography (ECLL) is truly exceptional in many ways because it shows a cost-effective, high throughput, and maskless pathway to fabricate large area micro to nanoscale patterns on the soft-surfaces.

5.2. Experimental section

5.2.1. Sample preparation

Indium tin oxide (ITO) coated glass slides (10 Ω /sq., Macwin India) were cut into 15 × 15 mm² pieces and cleaned with boiling acetone for 30 min and subsequently washed with a copious amount of water to use as the

TH-2671_146153005

transparent electrodes. Sylgard 184, came with the oligomer of dimethyl siloxane, and the crosslinker kit for the preparation of PDMS, was procured from Dow Corning. 2 weight % crosslinker was mixed with oligomer, and this crosslinker-oligomer mixture was dissolved in n-hexane (analytical grade, Sisco Research Laboratories Pvt. Ltd., India). This solution was spun-cast on an ITO-glass substrate (or bottom electrode) using a spin coater (Apex instruments, model: spinNXG-P1, rpm 2500, spin duration: 120 s) and cured for an hour at 120°C.[43] The thickness of the PDMS film was controlled by varying the concentration of the crosslinker-oligomer mixture in n-hexane. PDMS solution thus prepared was spin-coated on cleaned ITO coated glass substrate. Before spin coating, the substrates were suitably masked with magic tape (Scotch Magic Tape-810 series, 3M India Ltd.) to leave spaces for electrical connections and spacers. Once the spin coatings were done, the tape was removed without leaving a trace of adhesive.

5.2.2. Methods

EFL Experiments were performed in a parallel plate capacitor geometry, where PDMS coated ITO serves as a bottom electrode and bare ITO coated glass serves as a top electrode that confined ~ 5 µl of 4-Cyano-4'-pentylbiphenyl liquid crystal (5CB LC, Sigma-Aldrich, 99.99% pure). The experimental temperature was maintained at 23 ± 1 °C, at which the LC was in the nematic phase. A constant gap of ~35 µm between two ITO coated glass slides was maintained using polyimide spacers. A high voltage power source (HVPS, model EHT-11, SES Instruments Pvt. Ltd., India) was used to supply the DC voltage across the electrodes. A schematic of the experimental set-up is shown in Figure 5.1. A voltage of up to 300 V was used in all of the experiments with the ramping rate of ~2 V/s unless otherwise stated. The images and videos were recorded in reflective mode, using polarized light as well as in bright field settings, by Leica DM2500 M microscope, equipped with Leica DFC450 C camera having a CCD sensor.

For ECLL experiments, the same experimental arrangement as that of EFL was used. In this case, 300 V was applied first, and subsequently, LC was injected through the gap between PDMS and the top electrode. The motion of the LC could also be controlled by capillary pressure using the slightly wedged geometry of the

TH-2671_146153005

electrodes. The speed of the PDMS-5CB-air contact line was varied from ~ 2 μm/s to 50 μm/s by controlling the injection rate of LC.

5.2.3. Characterizations

Once the microstructure was formed at the LC-PDMS interface, the voltage supply was turned off, and the top electrode was removed carefully. To investigate the morphology of the PDMS thin film, the 5CB liquid crystal was first removed from the viscoelastic PDMS samples with the help of a filter paper. Subsequently, the deformed PDMS film was exposed to UV-Ozone for 20 min to petrify the structures by oxidizing the top silicone layer to silica.[44] The UV-Ozone treatment of the sample was performed within a very short time, which was much smaller than the relaxation time scale of the deformed PDMS. After the UV-Ozone treatment, the viscoelastic thin film was washed with Dimethyl sulfoxide (DMSO, Merck, India), a polar aprotic solvent, to remove excess 5CB LC without swelling the PDMS.[45] It also rendered a skin to protect the remaining silanol groups (if any) on the PDMS surface. Atomic Force Microscope (Model: Innova Iris, Bruker-Icon Analytical Equipment) was used to characterize the topography of the PDMS surface.

5.3. Results and discussion

5.3.1. The phenomenon

A ~ 5 μl 5CB droplet was dispensed on the PDMS film adhered to the ITO-glass bottom electrode, and another ITO-glass substrate (or top electrode) was brought to sandwich the 5CB layer and PDMS film between the electrodes. A constant separation distance of ~35 μm was maintained with the help of polyimide spacers. The experimental set-up very closely resembled the EWOD arrangement[41] but with a flat top electrode. This arrangement also mimicked very widely employed hybrid cells for LC applications.[40] It is well known that 5CB on untreated PDMS surface anchors in the homeotropic[46,47] manner while they do planer anchoring[48] on the pristine ITO-glass surface. Figure 5.2a shows the plausible director orientations in the 5CB layer in which the

TH-2671_146153005

LC molecules are showing homeotropic (planar) anchoring at the 5CB-PDMS (ITO-5CB) interface. Except at the solid-LC interfaces, the average orientations of directors were expected to be $0° < \theta < 90°$, where θ is the tilt angle of the director in the bulk nematic domains.

Before the experiments were initiated, in the absence of the electric field exposure, the bulk of the 5CB was in the nematic state and had a lateral variation of the director field of the LC owing to the local nematodynamics, as shown in the Figure 5.2a. When the electric field was applied through the electrodes, a set of very interesting events simultaneously took place,

(i) firstly, beyond a critical field intensity, the LC layer underwent a Fréedericksz phase transition wherein the directors of 5CB aligned in the direction of the applied electric field (Figure 5.2b);

(ii) secondly, the EHD stress at the PDMS-5CB interface led to the formation of micro/nano dimples/wells away from the contact line, which was similar to previously reported EFL (Figure 5.2c);[49]

(iii) thirdly, the Maxwell stress at the PDMS-5CB-air contact line created excess pressure drop to set in the reduction of the contact angles at both the confining surfaces similar to electrowetting and spreading of 5CB layer took place;

(iv) the Maxwell stress, owing to the presence of very high dielectric contrast at the PDMS-5CB-air contact line, instigated the periodic fingers of 5CB at the advancing front, and eventually, micro/nano dimples/wells started appearing beneath the periodic 5CB fingers.

Under the application of electric field, 5CB molecules on flat PDMS experienced one director gradient near the top ITO electrode, whereas the molecules exhibited another extra director gradient near the PDMS surface due to the dimple shape curvature of the surface. This appeared as the radial structure under a polarized optical microscope (POM). A schematic of the plausible arrangement of the 5CB molecules during this phenomenon is shown in Figure 5.2c.[47,50] Figure 5.2d depicts the polarized optical micrograph of 5CB filled microwell

TH-2671_146153005

created by the EFL method. The arrangement of the microwells was mostly hexagonal with long-wave instability accompanied by some defects (Figure 5.2d).

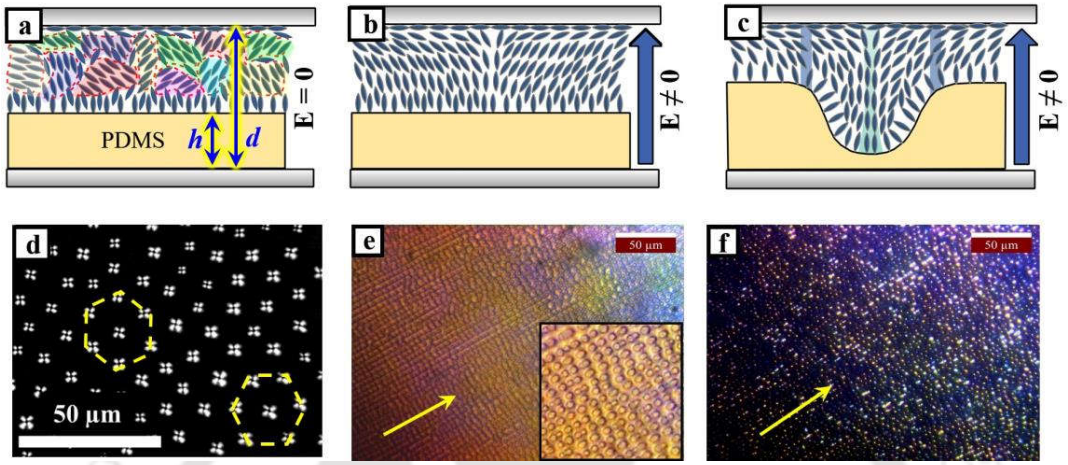

Figure 5.2 (a) Schematic representation of the nematic domains in LC in the absence of an electric field. (b) Schematic depiction of Fréedericksz phase transition in NLC in the presence of the electric field. (c) Deformed NLC-PDMS interface and the plausible LC molecular arrangement that gives rise to the radial structure in Polarized Optical Micrograph (POM). Figure (d) represents POM of LC filled microwells fabricated by the EFL method at an applied electric potential of 300 V and PDMS film thickness of ~ 8 µm. EFL induced morphology depicts mostly hexagonal arrangement of microwells accompanied by some defects. (e) Bright-field image during ECLL experiment and (f) polarized optical micrograph (POM) of 5CB filled orderly arranged microwells (formed by ECLL method) after careful removal of the top electrode and excess LC. These microwells are spanning over a large area of the PDMS surface. The initial film thickness was ~ 4 µm. The yellow arrow shows the direction of the 5CB-PDMS-Air contact line motion (see text for the details). The magnified inset (50 µm × 50 µm) of Figure 5e clearly shows the one-dimensional array of microwells.

Remarkably, while the 5CB front started spreading rapidly and periodic 5CB fingers transiently started appearing along the advancing contact line, they ejected 5CB droplets in the near vicinity of the contact line on the PDMS surface; we call it "electrospitting." In due course of time, at a given electric field, the 5CB layer,

TH-2671_146153005

confined between two perfectly parallel surfaces (ITO electrode and PDMS layer), reached an equilibrium, and the periodically undulated dynamic PDMS-5CB-air contact line became stationary. At this point, continuous injection of the more 5CB liquid crystal in between the top ITO electrode and the PDMS surface, instigated the Poiseuille flow that drives the periodically undulated contact line to forward direction while ejecting the 5CB droplets. In a short time, these ejected droplets coalesced with the advancing front before another new set of 5CB fingers are formed. The creation of periodic 5CB fingers on the contact line, ejection of the array of 5CB droplets, and coalescence of them with the advancing front kept on happening time-periodically leading to the emergence of the maskless patterning process, also termed here as ECLL. In this case, due to continuously controlled injection of the 5CB in between the confining parallel surfaces, the mass addition of LC prevented the thinning down of the LC layer during spreading, thus maintained its LC-PDMS bilayer arrangement throughout the experiment. The speed of the contact line motion was controlled by the rate of LC injection. The advancement of the contact line could also be achieved by the slightly wedged geometry of the confining surfaces of the 5CB due to the excess capillary pressure. In this wedged geometry arrangement, the whole 5CB layer moved toward the smaller spacing between the confining ITO and PDMS surfaces from the larger spacing regime, thus maintained the conservation of LC. Along with the Poiseuille flow or flow due to capillary pressure electrospreading due to the electromechanical force also engendered because of the non-uniform electric field at the three-phase contact line. We use the term "electrospreading" instead of "electrowetting" as the term "electrowetting" should rather be used only when the change of contact angle is concerned due to the electric field.[51] Here although the change in contact angle was coupled, the pressure-driven dynamic electrospreading front of dielectric NLC led to the template less long-range ordering of micro to nanoscale wells on the PDMS surface, as evident from the bright field and polarized optical micrograph (POM) of microwells shown in the Figure 5.2 e, f. The Figure 5.2f was recorded after careful removal of the top electrode and removal of the excess LC by soaking with filter paper. The figures and videos observed so far suggested that the ECLL was very different from previously reported EFL, and the process was capable of self-organizing large-area periodic patterns on a polymer surface with long-range ordering. In a way, while at the base of the stationary 5CB layer, we observed the traditional EFL, near the advancing electrospreading

TH-2671_146153005

front, the newly identified ECLL pathway of micro/nano-fabrication was observed. In what follows, we explore deeper into the origin of such a phenomenon, the length and time scales, the sensitivity parameters, and some applications.

5.3.2. Length and Time scales of EFL

The EFL of the soft-interface of a PDMS-5CB bilayer sandwiched between a pair of electrodes has been one of the very difficult systems to explore theoretically. However, the theoretical length scale for EFL associated with the fastest-growing dominant wavelength λ_{max} for an isotropic bilayer is well established.[16,19,20,24,29,52–54] In this study, we compare and contrast such a length scale associated with isotropic bilayer with the EFL observed for the PDMS-5CB system, assuming that the nematodynamics has limited influence on the length scales of the pattern formation. In all the experiments reported here, we used relatively thick layers (h >> 10 nm) of PDMS as well as 5CB. In this scenario, in comparison to the electrostatic force and interfacial tension, other forces such as van der Waals interactions and hydrostatic force can be neglected. Following previous studies, as the viscosity of LC, $\mu_{LC} << \mu_{PDMS}$, the linear dispersion relation associated with an isotropic bilayer for EFL is given by, $\omega = \frac{h^3}{3\mu}\left[-\frac{\partial P_{el}}{\partial h}k^2 - \gamma k^4\right]$, where ω and k represent growth coefficient and wavenumber of perturbation, respectively, while μ_{PDMS} and h are viscosity and thickness of the PDMS film. The parameter P_{el} is the excess electrostatic pressure at the interface due to the application of the electric field. The necessary condition for the destabilization of the interface is, $\frac{\partial P_{el}}{\partial h} < 0$ and $\left|\frac{\partial P_{el}}{\partial h}\right| > \gamma k^2$, and λ_{max}, corresponding to the maximum growth coefficient, has been obtained by setting $\frac{\partial \omega}{\partial k} = 0$ and $\frac{\partial^2 \omega}{\partial k^2} < 0$ at $\frac{\partial P_{el}}{\partial h} = -2\gamma k^2$, which follows:

TH-2671_146153005

$$\lambda_{max} = \frac{2\pi\sqrt{2\gamma\{\varepsilon_2 d + h(\varepsilon_1 - \varepsilon_2)\}^3}}{\sqrt{V^2\varepsilon_0\varepsilon_1\varepsilon_2(\varepsilon_1 - \varepsilon_2)^2}} \quad . \qquad (1)$$

Here V is the applied bias voltage, ε_0 is the dielectric permittivity of the vacuum, $\varepsilon_1, \varepsilon_2$ are the dielectric constants of 5CB and PDMS, γ is the interfacial tension at PDMS-5CB interface, and d is the separation distance between the electrodes.

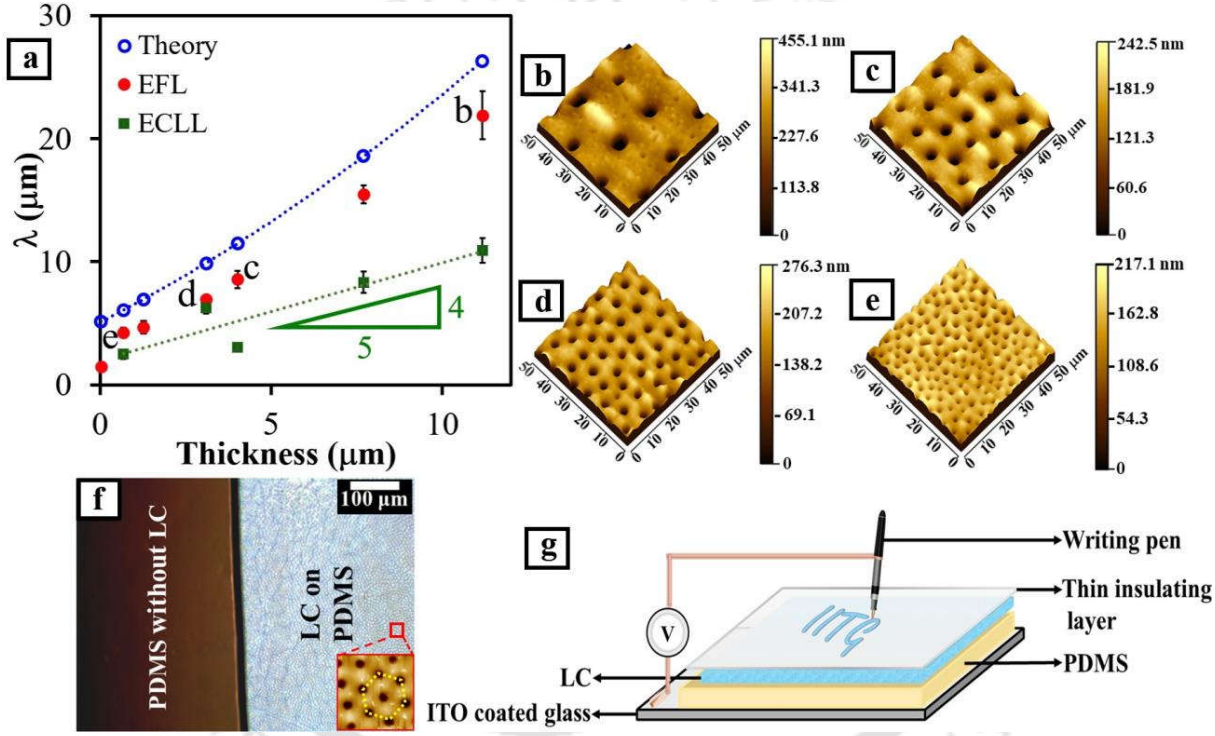

Figure 5.3 Characteristic wavelength (λ) of the morphology against the PDMS film thickness is shown in Figure (a). The blue open circles with dotted line depict a theoretical estimation of λ_{max} based on Eq.1 corresponding to the experimental geometry of fixed electrode distance of d = 35 μm and applied voltage = 300 V. The red filled circles represent experimental EFL data for the viscoelastic PDMS films. Few representative AFM images of PDMS films having thickness ~ 11.2 μm (b), ~ 4 μm (c), ~ 3 μm (d), and ~ 0.7 μm (e) are shown, mean wavelengths of which are pointed out in Figure (a). The green squares depict the separation distance between two neighboring lines of microstructures engendered from ECLL (see text). The Green dotted straight line is an aid to interpret the discrete data with a slope of ~ 0.8, representing $\lambda_C \sim 0.8\, h$. Figure (f) shows morphological

TH-2671_146153005

patterns developed on the PDMS covered by LC only (EFL experiment). PDMS free surface under air remained stable in the presence of the same external electric field. AFM image (25 μm × 25 μm) of the topography of the PDMS surface, which was covered by LC during the EFL experiment, is shown in the inset. (g) Schematic of the experimental set-up for "E-writing" (see text for detail).

The hollow blue circles with the dotted line in Figure 5.3a shows that the theoretical predictions for the isotropic bilayer somewhat over predicts the length scales associated with the EFL with the ones obtained experimentally for the PDMS-5CB system (filled circular symbols in red). The theoretical expression shown in the Eq. (1) suggests that λ_{max} to be ~ 5 μm when h ~ 0.03 μm until λ_{max} to be 26 μm when h ~ 11 μm, which is marginally higher than the one obtained through experiments. The AFM images Figure 5.3b to 5.3e show the signatures of EFL at the base of the 5CB layer and away from the contact line. Here a high dielectric contrast ($\varepsilon_{\|} = 19.7$ for 5CB,[40] and $\varepsilon = 2.65$ for PDMS[42]) across the 5CB-PDMS interface ensures that the dimples are formed on the lower dielectric PDMS surface. Theoretical calculation using Eq.1 for the Air-PDMS system reveals that the length scale of morphology obtained using the LC-PDMS system is about two orders of magnitude smaller than that for the Air-PDMS system (Figure 5.4a).

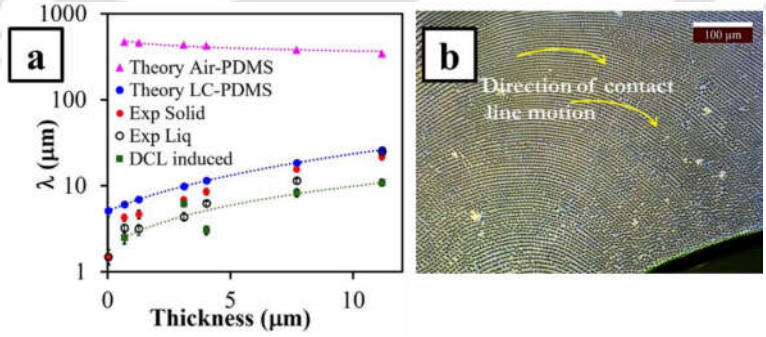

Figure 5.4 (a) Wavelength (λ) of the structures against the PDMS film thickness. The pink triangle with a pink dotted line depicts theoretical estimation based on equation 1 corresponds to the experimental geometry of fixed electrode distance of d = 35 μm and varying PDMS film thickness with an air gap instead of LC. The blue

TH-2671_146153005

circle with a blue dotted line shows theoretical estimation with LC without any air gap. This reveals that LC-PDMS system can give rise to microstructures having a length scale ~ 100 times smaller than that by the air-PDMS system. The red circles are the experimental data for the viscoelastic solid PDMS film with relatively higher elastic component. The black open circles are the experimental data with viscoelastic liquid PDMS film having relatively lower elastic component. The green squares depict the separation distance between two neighboring lines of microstructures engendered from the electric field and dynamic contact line (EF-DCL) induced instability (see text). (b) The curved arrangement of the microwells is achieved by driving the contact line in the curved pathway. This shows the flexibility and versatility of the ECLL method for different micro/nano patterning on demand.

Interestingly, a lower interfacial tension ($\gamma_{PDMS/LC}$ = 4.5 mN/m[55]), and a fluctuating higher dielectric contrast at the 5CB-PDMS interface, also leads to faster kinetics of the pattern formation. The PDMS film underneath the 5CB layer almost instantaneously undergoes deformation to produce patterns. This observation is quite unlike the previously reported polymer-air or polymer-polymer isotropic systems, where the kinetics of the instability was rather slow owing to the higher surface/interfacial tension and lower deterministic dielectric contrast. In fact, Figure 5.3f shows that the PDMS-air interface is absolutely stable when the patterns are formed under the 5CB layer while influenced by the same external electric field exposure, indicating faster kinetics for the 5CB-PDMS interface. Assuming $\mu_{LC} << \mu_{PDMS}$, from the linear dispersion relation, one can estimate the maximum growth coefficient ω_{max} from the following equation:

$$\omega_{\max} = \frac{h^3}{12\mu\gamma} \frac{\left[V^2 \varepsilon_0 \varepsilon_1 \varepsilon_2 (\varepsilon_1 - \varepsilon_2)^2\right]^2}{\left[\varepsilon_2 d + h(\varepsilon_1 - \varepsilon_2)\right]^6} \tag{2}$$

Using maximum growth coefficient, one can estimate the time scale of instability, τ_d, as:

$$\tau_d = \frac{1}{\omega_{\max}} \ln\left(\frac{h}{\in}\right) \tag{3}$$

TH-2671_146153005

Where $\in$ is the amplitude of the initial perturbation. Using eq. 3, for a 3 μm film, the estimated τ_d for the LC-PDMS system is ~ 44 ms whereas the same for the Air-PDMS system is ~ 10.3 h. The initial amplitude of perturbation, $\in$, for both the system is kept identical for this estimation (5 nm). As a word of caution, this estimation of τ_d is from the linear stability analysis, and hence, it should be taken as the first approximation of the time scale for destabilization. Nevertheless, this estimation shows that kinetics of destabilization for the Air-PDMS system is an order of magnitude slower than that of the LC-PDMS system.

It may also be noted here that the LC directors are not unidirectional rather fluctuating locally, although the time-averaged, as well as the space-averaged direction of the director, aligns with the applied electric field. As a result, at any given instance, the distribution of the local domains is observed. This fluctuation of directors somewhat diminishes with the increasing electric field intensity. In their seminal contributions, Frank[56] and Meyer[57] reported that polar or apolar LCs may splay out uniformly, but no stable three-dimensional structures are possible with uniform splay out configuration. Therefore, liquid crystals form isolated domains with the optimum splayed structure to accommodate the three-dimensional space at any given instant. As the dielectric permittivity of LC is a function of the orientation of the director, a sharp gradient in dielectric permittivity, as well as electrostatic pressure, is induced across the LC domain boundaries. Thus, noisy director fluctuation across the LC domain boundaries in conjunction with the high dielectric contrast across the 5CB-PDMS interface could be the reason for the faster deformation kinetics. Importantly, the time scale of the noise activated deformation τ_d is of the order of a few seconds in the 5CB-PDMS system compared to minutes or hours in case of the air-PDMS system. Noise activated escape to overcome the attenuated effective energy barrier,[58–60] in dissociation[61] or translocation [62,63] processes have already been reported in the literature. On similar lines, for the 5CB-PDMS system, the LC layer imparts fluctuation of the effective energy barrier for the deformation of the interface and induces faster kinetics.

As the time scale of deformation or instability (τ_d) is very small with NLC as the top layer, we employed an experimental set up to create micro-pattern on-demand using electric field induced writing named "E-writing"

TH-2671_146153005

(Figure 5.3g). Here a polymer thin film substrate was sandwiched between a flat electrode and a thin layer of LC with high dielectric constant. A micro/nano tip, which served as a counter electrode, was used as a pen to write on a thin, rigid insulating layer placed on top of the LC layer. This pen and the bottom flat electrode when connected with a voltage source, created an array of micro/nanostructures following the writing path of the pen on the thin polymer substrate. The time scale of writing ($\tau_w = \frac{\lambda_{max}}{v_w}$), has to be larger than the time scale of deformation(τ_d). Here v_w denotes the writing speed for "E-writing".

5.3.3. Maskless patterning using ECLL

As discussed in the earlier section, upon application of electric field, the 5CB layer electrospread on the PDMS film when the electric field was applied. During electrospreading, the formation of periodic 5CB fingers on the contact line, ejection of the array of 5CB droplets in front of the fingers (electrospitting), and coalescence of them with the advancing contact line leading to the maskless writing process ECLL. A time series of the contact line motion is shown in Figure 5.5a to 5.5c. In the process, the advancing electrospreading front of the 5CB layer left a well-organized one-dimensional array of microwells by forming a microwell at each lobe of the 5CB finger, as shown in Figure 5.5d. The direction of the array of these micro to nanostructures formed was perpendicular to the 5CB-PDMS-air contact line. A few previous studies had already reported the electric field induced fingering instability of viscoelastic films[52] in which the adhesion front was found to undergo edge straightening, finger elongation or pillar formation as the stiffness parameter (μ/h) of the film reduced. Further, an ad-hoc calculation using the experimental parameters following Fields and Ashby[64] revealed that the wavelength of the patterns formed due to fingering instability should be of the order of a few mm. However, in the present scenario, the observed length scale (λ_c, the average spacing between two adjacent parallel arrays of the micro-wells) was ~ 1000 times smaller while it also showed a linear dependence with the PDMS film thickness, as shown in the Figure 5.3a. Thus, we investigated a little deeper to find out the physics associated with the ECLL phenomenon.

TH-2671_146153005

It is well known that in electrowetting the droplet spreads owing to the development of additional Maxwell stress at the three-phase contact line. In a way, the EHD stress originating from the electric field ($\sim \frac{\varepsilon V^2}{2h}$, ε , being the dielectric permittivity of the insulating coating) overpower the thermodynamic equilibrium at the three-phase contact line, decided by the surface tension forces of 5CB and PDMS, to stimulate the spreading of the 5 CB. Previously, a simplistic linear stability analysis[65] of the contact line of a water droplet revealed that the critical wavenumber (k_c) of the distortion of the contact line under the influence of an external electric field could be, $k_c = \frac{2\pi}{\lambda_c} \simeq \frac{1}{\xi}$, where ξ is the electrostatic screening length and of the order of the thickness of the insulating layer ($\xi \sim h$). Thus, the critical wavelength $\lambda_c \sim h$ has been routinely observed when the water droplets undergo electrowetting and the fingers are formed. Figure 5.3a also shows that for the 5CB-PDMS system, $\lambda_c \sim 0.8h$, which means that the analysis remained valid even for the electrospreading of 5CB. This is because, near the three-phase contact line, the presence of the electrospreading fluid is somewhat minimal, while the EHD stresses were largely dictated by the thickness of the dielectric layer and the applied field intensity. Thus, the predictions associated with the spacing of the fingers issuing out of a water droplet or 5CB were found to be of the order of the thickness of the dielectric layer. Importantly, the aforementioned analysis corroborated that the finger formation at the advancing front of the 5CB layer was indeed short-wave in nature as, $\lambda_c \sim h$. Consequently, while a micro-thick PDMS film led to fingers with microscale spacing, the spacing could be reduced to the nanoscale by coating a nano-thick PDMS film.

TH-2671_146153005

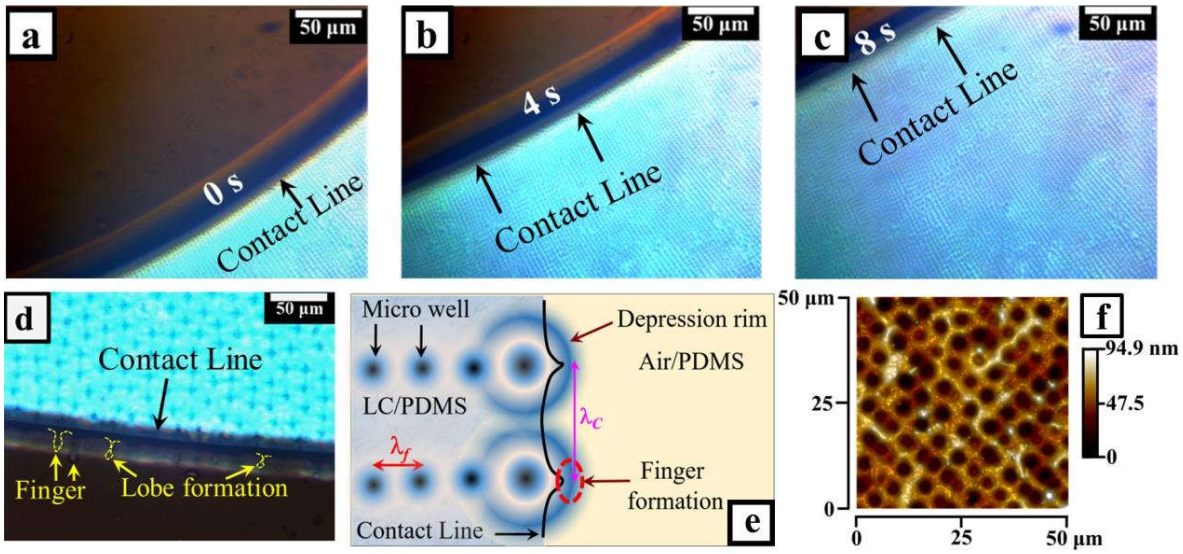

Figure 5.5 ECLL induced template-less pattern formation in LC-PDMS bilayer system. Figures (a-c) show the time series of a moving contact line and a one-dimensional array of microwell formation. (d) Reveals the formation of fingers and lobes, which eventually induce the formation of microwell on the PDMS interface. A schematic representation of the mechanism is depicted in Figure (e) (see text). AFM image of the one-dimensional array of microwells formed by ECLL is shown in Figure (f).

After the formation of the fingers, we observed an "electrospitting" of an array of small droplets in front of the advancing contact line of LC. Similar phenomena were reported previously for the electrowetting of deionized water and known to be suppressed for the saline water.[65,66] The formation of fingers and lobes of LC from the three-phase contact line before the ejection of the droplets were observed under the influence of the electric field, as shown in Figure 5.5d. With progress in time, the array of these ejected droplets coalesced with the advancing contact line. Subsequently, the experiments uncovered that, during this process, the formation of the dimples/indents took place exactly at the places where the array of 5CB droplets were ejected during electrospitting. Thus, the periodicity of the dimples/indents were found to follow the short-wave nature identical to that of the fingers, i.e., λ_c varies linearly with the thickness of the PDMS having a slope of ~ 0.8.

TH-2671_146153005

It may be noted here that EFL mostly showed long-wave hexagonal patterns at the polymer-polymer or polymer-air interfaces in the absence of patterned electrodes.[16] These patterns form small isolated 2D crystal-like domains with grain boundaries, and these isolated domains are initiated by the randomly formed single structure due to initial surface fluctuation.[67] In comparison, the ECLL led to a large area 1D array of microwells, initiated by the "edge effect" of the dynamic 5CB-PDMS-air contact line. As the contact line moved, the new arrays of the dimples/indents/microwells appeared due to the time-periodic finger formation, electrospitting, and coalescence of the droplets with the advancing front. Whenever one micro-well appeared under the LC phase near the contact line, isotropically a circular rim formation took place surrounding the newly formed well. Subsequently, radially further away from the center of the well, local circular depression was observed surrounding the rim. In such a scenario, the presence of contact line broke the symmetry of the isotropic circular depression surrounding the wells to initiate the formation of the new fingers of 5CB in the direction of the contact line motion. Such occurrences happened at the closest depression zone accessible, i.e., in the immediate frontal position of the previously formed microwell, as schematically shown in Figure 5.5e. Subsequently, a new set of dimple/indent/microwell formation took place at the lobes of the fingers, following the previous set of dimple/indent/microwell. AFM image of such an ECLL induced patterned surface is shown in Figure 5.5f.

Importantly, the edge effect at the vicinity of the local depression beyond the rim also induced a significant reduction of the wavelength, as compared to the natural deformation wavelength of a stationary LC film (EFL) (Figure 5.3a). This observation is similar to the pattern directing deformation or replication, reported earlier, where the rigid patterned electrode was used, and the width of the pattern influenced the wavelength of the morphologies.[22,25] The only exception is that there is no pre-patterned electrode employed in the present case. Instead, we employed the dynamic contact line of 5CB-PDMS-air as the soft template for pattern formation. The destabilization of the contact line being the guiding star for the formation of the dimple/indent/microwell, the pattern could be generated as desired by controlling the local curvature of the LC layer. Interestingly, some preliminary experiments (not reported here) also revealed that the in-line wavelength (λ_f), defined as the mean

TH-2671_146153005

separation distance between two subsequent microwells in the same array (see Figure 5.5e), and the dimension of the structure were weakly sensitive to the speed of the LC front (v_f). An extensive study on the dependency of the characteristic length scale of the morphology on the velocity of the contact line is reserved for our next report.

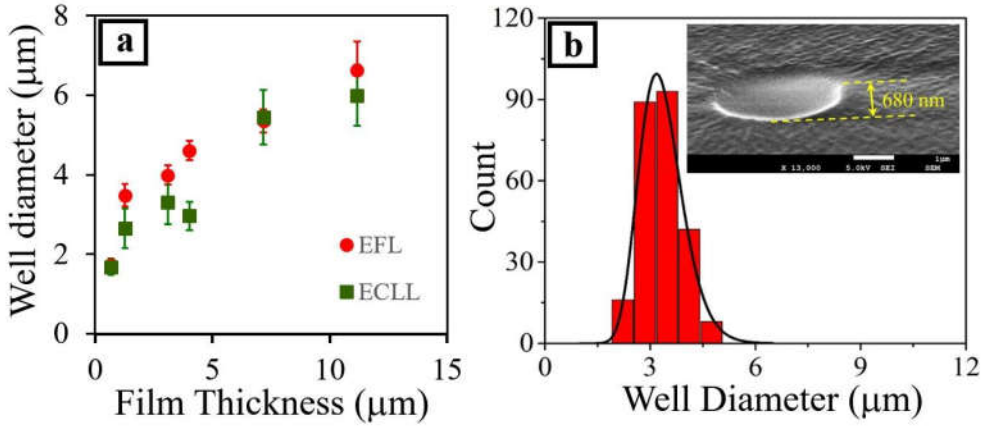

Figure 5.6 (a) Microwell diameter against the initial film thickness is shown both for EFL (red circle) and ECLL (green square). (b) Distribution of microwell diameters obtained from 250 microwells fabricated by the EFL method using a PDMS film of thickness ~3 μm. In the inset, a FESEM image is showing the cross-section of a microwell from the same sample.

To characterize the feature size, we compared the diameter of microwells obtained from EFL and ECLL methods for different film thicknesses. Surprisingly, it was found that although the center to center distance of the microwells (wavelength, λ) differs widely (Figure 5.3a), the diameter of the microwells was almost comparable (Figure 5.6a) for both EFL and ECLL. A representative microwell diameter (D_w) distribution was shown in Figure 5.6b for a film of the initial thickness of ~3 μm. The microwells were fabricated by the EFL method. It was observed that the distribution of the D_w was quite narrow for the film in spite of the limited statistics of 250 microwells. FESEM image of a single microwell from the same sample (Figure 5.6b inset) also revealed that the depth of the microwell is ~ 680 nm.

TH-2671_146153005

To summarize, the key similarities and contrasts between the ECLL and the EFL:

(i) The EFL induces long wave hexagonal arrangement of the structures, whereas the ECLL kindles the one-dimensional patterning with short-wavelength scale without any template. One dimensional arrangement of the microwells using EFL is only possible with the help of a templated substrate or by using a templated top electrode. Fabrication of templated electrode or substrate itself requires another lithographic technique.

(ii) Although the feature size, i.e., the diameter of the microwells, is comparable for both EFL and ECLL methods (Figure 5.6a), the periodicity of the morphology obtained from EFL is much larger than that obtained from ECLL (Figure 5.3a).

(iii) One can control the direction of the LC-PDMS-Air contact line motion and can create versatile patterns on demand. A circular bend arrangement of the micro-wells is shown in Figure 5.4b, where the microwells were fabricated by driving the three-phase contact line following an arc.

5.3.4. Solvent induced switching-pixelation

Being an electroactive material, LC is already used in smart display, where an individual pixel can be controlled electronically using a thin film transistor (TFT). In this regard, the solvent vapor induced or thermal phase transition in LC droplets have already been reported earlier.[68,69] Here, we demonstrate that the array of LC filled microwell can be used as a prototype of pixelated display that can be switched off or on in the presence or absence of solvent vapor.

Figure 5.7 Polarized optical microscope image of 5CB filled array of microwells, serve as light-reflecting pixels. Upon exposure to the solvent (n-hexane), the nematic to isotropic (N-I) transition takes place at 120 s (Figure

TH-2671_146153005

a, b, c) and withdrawing the solvent source kindles the array of reflecting lights again due to I-N phase transition (Figure c, d, e).

After the fabrication of a one-dimensional array of microwells on the PDMS surface by ECLL, the excess 5CB was removed by soaking with filter paper. This left an array of dimples/indents/microwells on the PDMS surface filled with 5CB. This structured PDMS surface was then observed under the POM in reflecting mode. The small nematic 5CB domains in the microwell reflected the polarized light, as shown in Figure 5.7a. At this stage, the sample was kept in a closed chamber filled with hexane vapor. The partial pressure of n-hexane within the chamber was maintained at ~18 kPa. Subsequently, solvent vapor was absorbed by the LC filled microwell and a nematic to isotropic (N-I) transition of the 5CB took place within 120 s of the vapor exposure (Figures 5.7b and 5.7c), and no light was reflected by the LC domains. A gradual decrease of the light intensity was observed in Figure 5.7b, and a complete dark (switch off) display was depicted by Figure 5.7c. Upon removal of the solvent vapor source, the isotropic to nematic (I-N) transition took place due to desorption of the solvent vapor and again, the reflected light reappeared (Figures 5.7d and 5.7e) at 240 s. Here a point to note that the switching off and on the reflecting light was solely due to the N-I and I-N transition of nematic liquid crystal in the presence or absence of the solvent vapor, respectively. What is important here is that one can fabricate the well-ordered array of micro pixels and can control the pixel size of the display by controlling the arrangement and diameter of microwell, respectively.

5.5. Conclusions

This study demonstrates an ultrafast, template-less technique, called ECLL, to fabricate ordered micro/nanopatterns on the thin polymer surface. Dynamic electrospreading of periodic NLC front is used as a soft template to create ordered patterns at the interface of the NLC-PDMS in electric field induced instability settings. The faster kinetics of the destabilization due to the high dielectric contrast at the interface of NLC-PDMS layers along with the local fluctuation of the highly dielectric NLC domains, make ECLL a novel

TH-2671_146153005

technological tool for miniaturized mesoscale patterning of a thin polymer film. This inherent expeditious nature of this NLC-PDMS system for the EHD destabilization of the interface also allows one to write (E-writing) on the polymer surface using an insulated electrode tip as a pen. In contrast to the conventional EFL experiments, which follows long-wave characteristics with a hexagonal arrangement of microstructures, ECLL shows a short-wave length scale with $\lambda_c \sim 0.8h$. A simple linear stability analysis reasonably predicts the length scale of the destabilization of the NLC-PDMS interface following conventional EFL and also of the NLC-PDMS-Air three-phase contact line following ECLL. The in-line wavelength (λ_f)of the micro/nano-wells formed by ECLL is weakly sensitive to the velocity of the LC spreading front, characterization of which needs extensive study and is reserved for our future publications. The ECLL induced patterning can have significant potential in the fabrication of MEMS/NEMS, optoelectronics, microsensors, etc. We have demonstrated one such application by fabricating the array of solvent responsive light-reflecting micropixels.

TH-2671_146153005

References

[1] A. M. Turing, *Philos. Trans. R. Soc. Lond. B. Biol. Sci.* **1952**, *237*, 37.

[2] G. François, B. P.-T., *Philos. Trans. R. Soc. A Math. Phys. Eng. Sci.* **2017**, *375*, 20160155.

[3] L. N. Guin, *Appl. Math. Comput.* **2014**, *226*, 320.

[4] A. Solga, Z. Cerman, B. F. Striffler, M. Spaeth, W. Barthlott, *Bioinspir. Biomim.* **2007**, *2*, S126.

[5] D. Franklin, Y. Chen, A. Vazquez-Guardado, S. Modak, J. Boroumand, D. Xu, S.-T. Wu, D. Chanda, *Nat. Commun.* **2015**, *6*, 7337.

[6] T. Makarczuk, T. R. Matin, S. B. Karman, S. Z. M. Diah, B. Davaji, M. O. Macqueen, J. Mueller, U. Schmid, I. C. Gebeshuber, in *Proc. SPIE*, **2011**, p. 80661O.

[7] T. Ponnusamy, G. Chakravarty, D. Mondal, V. T. John, *Adv. Healthc. Mater.* **2014**, *3*, 703.

[8] H. Zhang, L. Xu, Y. Xu, G. Huang, X. Zhao, Y. Lai, T. Shi, *Sci. Rep.* **2016**, *6*, 1.

[9] R. Mukherjee, A. Sharma, *Soft Matter* **2015**, *11*, 8717.

[10] R. Deb Roy, D. Sil, S. Jana, N. Bhandaru, S. K. Bhadra, P. K. Biswas, R. Mukherjee, *Ind. Eng. Chem. Res.* **2012**, *51*, 9546.

[11] N. A. Malvadkar, J. Hancock, Matthew, K. Sekeroglu, W. J. Dressick, M. C. Demirel, *Nat. Mater.* **2010**, *9*, 1023.

[12] M. A. Herman, W. Richter, H. Sitter, *Epitaxy—Physical Principles and Technical Implementations*, Springer, Berlin, **2004**.

[13] O. Custance, R. Perez, S. Morita, *Nat. Nanotechnol.* **2009**, *4*, 803.

[14] B. Moores, J. Simons, S. Xu, Z. Leonenko, *Nanoscale Res. Lett.* **2011**, *6*, 185.

[15] J. M. Reynolds, *Phys. Fluids* **1965**, *8*, 161.

TH-2671_146153005

[16] N. Arun, A. Sharma, P. S. G. Pattader, I. Banerjee, H. M. Dixit, K. S. Narayan, *Phys. Rev. Lett.* **2009**, DOI 10.1103/PhysRevLett.102.254502.

[17] E. Schaffer, T. Thurn-Albrecht, T. Russell, U. Steiner, *Nature* **2000**, *403*, 874.

[18] J. Sarkar, A. Sharma, V. B. Shenoy, *Phys. Rev. E* **2008**, *77*, 1.

[19] R. Verma, A. Sharma, K. Kargupta, J. Bhaumik, *Langmuir* **2005**, *21*, 3710.

[20] G. Tomar, V. Shankar, A. Sharma, G. Biswas, *J. Nonnewton. Fluid Mech.* **2007**, *143*, 120.

[21] A. Ramkrishnan, S. Kumar, *Phys. Fluids* **2014**, *26*, 122110.

[22] P. S. G. Pattader, I. Banerjee, A. Sharma, D. Bandyopadhyay, *Adv. Funct. Mater.* **2011**, *21*, 324.

[23] K. Mondal, P. Kumar, D. Bandyopadhyay, *J. Chem. Phys.* **2013**, *138*, DOI 10.1063/1.4773857.

[24] S. Srivastava, P. D. S. Reddy, C. Wang, D. Bandyopadhyay, A. Sharma, *J. Chem. Phys.* **2010**, DOI 10.1063/1.3400653.

[25] M. D. Morariu, N. E. Voicu, E. Schäffer, Z. Lin, T. P. Russell, U. Steiner, *Nat. Mater.* **2003**, *2*, 48.

[26] M. D. Dickey, S. Gupta, K. A. Leach, E. Collister, C. G. Willson, T. P. Russell, *Langmuir* **2006**, *22*, 4315.

[27] Z. Lin, T. Kerle, T. P. Russell, E. Schäffer, U. Steiner, *Macromolecules* **2002**, *35*, 6255.

[28] P. D. S. Reddy, D. Bandyopadhyay, A. Sharma, *J. Phys. Chem. C* **2012**, *116*, 22847.

[29] D. Bandyopadhyay, A. Sharma, U. Thiele, D. S. Reddy, *Langmuir* **2009**, *25*, 9108.

[30] R. V. Craster, O. K. Matar, *Phys. Fluids* **2005**, *17*, 0.

[31] Q. Wang, L. Zhang, X. Zhao, *Phys. Rev. Lett.* **2011**, *106*, 1.

[32] Z. Lin, T. Kerle, S. M. Baker, D. A. Hoagland, E. Schärfer, U. Steiner, T. P. Russell, *J. Chem. Phys.* **2001**, *114*, 2377.

TH-2671_146153005

[33] N. Wu, W. B. Russel, *Ind. Eng. Chem. Res.* **2006**, *45*, 5455.

[34] P. van der Asdonk, H. C. Hendrikse, M. Fernandez-Castano Romera, D. Voerman, B. E. I. Ramakers, D. W. P. M. Löwik, R. P. Sijbesma, P. H. J. Kouwer, *Adv. Funct. Mater.* **2016**, *26*, 2609.

[35] T. Kato, Y. Hirai, S. Nakaso, M. Moriyama, *Chem. Soc. Rev.* **2007**, *36*, 1857.

[36] K. Akagi, G. Piao, S. Kaneko, K. Sakamaki, H. Shirakawa, M. Kyotani, *Science (80-.).* **1998**, *282*, 1683.

[37] S. Moynihan, P. Lovera, D. O'Carroll, D. Iacopino, G. Redmond, *Adv. Mater.* **2008**, *20*, 2497.

[38] M. A. Lohr, M. Cavallaro, D. A. Beller, K. J. Stebe, R. D. Kamien, P. J. Collings, A. G. Yodh, *Soft Matter* **2014**, *10*, 3477.

[39] M. D. Lynch, D. L. Patrick, *Nano Lett.* **2002**, *2*, 1197.

[40] L. M. Blinov, *Structure and Properties of Liquid Crystals*, Springer, **2011**.

[41] F. Mugele, J.-C. Baret, *J. Phys. Condens. Matter* **2005**, *17*, R705.

[42] R. Dey, U. U. Ghosh, S. Chakraborty, S. DasGupta, *Langmuir* **2015**, *31*, 11269.

[43] N. Bhandaru, S. Roy, Suruchi, G. Harikrishnan, R. Mukherjee, *ACS Macro Lett.* **2013**, *2*, 195.

[44] R. Mukherjee, A. Sharma, *ACS Appl. Mater. Interfaces* **2012**, *4*, 355.

[45] T. Honda, M. Miyazaki, H. Nakamura, H. Maeda, *Lab Chip* **2005**, *5*, 812.

[46] P. Dhara, N. Bhandaru, A. Das, R. Mukherjee, *Sci. Rep.* **2018**, *8*, 7169.

[47] Y. Xia, E. Lee, H. Hu, M. A. Gharbi, D. A. Beller, E.-K. Fleischmann, R. D. Kamien, R. Zentel, S. Yang, *ACS Appl. Mater. Interfaces* **2016**, *8*, 12466.

[48] H. Dreyfus-lambez, D. Stoenescu, I. Dozov, P. Martinot-Lagarde, *Mol. Cryst. Liq. Cryst. Sci. Technol. Sect. A. Mol. Cryst. Liq. Cryst.* **2000**, *352*, 19.

[49] Z. Lin, T. Kerle, T. P. Russell, E. Schäffer, U. Steiner, *Macromolecules* **2002**, *35*, 3971.

TH-2671_146153005

[50] A. D. Rey, *Soft Matter* **2010**, *6*, 3402.

[51] T. B. Jones, *Langmuir* **2002**, *18*, 4437.

[52] N. Arun, A. Sharma, V. B. Shenoy, K. S. Narayan, *Adv. Mater.* **2006**, *18*, 660.

[53] V. Shankar, A. Sharma, *J. Colloid Interface Sci.* **2004**, DOI 10.1016/j.jcis.2003.12.024.

[54] N. Wu, L. F. Pease, W. B. Russel, *Langmuir* **2005**, *21*, 12290.

[55] P. K. Rai, M. M. Denn, C. Maldarelli, *Langmuir* **2003**, *19*, 7370.

[56] F. C. Frank, *Discuss. Faraday Soc.* **1958**, *25*, 19.

[57] R. B. Meyer, *Phys. Rev. Lett.* **1969**, *22*, 918.

[58] B. Carmeli, A. Nitzan, *J. Chem. Phys.* **1983**, *79*, 393.

[59] G. Caratti, R. Ferrando, R. Spadacini, G. E. Tommei, *Phys. Rev. E* **1996**, *54*, 4708.

[60] P. Hänggi, P. Talkner, M. Borkovec, *Rev. Mod. Phys.* **1990**, *62*, 251.

[61] M. K. Chaudhury, P. S. Goohpattader, *Eur. Phys. J. E* **2012**, *35*.

[62] S. Lee, W. Sung, *Phys. Rev. E* **2001**, *63*, 21115.

[63] M. K. Chaudhury, P. S. Goohpattader, *Eur. Phys. J. E* **2013**, *36*, 15.

[64] R. J. Fields, M. F. Ashby, *Philos. Mag. A J. Theor. Exp. Appl. Phys.* **1976**, *33*, 33.

[65] M. Vallet, M. Vallade, B. Berge, *Eur. Phys. J. B - Condens. Matter Complex Syst.* **1999**, *11*, 583.

[66] M. Vallet, B. Berge, L. Vovelle, *Polymer (Guildf).* **1996**, *37*, 2465.

[67] K. A. Leach, Z. Lin, T. P. Russell, *Macromolecules* **2005**, DOI 10.1021/ma048157p.

[68] B. Ravi, S. Chakraborty, M. Bhattacharjee, S. Mitra, A. Ghosh, P. S. Gooh Pattader, D. Bandyopadhyay, *ACS Appl. Mater. Interfaces* **2017**, *9*, 1066.

TH-2671_146153005

[69] B. Ravi, M. Bhattacharjee, A. Ghosh, D. Bandyopadhyay, *Nanoscale* **2019**, DOI 10.1039/C8NR08400A.

भारतीय प्रौद्योगिकी संस्थान गुवाहाटी • Indian Institute of Technology Guwahati •

TH-2671_146153005

Chapter 6

TH-2671_146153005

Chapter 6

TEMPLATE-LESS CROSS-PATTERNING OF SOFT SURFACES BY THE FIELD DRIVEN DIRECTED CONFINED FLOW OF NEMATIC LIQUID CRYSTAL

Abstract

The origin of electric field induced interfacial instability in a confined bilayer system is studied in this chapter. The instability is generated due to Maxwell stresses at the interface for the imposed electric field. The bilayer consists of partially crosslinked Polydimethylsiloxane (PDMS) film (isotropic and having significant viscous and elastic component) and 5CB (4-Cyano-4'-pentylbiphenyl) nematic liquid crystal layer. Electric field induced motion of anisotropic nematic liquid crystal - wavefront on soft viscoelastic thin film has empowered to produce remarkable arrays of microwells on soft viscoelastic PDMS in any direction with high fidelity in wavelength and geometry of pattern. The present study also validates the genesis of fingering instability at PDMS/air/5CB contact line reported previously as ECLL (Electrodynamic-Contact-Line-Lithography) technique. Despite that, it is also shown that the injection of a perpendicular stream of 5CB to the ECLL patterned area under the electric field in the air can create cross patterns with sufficient accuracy. The easy applicability and flexibility in designing complex hierarchical structures open a new horizon for producing a tailor-made patterned surface for novel soft materials in microfluidics and soft lithography applications.

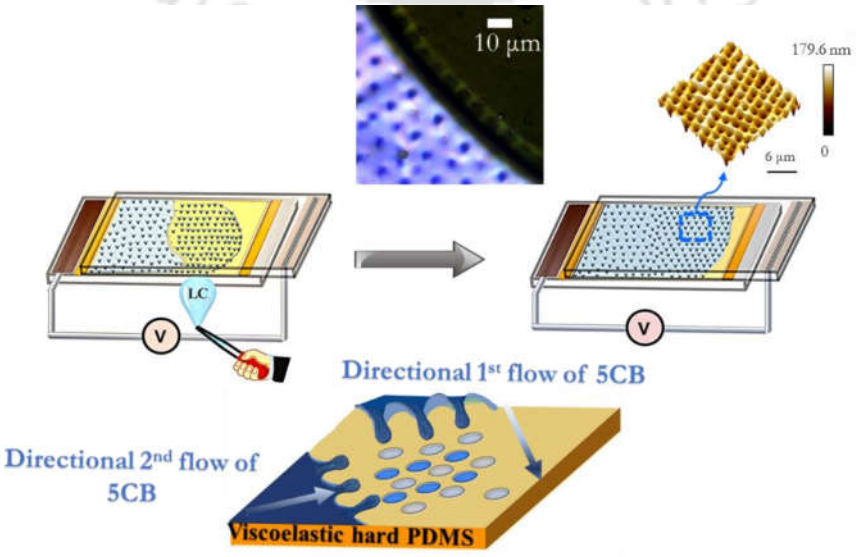

TH-2671_146153005

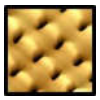

6.1. Introduction

Multiscale patterning over a large surface area has remained a long endeavor as many technologies require patterned surfaces. The advantage of fabricating a multiscale patterned surface is that the functionality of the surface inter alia depends on the structure's wavelengths. In this context, Nature has always inspired in displaying some excellent multiscale functional surfaces. The superhydrophobic surface of lotus leaf,[1] colorful structures of butterfly wing scale,[2] pressure-sensitive microfluidic adhesive[3] like Gecko pad, etc., are some of the prime examples of multiscale surfaces. Artificial fabrication of periodic structures of these kinds over a surface required the use of conventional patterning techniques. One of the top-down approaches which are heavily used in large scale to pattern surfaces is photolithography. Photolithography, though, is most efficient, is not an economical option when it comes to large area patterning since it involves high-end instrumentation and the use of harsh chemicals in multiple chemical treatment steps. In this regard, researchers have explored patterning in a non-photolithographic way for decades. Thus, a lot of attention has been given of late to create patterns on thin polymer surface mainly via the perturbation induced dewetting utilizing various instabilities,[4–13] employing capillary force lithography[14–16] and thermocapillarity,[17] using flow[18] and mobile contact line[19] and utilizing electrodynamics.[20–31] In most of these techniques to align microstructures, a templated mask or a pre-patterned substrate is required, for which, again, dependency on any of the conventional lithographic techniques is obvious.

An electric field bias perturbs polymer/air or polymer/polymer interfaces into micro-structures of a specific wavelength in an electric field induced patterning technique. The process involves a competition between the surface tension of the concerned polymeric thin film and the electrodynamic instability. With the ramping of voltage, perturbation grows with time, and at a dominant wavelength, the microstructures predominate. In all the bilayers, as mentioned earlier, the instability can be located in places where the distance between the electrodes is minimum. So, to obtain a faithful replication of microstructures in specific thin film areas, the bottom polymer layer or the top electrode should be patterned. In most of the reported articles, polymer-air bilayer,[30,32] polymer-polymer bilayer[33] and polymer-polymer-air trilayer[34] under electric field bias are widely investigated both theoretically and in

TH-2671_146153005

few cases, experimentally,[22,35] with the templated top electrode. Here, in our study, we use hard viscoelastic films (PDMS) and the nematic liquid crystal layer (5CB) to constitute the required confined bilayer system, and it is a template-less process.

The ECLL patterning dynamics have been discussed in chapter 4. This chapter focuses on a simple problem of the motion of a PDMS/LC/air contact line over an ECLL patterned PDMS substrate. In a confined arrangement, nematic LC molecules interact differently with the confined walls, i.e., the ITO surface and viscoelastic hard PDMS surface. The wetting characteristics change in applying electric field bias to the system. For, a viscoelastic hard PDMS substrate, during ECLL movement, the perturbed LC interface having a particular wavelength of instability deforms the PDMS thin film to form aligned patterned microwells filled with LC. From a fundamental point of view, the dynamical moving anisotropic LC front is an ideal testing ground for the various directional patterning techniques. Hence, we have tried to couple the ECLL phenomenon due to 5CB injection from the perpendicular direction to the ECLL-patterned microwells under air in the same system. We intended to interact with the system's dominant wavelength of instability to another irregular periodicity available within that system.

6.2. Experimental

6.2.1. Materials

Indium tin oxide coated glass plates (ITO, 10Ω /sq.) were obtained from Macwin India, India. Sylagrad 184, a commercial poly(dimethylsiloxane) (PDMS) precursor consists of a cross-linkable oligomer, and crosslinker was procured from Dow Corning, Mumbai, India (SYLGARD 184 kit). Analytical grade solvent n-hexane, acetone, isopropanol, and DMSO were procured from Merck, India. The nematic liquid-crystal 4-Cyano-4'-pentylbiphenyl was obtained from Sigma-Aldrich (99.99% pure, 5CB NLC). SU-8 2002 photoresist was purchased from Microchem, USA. The ITO coated glass plates were cut and cleaned by consecutive washing for 10 min each in boiling acetone and boiling isopropanol solvents. All the chemicals were used as received.

TH-2671_146153005

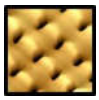

6.2.2. Methods

6.2.2.1. Construction of Liquid-Crystal Cell

A detailed description of the methods used to prepare and examine the liquid crystal-PDMS bilayer film within optical cells can be found in the previous chapter. Briefly, the experiments are carried out as follows: at the start t = 0, the sandwiched 5CB layer between two electrodes is kept at zero voltage. The cleaned planer ITO coated glass electrode served as the top electrode in each case, and spin-coated smooth viscoelastic PDMS thin film (~3 μm) resting on the ITO coated glass substrate acted as the bottom electrode. The two ITO coated top and bottom electrodes were kept apart by inserting a 35-μm polyimide film. The voltage was increased linearly with time at a ramping speed of ~2 V/s.

6.2.2.2. Fabrication of Micro grooved viscoelastic hard PDMS Surface

Permanent patterned master template of ~2.7 μm thickness and having 500 μm area of line pattern (spacing ~3 μm and width ~5 μm) was fabricated using negative photoresist SU-8 2002 (spin speed 2500 rpm, duration 60 s) on a glass substrate with the help of electron-beam lithography (JEOL USA). PDMS oligomer and crosslinker (2%) were mixed, and the mixture was diluted with n-hexane solvent in a 1:10 (v/v) ratio for spin coating. Cleaned 15×15 mm^2 ITO coated glass substrates were dried in N_2 stream and partially covered with magic tape to leave spaces for electrical connections and spacers. Spin-coating was done on these substrates at 2500 rpm for 120 s to get a ~3 μm soft PDMS film. The magic tapes were peeled off after spin coating. The thin films were prebaked for 10 min at 80 °C to remove the excess solvent. After that, the master template was embossed on the soft PDMS film, and a stack of 12 glass slides was put as the weight on the master template. The assembly was post baked at 120 °C for 12 h in a vacuum oven. After peeling off the master template, the micro-grooved structure's negative replica was fabricated on the PDMS surface. The flat bottom electrode on which the patterned PDMS film was resting was separated from the clean ITO coated glass (top) electrode by a spacer. Commercial polyimide tape of thickness ~35 μm was used as the spacer. An experimental set-up was arranged, and at 100 V, 5CB NLC was injected through the system, as schematically shown. For such a set-up, the generation of a high-intensity electric field of the order of a few MV/m through the electrodes led to rapid spreading of the 5CB droplet when injected normal to the line pattern on the PDMS surface.

TH-2671_146153005

6.2.2.3. Characterizations

After the experiment, the top electrode was taken away, and the surplus 5CB NLC on top of structured PDMS was soaked with a filter paper without disturbing the morphology. Then the PDMS film was directly kept in a UV-ozone chamber (Novascan PSD-UV - Benchtop UV-Ozone Cleaner) and exposed to UV-ozone for 20 min. A stiff oxide layer on the film was formed, attributed to the change in the chemical Nature of hydrophobic PDMS. It was washed with a polar aprotic solvent DMSO to get rid of the polar 5CB, which was still present on the PDMS surface. DMSO removes 5CB, with the least swelling of the PDMS. Morphological characterizations were accomplished employing the Atomic Force Microscope (Innova Iris, Bruker-Icon Analytical Equipment). Measurements regarding the diameters, wavelengths, and other morphological studies of the formed microwells were performed using Nanoscope Analysis software.

6.3. Results and Discussion

6.3.1. Role of 5CB liquid crystal on underlying PDMS

The surface morphology limits the anchoring properties of nematic liquid crystal. Without any external perturbation, the surface aligns the molecules in a direction known as easy direction. Therefore, it is predominantly in a planar orientation on the untreated ITO surface, whereas on viscoelastic hard PDMS, it is homeotropic.

There are two different zones of interest where various instabilities play their part. The regions are (a) The area far from the contact line, i.e., confined bilayer, and (b) The LC-PDMS-air contact line.

a) Since 5CB possesses high positive dielectric anisotropy, i.e., the dielectric constant along the director is ≈7.5 times larger than the dielectric constant along its perpendicular direction, dielectric alignment of molecules occurs above a critical voltage along the direction of the field. It is known as the Freedericksz transition, and the 5CB molecules are quasi-homeotropically oriented. When viewed through the cross polarizer, a color change is observed while passing the threshold voltage, and a transition from homeotropic to oblique alignment occurs. A transient Williams domain[36] arises, which becomes violent in the increasing field. The boundary of the loops consists of molecules that are yet to be realigned with the field direction. In the meantime, the viscoelastic hard PDMS thin film undergoes deformation from a flat state to a perturbed one due to electrical stress. Creasing instability develops initial indentation causing

TH-2671_146153005

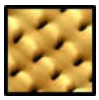

circular micro-cavities of larger diameter and longer wavelength on PDMS. This phenomenon results in an elevation in surface height around the dimples due to material displacement. Any area that is not near the dimples suffers a lower/no rise of surface height. Due to this variation of the thickness of PDMS film, when the voltage is further increased, miniaturized microwells are formed explicitly in the elevated PDMS zone experiencing higher electrical stress. On shooting up the voltage, the rest of the regions become packed with identical microwells in hcp design having smaller diameters and specific wavelengths.

b) In the LC-PDMS-air contact line, 5CB is planar on ITO and homeotropic on PDMS. Moreover, the wetting characteristics of 5CB are also different based on the hydrophobicity of PDMS and hydrophilicity of the ITO surface. There is also a large dielectric contrast between PDMS and 5CB. All these factors contribute to the rapid fingering instability at the three-phase contact line. The phenomenon termed as ECLL has been elaborated in chapter 4. Now, Due to ECLL, a large area of one-dimensionally line patterned arrays of microwells filled with 5CB is generated. Two wavelengths are reported- λ_c being the wavelength between two successive lines of patterned microwells and λ_f the wavelength of two adjacent microwells within a line. It is reported in our earlier publication that λ_c is mainly dependent on the thickness of the PDMS layer when other parameters are kept constant, and it was predicted that λ_f is dependent on the velocity of the contact line.

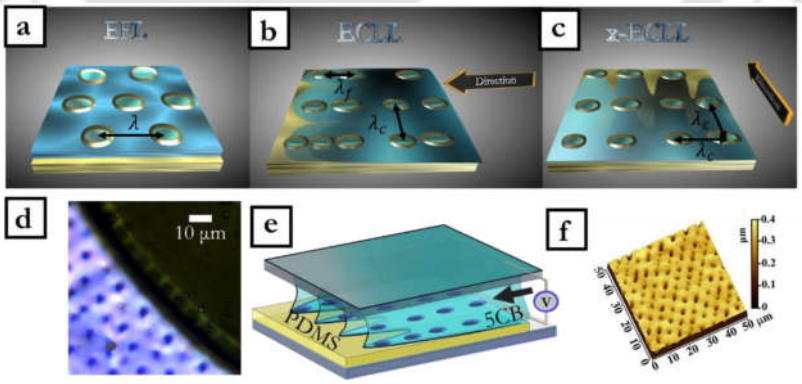

Figure 6.1 (a) Schematic diagram shows the EFL method and its characteristic wavelength. (b)-(c), Schematic diagrams depicting ECLL wavelengths (λ_c and λ_f) originated from it. (d) Polarized optical

TH-2671_146153005

micrograph of advancing LC contact line under which equispaced fingers generated. (e) Schematic diagram showing the ECLL process. (f) AFM micrograph showing the morphology of ECLL patterned area.

Because of the generation of microstructures on the PDMS surface, the orientation profile of the 5CB molecule around and inside those structures changes continuously with the ramping of voltage. When the voltage is kept constant at a higher value (300 V), almost all the 5CB molecules attain homogeneous oblique alignment. However, in the ECLL patterned area, due to the periodicity (λ_c) of the pattern, nicely ordered liquid crystalline electroconvections are originated along the patterned direction.

6.3.2. Fingering instability in nematic flow

Injection of air in a liquid crystal cell generates interfacial fingering patterns, and the phenomenon is studied extensively with various liquid crystal phases.[37][38] Spontaneous fingering instability of nematic film on the rigid surface is also reported.[39] This phenomenon is unexplored on soft surfaces. In our previous work[40], the generation of elongated 5CB fingers from the air/PDMS/5CB contact line on the influence of the electric field (Electrospitting) is discussed in detail (Figure 6.1d). In a parallel plate capacitor, under an electric field, viscous fingering at the interface of PDMS-LC occurs in the horizontal arrangement where gravity hardly plays any role. The viscous fingers grow and eject from the progressive contact line as satellite 5CB droplets. This is also called "electrospitting", which was validated by performing the following experiment. ITO-coated glass electrode having 500 μm area of line pattern on viscoelastic solid (~3.1 μm) PDMS thin film was made by imprinting lithographic technique having a separate area for electrical contact. The fabricated patterned electrode was used as the bottom electrode, and one clean ITO-coated glass electrode was used as the top electrode. Commercial polyimide tape of thickness ~35 μm was used as a spacer. The experimental set-up was arranged, and at 100 V, 5CB NLC was flowed through the system, as schematically shown in Figure 3d. For such a set-up, the generation of a high-intensity electric field of the order of a few MV/m through the electrodes led to the rapid spreading of the 5CB droplet when injected normal to the line pattern on the PDMS surface. The satellite 5CB droplets were arrested using artificially created periodic depression zones, and arrays of microwells are generated along the channel. The atomic force micrograph reveals that microwell morphology was formed across the depression zone of the pre-patterned PDMS film.

TH-2671_146153005

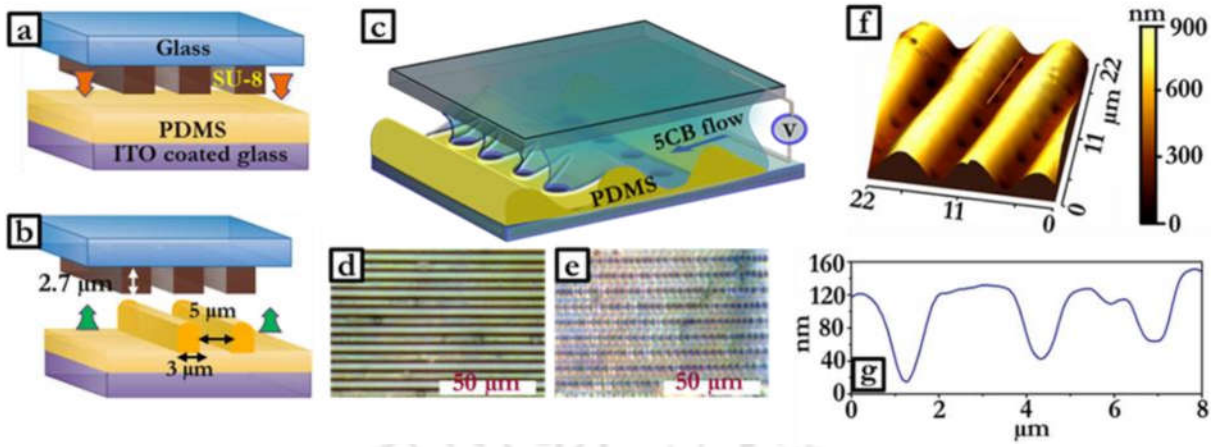

Figure 6.2 (a)-(b) Schematics of the performed experiment imprinting lithographic patterning of viscoelastic solid PDMS thin film (thickness ~3 μm). (c) Optical micrograph of the patterns generated due to embossing and curing the substrate with the attached template of Su-8 in the glass. Scale bar is 50 μm (d) Schematics of the experimental set-up. (e) Optical micrograph of the patterns generated after the flow of 5CB. (f) Atomic force micrograph showing the topography of the PDMS thin film after the experiment.

6.3.3. Mask-less cross patterning (x-ECLL) with a dominant wavelength

A dynamic flow of 5CB molecules in a confined geometry on the viscoelastic hard PDMS-5CB bilayer system under the electric field dissipates the local geometric phases of 5CB molecules. When 5CB/air/PDMS contact line moves unidirectionally on viscoelastic hard PDMS substrate under the electric field, it creates one-dimensionally patterned microwells. As discussed earlier, it generates two characteristic wavelengths λ_c and λ_f. We find that for a given thickness of PDMS film, λ_c is generally greater than λ_f. Now, during the ECLL process, displaced PDMS accumulates mostly around microwells. The effective upliftment of PDMS thin film around a microwell occurs in a direction and places where λ_f is involved ($\lambda_f < \lambda_c$) (Figure 6.1b). In this elevated zone, electrostatic pressure is relatively higher. After the ECLL process, the LC layer was displaced from the ECLL patterned zone though some amount of LC in those microwells was still left inside. Now, injection of an in-plane 5CB liquid crystal stream orthogonal to the

TH-2671_146153005

ECLL patterned direction results in forming cross-patterns of microwells. The dominant wavelength (λ_c) is preserved in all directions(Figure 6.1c).

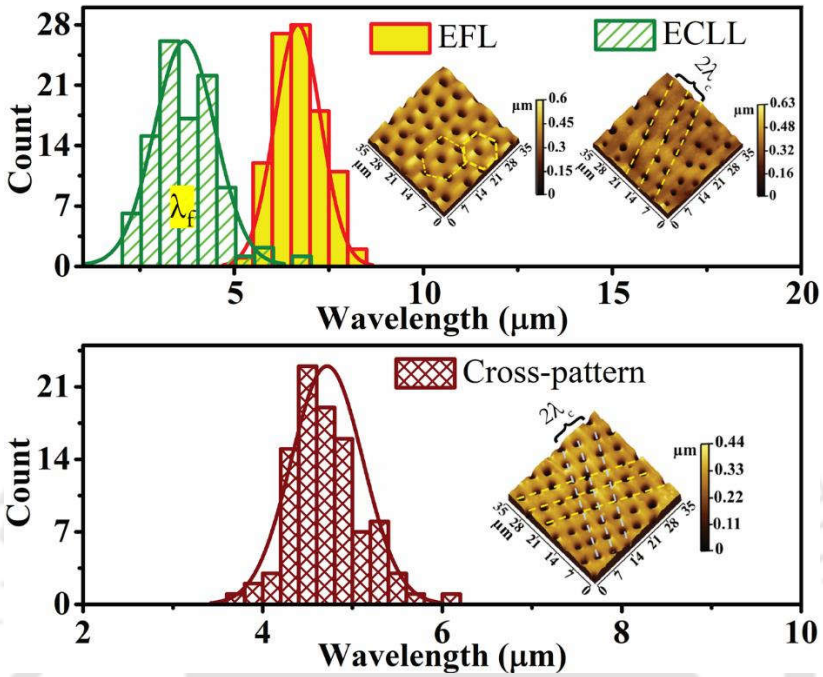

Figure 6.3 The characteristic wavelength distribution of (a) EFL, ECLL, and (b) x-ECLL.

Since $\lambda_f < \lambda_c$, the material accumulation around each microwell during ECLL process has a variation in material (PDMS) deposition profile. The places where λ_f (i.e., along the microwell array) is involved is elevated due to the shorter horizontal distance from next available microwell. Due to the shorter distance to the top electrode in those places, the electrostatic pressure is relatively higher. Figure 6.3 reflects from the wavelength distribution plot that the λ_c is guided by the pattern forming dominant wavelength of the system, and in the x-ECLL technique, the patterns with λ_c instability repeat itself from the perpendicular direction of the ECLL pattern. Here, the in-line wavelength λ_f is rearranged under the influence of fingering instability and the curvature effect of the incoming 5CB LC stream under the electric field in the air medium. The method is a pattern rectification technique. This mechanism continues with the flow and results in square patterned microwells (Figure 6.1c, 6.1f).

TH-2671_146153005

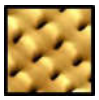

6.4. Conclusions

A three-phase moving contact line dynamics in an EWOD configuration with configuration is studied in this present chapter. The study has provided valuable insight into understanding the ECLL phenomena. We have demonstrated the phenomenon of electric field-induced directional cavitation on a one-dimensionally patterned viscoelastic PDMS layer by the directional cross-flow of liquid crystal 5CB. In this process, within a confined viscoelastic PDMS-5CB liquid crystal bilayer system, a square pattern of microwells was obtained without any mask/template. The patterning process is soft lithographic in Nature, and the mechanism is fast, reliable. The use of less expensive PDMS in place of any costly photoresist makes it economically friendly. Intricate patterning can be done without any mask in this method.

TH-2671_146153005

References

[1] M. Sun, C. Luo, L. Xu, H. Ji, Q. Ouyang, D. Yu, Y. Chen, *Langmuir* **2005**, DOI 10.1021/la050316q.

[2] M. Kolle, P. M. Salgard-Cunha, M. R. J. Scherer, F. Huang, P. Vukusic, S. Mahajan, J. J. Baumberg, U. Steiner, *Nat. Nanotechnol.* **2010**, DOI 10.1038/nnano.2010.101.

[3] A. Majumder, A. Ghatak, A. Sharma, *Science (80-.).* **2007**, DOI 10.1126/science.1145839.

[4] L. Xue, Y. Han, *Prog. Polym. Sci.* **2011**, *36*, 269.

[5] M. Nedelcu, M. D. Morariu, S. Harkema, N. E. Voicu, U. Steiner, *Soft Matter* **2005**, *1*, 62.

[6] S. Roy, D. Biswas, N. Salunke, A. Das, P. Vutukuri, R. Singh, R. Mukherjee, *Macromolecules* **2013**, *46*, 935.

[7] A. M. Telford, S. C. Thickett, C. Neto, *J. Colloid Interface Sci.* **2017**, *507*, 453.

[8] A. M. Telford, L. Meagher, V. Glattauer, T. R. Gengenbach, C. D. Easton, C. Neto, *Biomacromolecules* **2012**, *13*, 2989.

[9] S. C. Thickett, J. Moses, J. R. Gamble, C. Neto, *Soft Matter* **2012**, *8*, 9996.

[10] D. C. Hyun, M. Park, U. Jeong, *J. Mater. Chem. C* **2016**, *4*, 10411.

[11] A. Ghatak, M. K. Chaudhury, *Langmuir* **2003**, *19*, 2621.

[12] S. Harkema, E. Schäffer, M. D. Morariu, U. Steiner, *Langmuir* **2003**, *19*, 9714.

[13] M. Banik, R. Mukherjee, *ACS Omega* **2018**, *3*, 13422.

[14] K. Y. Suh, Y. S. Kim, H. H. Lee, *Adv. Mater.* **2001**, *13*, 1386.

[15] K.-Y. Suh, M. C. Park, P. Kim, *Adv. Funct. Mater.* **2009**, *19*, 2699.

[16] K. Y. Suh, H. H. Lee, *Adv. Funct. Mater.* **2002**, *12*, 405.

[17] J. P. Singer, *J. Polym. Sci. Part B Polym. Phys.* **2017**, *55*, 1649.

[18] M. Park, Y. Xia, U. Jeong, *Angew. Chemie Int. Ed.* **2011**, *50*, 10977.

TH-2671_146153005

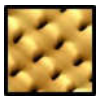

[19] U. Thiele, *Adv. Colloid Interface Sci.* **2014**, *206*, 399.

[20] E. Schäffer, T. Thurn-Albrecht, T. P. Russell, U. Steiner, *Europhys. Lett.* **2001**, DOI 10.1209/epl/i2001-00183-2.

[21] P. G. Oppenheimer, *Electrohydrodynamic Patterning of Functional Materials*, **2013**.

[22] M. D. Morariu, N. E. Voicu, E. Schaffer, Z. Q. Lin, T. P. Russell, U. Steiner, *Nat. Mater.* **2003**, *2*, 48.

[23] P. S. G. Pattader, I. Banerjee, A. Sharma, D. Bandyopadhyay, *Adv. Funct. Mater.* **2011**, *21*, 324.

[24] G. Amarandei, P. Beltrame, I. Clancy, C. O'Dwyer, A. Arshak, U. Steiner, D. Corcoran, U. Thiele, *Soft Matter* **2012**, *8*, 6333.

[25] L. Wu, S. Y. Chou, *J. Nonnewton. Fluid Mech.* **2005**, *125*, 91.

[26] M. D. Morariu, N. E. Voicu, E. Schäffer, Z. Lin, T. P. Russell, U. Steiner, *Nat. Mater.* **2003**, *2*, 48.

[27] N. E. Voicu, S. Ludwigs, U. Steiner, *Adv. Mater.* **2008**, *20*, 3022.

[28] R. Verma, A. Sharma, K. Kargupta, J. Bhaumik, *Langmuir* **2005**, *21*, 3710.

[29] J. Heier, J. Groenewold, U. Steiner, *Soft Matter* **2009**, DOI 10.1039/b906863e.

[30] E. Schaffer, T. Thurn-Albrecht, T. P. Russell, U. Steiner, *Nature* **2000**, *403*, 874.

[31] G. Amarandei, P. Beltrame, I. Clancy, C. O'Dwyer, A. Arshak, U. Steiner, D. Corcoran, U. Thiele, *Soft Matter* **2012**, DOI 10.1039/c2sm25273b.

[32] P. Goldberg-Oppenheimer, U. Steiner, *Small* **2010**, DOI 10.1002/smll.201000060.

[33] R. V. Craster, O. K. Matar, *Phys. Fluids* **2005**, *17*, 0.

[34] P. D. S. Reddy, D. Bandyopadhyay, A. Sharma, *J. Phys. Chem. C* **2012**, *116*, 22847.

[35] N. Arun, A. Sharma, P. S. G. Pattader, I. Banerjee, H. M. Dixit, K. S. Narayan, *Phys. Rev. Lett.* **2009**, DOI 10.1103/PhysRevLett.102.254502.

TH-2671_146153005

[36] R. Williams, *J. Chem. Phys.* **1963**, *39*, 384.

[37] A. Buka, J. Kertész, T. Vicsek, *Nature* **1986**, *323*, 424.

[38] A. Buka, P. Palffy-Muhoray, Z. Racz, *Phys. Rev. A* **1987**, *36*, 3984.

[39] M. Ben Amar, L. J. Cummings, *Phys. Fluids* **2001**, *13*, 1160.

[40] P. Roy, R. Mukherjee, D. Bandyopadhyay, P. S. Gooh Pattader, *Nanoscale* **2019**, DOI 10.1039/c9nr05729c.

TH-2671_146153005

Chapter 7

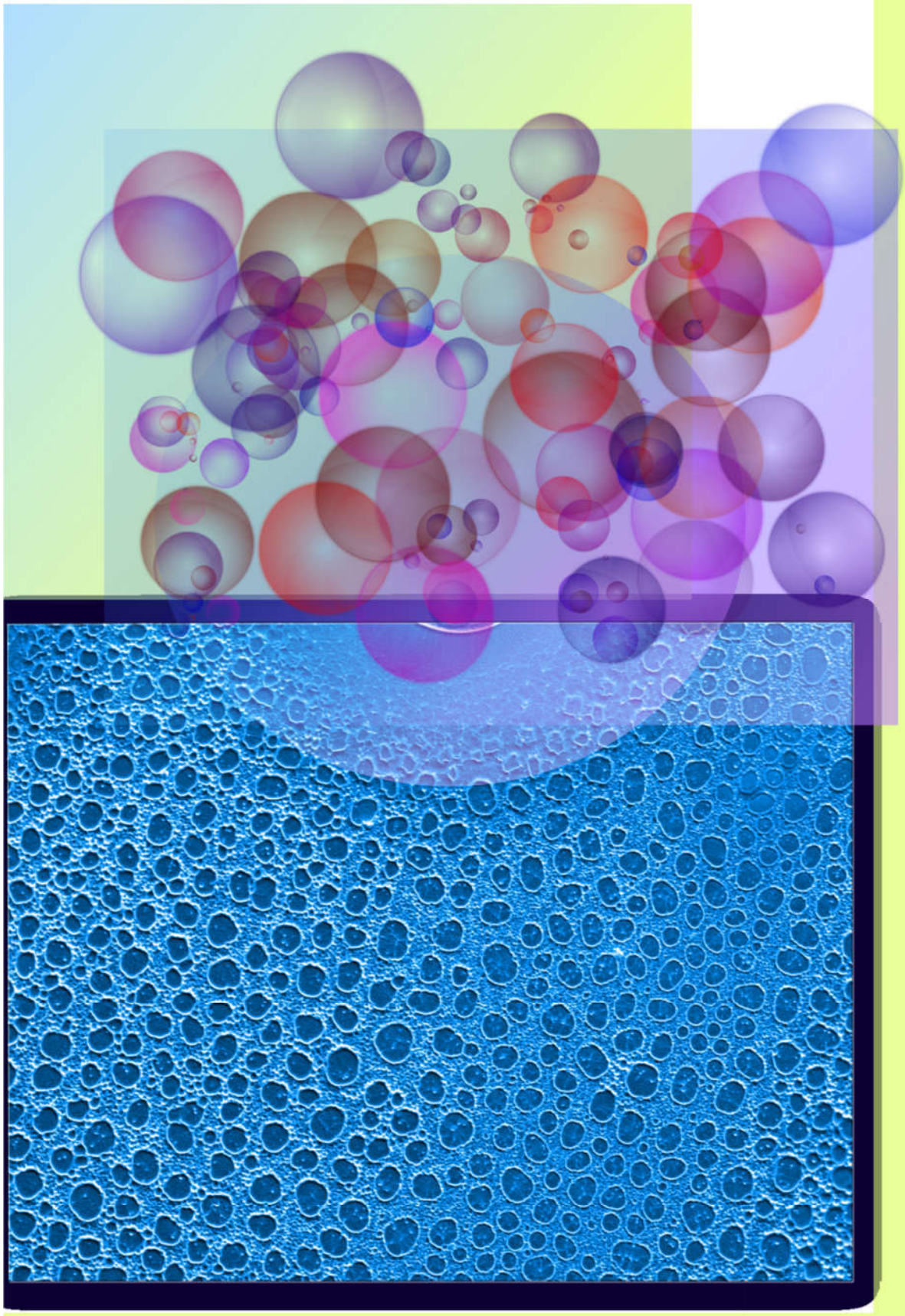

TH-2671_146153005

Chapter 7

MULTISCALE PATTERNING OF THE SOFT INTERFACE: A DYNAMIC BREATH FIGURE TEMPLATE FOR ELECTROHYDRODYNAMIC LITHOGRAPHY

Abstract

This chapter experimentally demonstrates a simple pathway to fabricate multiscale patterns on a soft surface. For this purpose, a dynamic breath figure (d-BF) mask and electric field induced lithography (EFL) were employed. First, hygroscopic glycerine microdroplets that dictated the largest length scale were placed on soft elastomer by imprint lithographic technique. Then d-BF of condensed water vapor serves as a tunable soft template for secondary lengthscale. Finally, EFL imparted finer features to the system. UV-Ozone treatment of the surface masked with glycerine microdroplets and d-BF selectively changed the surface property and hardness of the PDMS elastomer; thus, EFL induced the finer structures selectively. A confined bilayer set-up, consisting of 5CB Liquid crystal and the selectively modified PDMS, underwent EFL in a parallel plate capacitor arrangement between two Indium Tin Oxide (ITO) electrodes revealed the multiscale patterns on the PDMS. The wavelength of the finest structure due to EFL depends on the local thickness of PDMS and the applied electric field when all the other parameters are kept constant. The secondary length scale can be controlled by the parameters influencing the d-BF, and the largest length scale is dictated by the imprinting length scale of the mask used.

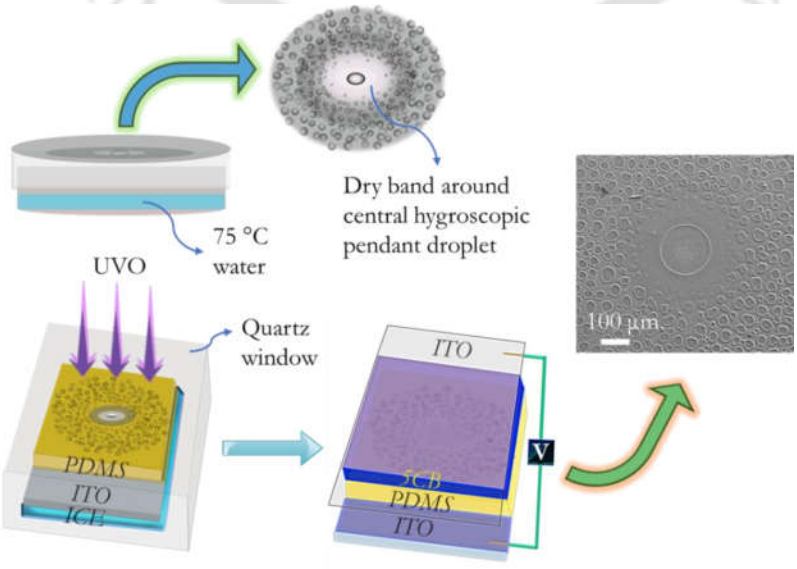

TH-2671_146153005

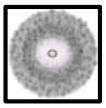

7.1. Introduction

From the beautiful wings of the butterfly and the fascinating peacock's plumage to the regularities in fish scales and the hexagons of the honeycomb, patterns exist in nature for their intended uses. A butterfly's wings consist of micro- and nanoscale features where microstructures protect it from environmental, mechanical abrasion while the nanostructures present in it incorporate superb optical properties.[1] Moreover, if we take the example of fractal tree branches, its repetitive growth follows miniaturization in scale. It is self-similar as well as hierarchical in nature.[2]

Various attempts were made to replicate the naturally occurring patterns, especially multi-length scale, hierarchical features which have enormous potential in diverse applications such as self-cleaning, chromogenic and optical devices, etc. In this regard, for creating micron and submicron scale pattern morphology, the electric field is used on deformable soft polymer surfaces, and the process is termed electric field lithography (EFL).[3,4] The benefits of using EFL lies in the fact that no demolding step is required like capillary force lithography (CFL)[5–7], where distortion may occur to the required morphology, and like photolithography, no high-end instrumentation or no tedious, repetitive chemical routes are needed to be followed. The electric field induces instability in both cases where an in-plane electric field applies to the polymer thin film[8] and where the film experiences an electric field perpendicular to the surface in between two parallel electrodes.[9,10],[11] Mostly, the instability of polymeric thin film under the influence of the electric field is studied in a capacitor arrangement. A critical applied voltage begins to alter the morphology. The mechanism involves charge accumulation at the interface to destabilize it by overcoming interfacial tension, restoring elastic force, etc. All the experiments reveal that the initial thickness of polymer film, electrode spacing, effective applied voltage, and interfacial tension at the interface is the main governing parameters. The thoroughly studied systems in the capacitor arrangement are polymer-air,[11,12] polymer-polymer[13],[14],[15] bilayers, liquid bilayer[16], liquid tri-layer[17], polymer-polymer-air[18],[19], and polymer-air-polymer[20],[21] trilayers. All these studies point out that the ratios of dielectric constants, thicknesses, viscosities of confined layers are important in predicting microstructures at the interface. A detailed study explores that the viscosity of the polymer in the polymer-air system can influence the dynamics of the pattern formation process.[22] Also, it is experimentally demonstrated that pattern

TH-2671_146153005

morphology (microwell or micropillar) can be controlled by the rheology of the polymer film coupled with its thicknes, if the bilayer system with highly contrasting dielectric permittivity is chosen.[23]

In this work, we have chosen the bottom polymer layer as viscoelastic hard PDMS and the top layer as 5CB liquid crystal sandwiched between two ITO coated electrodes to have the microwells in the EFL experiment.[23] The breath figure template is configured by the dropwise condensation of water vapor on a cold surface. The phenomena find its applications in fabricating porous films,[24–29] decorating nanoparticles,[30] diffraction gratings,[31] gas sensors.[32] Different types of chemically hygroscopic droplets were used in breath figure experiments to explain the formation and kinetics, including the dry band around it.[33–35] We first report that this hierarchically configured pattern of water droplets can be judicially used as a mask in the EFL experiment for a soft substrate.

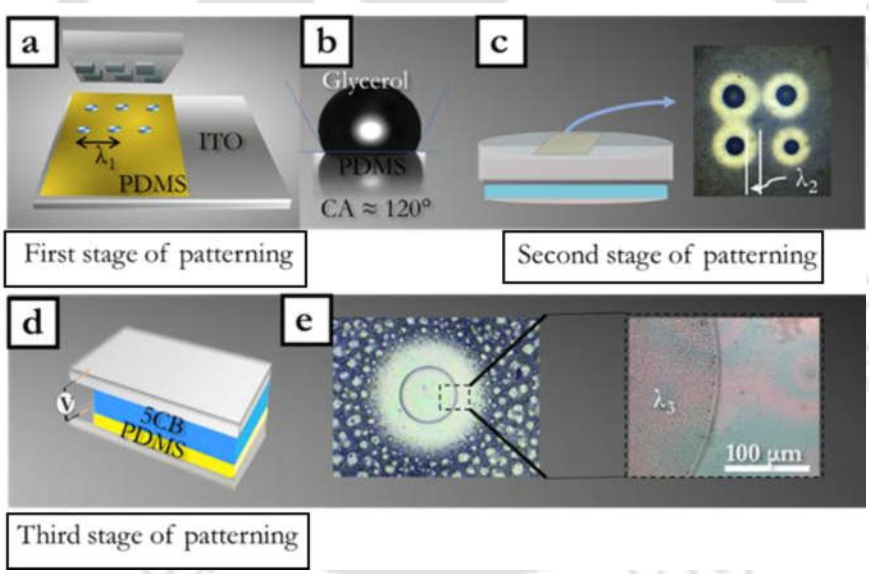

Figure 7.1 (a) Schematic diagram of the first stage of patterning by micro-contact printing of glycerol droplets on viscoelastic hard PDMS thin film (thickness ~3 µm). Patterning wavelength ($\lambda_1 = 288 \pm 15$ µm) is generated due to the patterned mask (b) Image of glycerol sessile droplet on PDMS showing contact angle ≈ 120°. (c) A schematic diagram shows the second stage of patterning. In the reflective mode, the optical micrograph shows the generation of tunable second patterning wavelength (λ_2~ 50 µm, depends on the time of exposure to the vapor when other parameters are kept constants) due to the formed dry band in breath figure. (d) Schematic diagram of the EFL experiment. (e) Optical micrograph of the breath

TH-2671_146153005

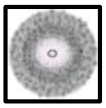

patterned area after EFL. The magnified view of it shows predominantly uniform microwells having EFL wavelength (λ_3 = 4.13 ± 0.5 μm).

7.2. Materials and methods

7.2.1. Materials

Glycerol was purchased from Merck, India. Indium tin oxide coated glass plates (ITO, 10Ω /sq.) were obtained from Macwin India, India. Sylgard 184, a standard poly(dimethylsiloxane) (PDMS) precursor having cross-linkable oligomer and crosslinker, was procured from Dow Corning, Mumbai, India (SYLGARD 184 kit). Analytical grade solvent n-hexane was procured from Sisco Research Laboratories Pvt. Ltd., India. 4-Cyano-4'-pentylbiphenyl nematic liquid crystal was obtained from Sigma-Aldrich (99.99% pure, 5CB NLC, Tp ~ 34.5 ± 0.5 °C). All of these chemicals were used without any further purification. deionized water (DI, Merck Millipore, grade-I) was used for all the experiments

7.2.2. PDMS substrate preparation

We prepared thin PDMS films from Sylagrad 184 by spin coating. The oligomer to crosslinker volume ratio was maintained at 50:1. To prepare the aliquot for spin coating, the PDMS precursor mixture was diluted in the solvent n-hexane in a 1:10 volume ratio to obtain ~ 3 μm spin-cast (2500 rpm, 120 s) PDMS film. Before spin coating, the bare ITO surface was selectively masked with magic tape (Scotch Magic Tape-810 series, 3M India Ltd), leaving spaces for attaching electrical connections and spacers. When the spin coatings were over, the tape was removed without any leftover adhesive. After spin-coating, samples were baked under vacuum to obtain viscoelastic hard samples (120 °C for 12 h). Thickness measurements were done in Stylus Profiler (Dektak Veeco).

7.2.3. PDMS stamp preparation

A topographically patterned PDMS stamp was prepared via replica molding. As a positive replica (master), the flexible inner wrapping aluminium foil (8011 grade) used on hard chocolate was chosen. The

TH-2671_146153005

golden/silver aluminium foil had protruded gridlines creating decorative square patterns on both sides. A suitable portion of the foil was cut and pasted on a clean glass surface, and a trench was built around it using double-sided foam tape. PDMS solution was prepared by mixing 10% crosslinker with the prepolymer. After the degassing step, the empty trench was filled with the prepared mixture of crosslinker and prepolymer PDMS. The embossed trench was cured in a vacuum oven at 120 °C for 12 h for complete cross-linking and pattern replication. After this, the PDMS cake was released from the master to get the desired structures on the PDMS.

7.2.4. Micro-contact printing (μCP) of glycerin droplets on soft PDMS substrate

The clean surface of a glass slide was made properly hydrophilic by UVO treatment. The degree of hydrophilicity was checked by placing a glycerin droplet on top of the treated surface. Now, with the edge of another clean glass slide, the glycerin was homogeneously spread over the surface to obtain a uniform wet glycerin film. Now, the PDMS stamp was gently touched to the glycerin coating and was separated. The micro glycerin drops adhered to the patterned stamp was transferred onto the viscoelastic hard PDMS by bringing the stamp in close proximity to the film. When the stamp was uplifted, the desired transfer of glycerin droplets occurred, and multiple square patterns of micro drops of glycerin on viscoelastic hard PDMS thin film substrate were obtained. The different stages of this patterning process are schematically shown in Figure 7.3a-7.3f.

7.2.5. EFL experiment

Before the experimental arrangement for the EFL experiment, the following steps were performed. Firstly, the PDMS film was spin-cast on a clean piece of ITO and vacuum cured, as discussed before. Then, on the surface of the PDMS films, glycerol micro drops were patterned, and UVO exposure was performed for 30 min. After that, the PDMS film was washed with a copious amount of water to get rid of any glycerol residue. Next, it was dried with the dry nitrogen flow. Thereafter, commercial polyimide (~ 35 μm) tape, as spacers were attached, and a layer of 5CB was introduced on the UVO treated PDMS substrate, and another clean ITO substrate was placed from the top to confine the 5CB loaded PDMS surface. Finally, the ITO electrodes were connected with a direct current (DC) power source (SES Instruments Pvt. Ltd.,

TH-2671_146153005

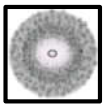

EHT-II), and the voltage was elevated at a ramping speed of ~2V/s. The experiments were imaged and video recorded by placing the LC cell on the microscope stage.

7.2.6. Dynamic breath figure (d-BF) experiment

A glycerol droplet (1 µl) was pipetted out on the inner surface of a PS-made petridish lid. Now the lid carrying the droplet was carefully covered on the dish containing 5 ml of 75 °C warm water. So, the hygroscopic pendant droplet of glycerol was exposed to its solvent water vapor in a semi-closed system. A breath figure with a thick dry band around the central glycerol droplet formed. Next, a quartz window was prepared by selectively removing a portion from the PS-lid and by attaching a quartz plate in that vacant position. After that modification, it was also checked whether the lid was still impervious to water and gases. Now, for the PDMS substrate on ITO, the same process of breath figure formation was repeated for patterned glycerol droplets. Breath figures and dry bands were formed for individual droplets. When the equilibrium was reached, the PDMS substrate was transferred and placed inside the closed petridish having a quartz window lid. In that situation, the temperature of the system was lowered down by placing an icepack below the system, and UVO treatment was done for 30 min. Finally, the EFL experiment was done with the PDMS substrate as the bottom electrode, as described earlier.

7.2.7. Characterizations

To look into the morphology of the PDMS thin film after the experiment, specifically, the 5CB liquid crystal layer was removed without hampering the morphology of the thin PDMS film. Excess 5CB NLC was soaked from the bottom electrode with a filter paper carefully. Then UVO treatment was done on the PDMS film for 20 min, which contributes to a stiff oxide layer on the top of the film. The UVO treated substrate was washed with DMSO, a polar aprotic solvent, that removed 5CB NLC preferentially, hardly swelling the PDMS. It also furnished a skinny layer for protecting the silanol groups in the PDMS surface. This was advantageous to prepare a better surface in the case of PDMS for doing morphology characterization in Atomic Force Microscope (AFM; Innova Iris, Bruker-Icon Analytical Equipment). The substrate was dried in dry nitrogen flow, and atomic force microscopy was done on the selected patterns in tapping mode.

TH-2671_146153005

7.3. Results and discussion

7.3.1. Glycerol droplet templated evolution of pattern morphology on viscoelastic hard film

Nearly hemispherical glycerine drops in the square arrangement were imprinted on viscoelastic PDMS film using a square PDMS stamp. Figure 7.2a shows the digital photograph of the aluminium foil used in fabrication of the square PDMS stamp. FESEM micrograph reveals that the aluminium foil contains square arrangement having periodicity of ~ 300 μm with the dimension of ~ 175 × 175 μm at the bottom of the box pattern. After casting, and demolding the cured PDMS stamp had the raised square box template. This was used as flexible stamp for subsequent imprinting.

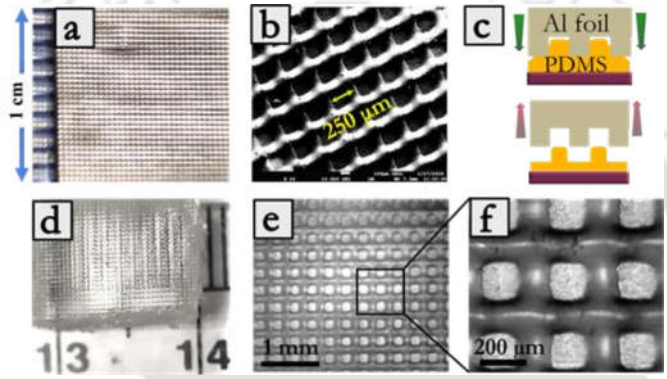

Figure 7.2 (a) Digital photograph of the master (Aluminium foil) and (b) FESEM imaging reveals the dimension and morphology of the open box pattern. (c) Schematic diagram of the process capillary force lithography to prepare the PDMS negative replica (stamp) of the master aluminium foil. (d) Digital photograph of the hard-baked PDMS stamp after releasing from the master. (e) The optical micrograph in the reflective mode showing the morphology of the stamp and (f) the magnified view of it showing predominantly uniform negative pattern replication.

The optical images of the surface structures on the PDMS stamp are depicted in Figure 7.2e-7.2f. The μCP of glycerol with the prepared PDMS stamp was performed on the viscoelastic hard thin film of thickness ~3 μm. The μCP process is depicted in Figure 7.3. The hydrophobic PDMS allowed the hydrophilic glycerol to adhere to the tip of each box of the stamp as droplets (contact angle ≈ 120°, Figure 7.1b). For the time window of the experiment, there was no diffusion of glycerol in bulk PDMS, or swelling of the PDMS stamp was observed. For μCP, the PDMS stamp, having the glycerol drops, was placed on the

TH-2671_146153005

viscoelastic PDMS substrate, and then the PDMS stamp was quickly uplifted. The special precaution was taken while contacting and uplifting the stamp. No extra pressure was applied in transferring the mass of glycerol to the substrate; otherwise, the ordered glycerol drops got disrupted. Figure 7.3g unveils the ordered deposition of glycerol droplets over a large surface area. A magnified micrograph (Figure 7.6a) depicts an almost uniform distribution with marginal variation in the volume of glycerol droplets. The glycerol droplets were used as a shield to protect the underneath viscoelastic PDMS layer from UVO exposure.

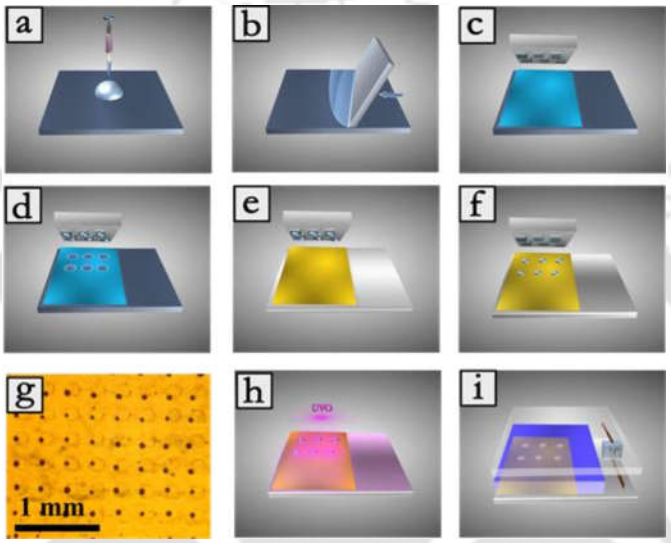

Figure 7.3 (a)-(f) Schematic representation of the μCP of arrays of glycerol droplets on viscoelastic hard PDMS substrate. (g) The optical micrograph in the reflective mode shows the large are patterned PDMS surface. Schematic representations of (h) the UVO treatment of glycerol droplet masked PDMS surface and (i) the electric field induced lithography with 5CB LC as the top layer on washed (with DI water) and dried UVO treated PDMS substrate as the bottom layer.

When the masked substrate is exposed to UV light, chemical changes occur on the PDMS surface. The UV lamp inside the UVO cleaner irradiates two wavelengths (185 and 254 nm). The 185-nm UV light generates ozone from atmospheric oxygen. First, it dissociates molecular oxygen (O_2) into triplet atomic oxygen $O(^3P)$, which later combines with molecular oxygen to generates ozone (O_3). On the other hand, 254-nm UV light dissociates O_3 and forms O_2 and singlet atomic oxygen $O(^1D)$. Singlet atomic oxygen $O(^1D)$,

TH-2671_146153005

having strong oxidation power, reacts with PDMS surfaces and transforms it into inorganic stiff silicon oxide. Now, pure glycerol can hinder molecular oxygen permeability[36], and it is non-transparent to UV. The most intense UV absorption wavelength for glycerol is at 198 nm.[37]

7.3.2. Condensation of water vapor on a single glycerol droplet

A rapid evaporative solvent is required to form the breath figure on a cold surface. In this context, moisture-laden air is generally used to get a gradient of pure water droplets condensed around the central hygroscopic droplet. To accelerate the process, we use 75 °C warm water as the source of vapor and to maintain temperature gradient and humid conditions. The distance between the hot water surface to the glycerol droplet is ~0.5 cm. To explain the difference between regular breath figure structures and the one formed around a hygroscopic droplet, we consider the hygroscopicity of the central drop.

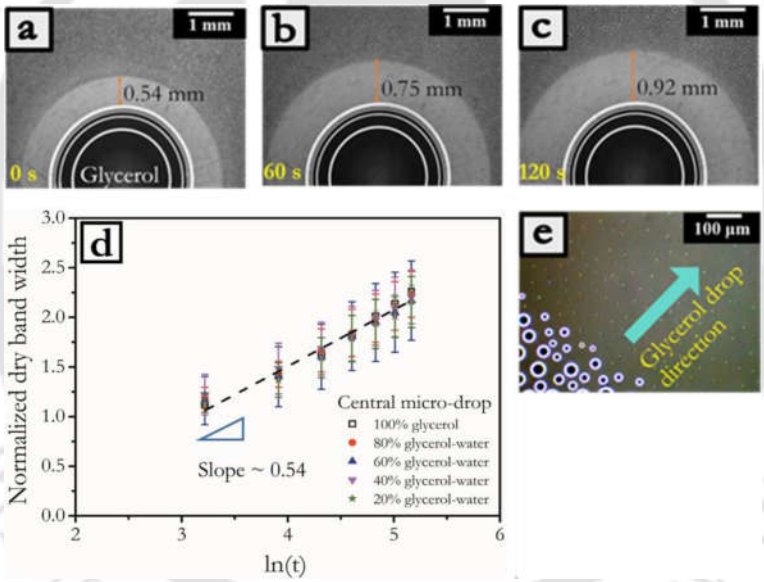

Figure 7.4 Optical micrographs in the reflective mode breath figure process around the central pendant glycerol droplet on PS petridish surface in different time frames (a) 0 s, (b) 60 s, and (c) 120 s. The sequences also show the increment of dry band width with time. Variation of normalized dry band width against the time of 1 µL central glycerol droplet of different concentrations is shown in figure (d). Figure (e) shows the optical micrograph of the size distribution of evaporative water droplets in the immediate vicinity of the dry band.

TH-2671_146153005

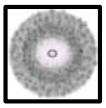

It is well-documented that the hygroscopic drop has a 'zone of influence' of absorbing water molecules in it. The spreading coefficient, S_c, is defined as:[38]

$$S_c = \gamma_{sg} - \gamma_{lg} - \gamma_{ls}$$

Where γ_{sg} is the component of surface tension of the pure polymer surface, γ_{lg} is the surface tension component of the pure liquid drop, and γ_{ls} is the liquid drop-polymer interfacial tension. $S > 0$ implies complete wetting and $S < 0$ means partial wetting. For the pendant glycerol droplet, when it gets hydrated and expands its contact line. Those water droplets which are condensed in immediate vicinity to dry band evaporates quickly, and due to mass loss, volume contraction occurs. So, due to this physical phenomenon, a long-range hierarchical mask composed of condensed water droplets is produced. In the case of PS or PDMS substrate, during the breath figure experiment, γ_{sg} does not change. γ_{lg} also remains constant for liquid droplets. So, the spreading is mainly dependent on γ_{ls}. γ_{ls} is also termed as the free energy required for creating a solid-liquid interface.[39] The contact line dynamics and other physical phenomena in the breath figure experiment that dependent on the γ_{ls} component are described in Appendix A.2. Further, during the UVO treatment, the spreading coefficient increases as the polymer PDMS at the contact line of both glycerol and water droplet slowly transforms towards hydrophilic. The base radius changes by these processes. The optical images in Figure 7.6a-7.6c support this phenomenon.

Kinetics of the growth of dry band around different concentrations of glycerol drop is studied. The increment of the droplet radius and the dry band follows a power law in time ($d \sim t^{0.5}$).[34,40](Figure 7.4d)

7.3.3. Electric field induced lithography using the d-BF mask

The dynamic breath figure patterning of a glycerol droplet that we have developed in this article can be applied both to the case of a single glycerol droplet as well as to a pattern of glycerol drops. We construct a bilayer system composed of d-BF patterned PDMS as the bottom layer on the ITO electrode, and a 5CB nematic liquid crystal layer on top of it serves as the top layer. We have discussed and analyzed the evolution of morphology and other details of flat PDMS thin film and 5CB bilayer systems under the electric field elsewhere.[4,41] It is worth mention here that polydimethylsiloxane (PDMS) is isotropic in nature and has a

TH-2671_146153005

very low positive dielectric constant (2.65)[42] compared to 5CB having anisotropic dielectric constants $\varepsilon_{\parallel}$ = 15.70 and $\varepsilon_{\perp}$ = 7.50.[43] In general, 5CB is a naturally twisted nematic liquid crystal, which, on the application of voltage, untwist itself in varying degrees depending on the magnitude of the applied voltage.

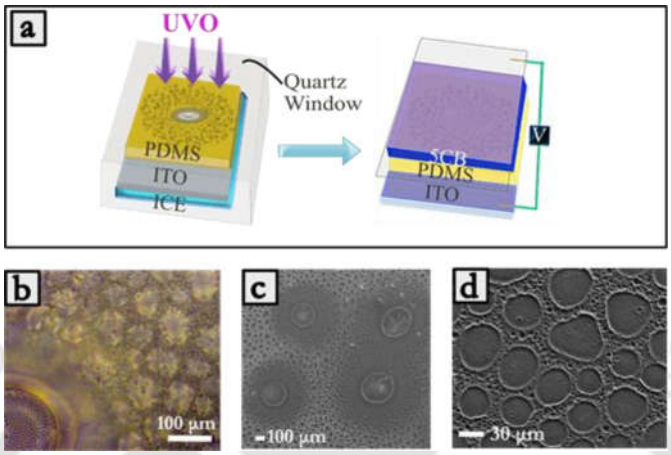

Figure 7.5 (a) Schematic representation of the UVO treatment of breath figure pattern on viscoelastic hard PDMS substrate and EFL experiment using the UVO treated PDMS on ITO as a bottom electrode (b) Optical polarized micrograph during EEL experiment. (c) FESEM image of patterned PDMS substrate after removing the 5CB top layer. (d) FESEM image of PDMS substrate with breath figure experiment and UVO treatment.

The PDMS thin film (~3 µm) used primarily in this study is viscoelastic hard in nature. The electric field response to this bilayer interface can be categorized based on the appearance of liquid crystals in different morphological zones. Firstly, the LC layer undergoes the Fréedericksz transition supported by the homeotropic anchoring at the PDMS interface. The LC molecules try to maintain their vertical alignment (as the electric field is applied in the vertical z-direction) in the interface and bulk as well. Only near the top flat ITO electrode, the LC layer exhibits a large director gradient. Secondly, due to electric pressure induced by the applied electric field, the PDMS-LC interface deforms to minimize the system's overall energy. This is in accordance with the electrohydrodynamic instability (EHD) reported for different bilayer systems. In our PDMS-5CB bilayer settings, upon application of the electric field, the fastest-growing dominant wavelength, λmax, determines the length scale of the instability and governs the formed pattern periodicity.

TH-2671_146153005

The theoretical derivation of the characteristic wavelength of instability in EHD, for isotropic Newtonian bilayer, is well established. Taking reference from it and considering our system in similar settings can formulate the dominant wavelength applicable to our confined bilayer system as:

$$\lambda_{max} = \frac{2\pi\sqrt{2\gamma\{\varepsilon_2 d + h(\varepsilon_1 - \varepsilon_2)\}^3}}{\sqrt{V^2\varepsilon_0\varepsilon_1\varepsilon_2(\varepsilon_1 - \varepsilon_2)^2}}$$

Where V is the applied bias voltage, ε_0 is the dielectric permittivity of the vacuum (8.854×10^{-12} F/m), and $\varepsilon_1, \varepsilon_2$ are the dielectric constants of 5CB and PDMS, respectively. γ is the interfacial tension at the PDMS-5CB interface. Apart from all these parameters, substrate rheology also plays an important role in the electric field induced evolution of morphology. In our previous study, we have seen micropillars or microwells are formed based on whether the PDMS substrate is viscoelastic soft or hard. In this analysis, we see the central glycerol drop and the breath figure around it serve as a soft template.

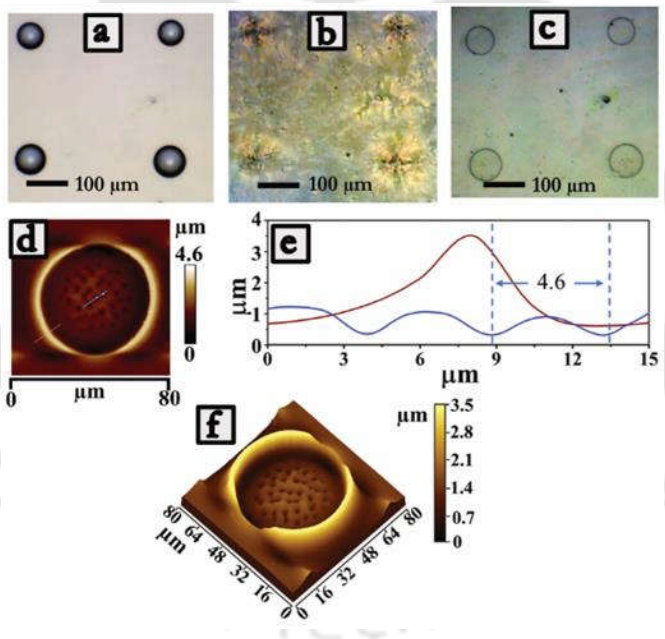

Figure 7.6 (a) Optical micrograph in the reflective mode of the square patterned glycerol droplets on the ~3 µm PDMS thin film (b) Optical polarized micrograph of the same area during EFL experiment. The footprints of glycerol droplets on PDMS under the 5CB layer in the presence of 300 V DC shows the formation of distinct microwells. After the EFL experiment, (c) Optical micrograph in the reflective mode shows the glycerol spots after removing the 5CB layer and washing with DMSO. (d) 2D AFM image of the

TH-2671_146153005

microwell-patterned single glycerol droplet footprint by EFL is shown. In figure (e), the line scans of the AFM image depict the surface profile and wavelength of the morphology for the ~3 μm PDMS thin film. (f) The 3D view of it shows the actual topography of the footprint after EFL patterning.

Pure water is UV transparent[44], and in water, appreciable oxygen solubility is reported.[45,46] In atmospheric pressure, the availability of molecular oxygen outside the water droplet is equivalent to the air's oxygen concentration. Due to the hemispherical shape of the water droplet on PDMS, the probability of interaction of UV with soluble oxygen happens maximum along the center of the drop. From the center to the perimeter, the effectiveness of UVO treatment reduces gradually. The perimeter of the drop is the interface with water and air and along it, the influence of UVO treatment is maximum in air side and minimum on the water side. As the breath figure condenses, the central glycerol drop tends to get saturated absorbing water molecules from the nearby evaporating droplets. In this process the increased water content facilitates the UVO treatment of that glycerol masked spots. Figure 7.5c is the FESEM micrograph showing the final PDMS substrate morphologies after breath figure patterning, and figure 7.5d is the FESEM micrograph confirming the structure formation outside the glycerol drop imprint due to solely breath figure experiment and UVO treatment. We freeze the system before UVO treatment to minimize the rate of water evaporation. The porous structures between the water droplet imprint and on the rest of the film are due to the frost condensation during the application of ice to freeze the evaporation of condensed water droplets.

7.4. Conclusions

We presented a novel and straightforward strategy for producing hierarchically ordered multiscale polymeric films. The presence of central hygroscopic drop assisted the hierarchical ordering of aqueous droplets on the surface of a polymer viscoelastic hard film. UVO treatment of the film using the hierarchically arranged water droplets as a mask produces comparatively soft and hard spots on the same surface. Electric field induced lithographic technique produces microwells on the soft spots. The breath figure assisted morphological structures itself, and the hexagonally packing of microwells constitutes

TH-2671_146153005

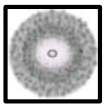

independent multiscale orderings in the masked parts of the polymer film. Application of temperature gradient and good hydrophobicity of the defect-free clean polymer surface was crucial in terms of obtaining a highly ordered breath figure. A wide spectrum of hygroscopic materials is anticipated to be useful in this approach to fabricate diverse hierarchical and multiscale structures without utilizing any intricate chemistry and high-end instrumental facilities.

TH-2671_146153005

References

[1] W. G. Bae, H. N. Kim, D. Kim, S. H. Park, H. E. Jeong, K. Y. Suh, *Adv. Mater.* **2014**, *26*, 675.

[2] Philip Ball, *Patterns in Nature: Why the Natural World Looks the Way It Does*, **2018**.

[3] P. S. G. Pattader, I. Banerjee, A. Sharma, D. Bandyopadhyay, *Adv. Funct. Mater.* **2011**, *21*, 324.

[4] P. Roy, R. Mukherjee, D. Bandyopadhyay, P. S. Gooh Pattader, *Nanoscale* **2019**, DOI 10.1039/C9NR05729C.

[5] K. Y. Suh, Y. S. Kim, H. H. Lee, *Adv. Mater.* **2001**, *13*, 1386.

[6] K.-Y. Suh, M. C. Park, P. Kim, *Adv. Funct. Mater.* **2009**, *19*, 2699.

[7] K. Y. Suh, H. H. Lee, *Adv. Funct. Mater.* **2002**, *12*, 405.

[8] D. Salac, W. Lu, C.-W. Wang, A. M. Sastry, *Appl. Phys. Lett.* **2004**, *85*, 1161.

[9] E. Schaffer, T. Thurn-albrecht, T. P. Russell, S. Ullrich, *Nature* **2000**, *403*, 874.

[10] E. Schäffer, T. Thurn-Albrecht, T. P. Russell, U. Steiner, *Europhys. Lett.* **2001**, DOI 10.1209/epl/i2001-00183-2.

[11] P. Goldberg-Oppenheimer, U. Steiner, *Small* **2010**, DOI 10.1002/smll.201000060.

[12] E. Schaffer, T. Thurn-Albrecht, T. P. Russell, U. Steiner, *Nature* **2000**, *403*, 874.

[13] R. V. Craster, O. K. Matar, *Phys. Fluids* **2005**, *17*, 0.

[14] Z. Lin, T. Kerle, T. P. Russell, E. Schäffer, U. Steiner, *Macromolecules* **2002**, *35*, 6255.

[15] D. Bandyopadhyay, A. Sharma, U. Thiele, D. S. Reddy, *Langmuir* **2009**, *25*, 9108.

[16] Z. Lin, T. Kerle, T. P. Russell, E. Schäffer, U. Steiner, *Macromolecules* **2002**, *35*, 3971.

[17] P. D. S. Reddy, D. Bandyopadhyay, A. Sharma, *J. Phys. Chem. C* **2012**, *116*, 22847.

[18] M. D. Morariu, N. E. Voicu, E. Schäffer, Z. Lin, T. P. Russell, U. Steiner, *Nat. Mater.* **2002**, *2*, 48.

[19] K. A. Leach, S. Gupta, M. D. Dickey, C. G. Willson, T. P. Russell, *Chaos* **2005**, *15*, DOI 10.1063/1.2132248.

TH-2671_146153005

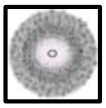

[20] G. Amarandei, P. Beltrame, I. Clancy, C. O'Dwyer, A. Arshak, U. Steiner, D. Corcoran, U. Thiele, *Soft Matter* **2012**, *8*, 6333.

[21] S. Srivastava, D. Bandyopadhyay, A. Sharma, *Langmuir* **2010**, *26*, 10943.

[22] N. Arun, A. Sharma, P. S. G. Pattader, I. Banerjee, H. M. Dixit, K. S. Narayan, *Phys. Rev. Lett.* **2009**, DOI 10.1103/PhysRevLett.102.254502.

[23] P. Roy, P. Sarathi, G. Pattader, *Bull. Mater. Sci.* **2020**, *0123456789*, DOI 10.1007/s12034-020-2073-0.

[24] M. H. Lu, Y. Zhang, *Adv. Mater.* **2006**, *18*, 3094.

[25] J. S. Park, S. H. Lee, T. H. Han, S. O. Kim, *Adv. Funct. Mater.* **2007**, *17*, 2315.

[26] C. Greiser, S. Ebert, W. A. Goedel, *Langmuir* **2008**, *24*, 617.

[27] S. Shojaei-Zadeh, S. R. Swanson, S. L. Anna, *Soft Matter* **2009**, *5*, 743.

[28] H. Bai, C. Du, A. Zhang, L. Li, *Angew. Chemie - Int. Ed.* **2013**, *52*, 12240.

[29] A. Zhang, H. Bai, L. Li, *Chem. Rev.* **2015**, DOI 10.1021/acs.chemrev.5b00069.

[30] A. Böker, Y. Lin, K. Chiapperini, R. Horowitz, M. Thompson, V. Carreon, T. Xu, C. Abetz, H. Skaff, A. D. Dinsmore, T. Emrick, T. P. Russell, *Nat. Mater.* **2004**, *3*, 302.

[31] A. Kumar, G. M. Whitesides, *Science (80-.).* **1994**, DOI 10.1126/science.263.5143.60.

[32] S. H. Yu, H. G. Girma, K. M. Sim, S. Yoon, J. M. Park, H. Kong, D. S. Chung, *Nanoscale* **2019**, *11*, 17709.

[33] R. Williams, J. Blanc, *J. Chem. Phys.* **2014**, *4675*, 8.

[34] J. Guadarrama-Cetina, R. D. Narhe, D. A. Beysens, W. Gonz??lez-Vi??as, *Phys. Rev. E - Stat. Nonlinear, Soft Matter Phys.* **2014**, *89*, 1.

[35] S. Biswas, A. Chakrabarti, A. Chateauminois, E. Wandersman, A. M. Prevost, M. K. Chaudhury, *Langmuir* **2015**, *31*, 13155.

TH-2671_146153005

[36] J. Liang, Q. Xia, S. Wang, J. Li, Q. Huang, R. D. Ludescher, *Food Hydrocoll.* **2015**, DOI 10.1016/j.foodhyd.2014.09.002.

[37] H. Xu, T. Zhu, R. P. Yu, *Guang Pu Xue Yu Guang Pu Fen Xi/Spectroscopy Spectr. Anal.* **2007**.

[38] J. Ding, A. Zhang, H. Bai, L. Li, J. Li, Z. Ma, *Soft Matter* **2013**, *9*, 506.

[39] A. Marchand, J. H. Weijs, J. H. Snoeijer, B. Andreotti, *Am. J. Phys.* **2011**, *79*, 999.

[40] R. N. Leach, F. Stevens, S. C. Langford, J. T. Dickinson, *Langmuir* **2006**, *22*, 8864.

[41] P. Roy, P. Sarathi, G. Pattader, *Bull. Mater. Sci.* **2020**, *0123456789*, DOI 10.1007/s12034-020-2073-0.

[42] R. Dey, U. U. Ghosh, S. Chakraborty, S. DasGupta, *Langmuir* **2015**, *31*, 11269.

[43] S. Chandrasekhar, *Liquid Crystals*, **1992**.

[44] C. D. Hodgman, *J. Opt. Soc. Am.* **1933**, *23*, 426.

[45] G. A. Truesdale, A. L. Downing, *Nature* **1954**, *173*, 1236.

[46] I. Kutsche, G. Gildehaus, D. Schuller, A. Schumpe, *J. Chem. Eng. Data* **1984**, DOI 10.1021/je00037a018.

TH-2671_146153005

Chapter 8

TH-2671_146153005

Chapter 8

CONCLUSIONS AND SCOPE FOR FUTURE WORK

8.1. Conclusions

The present thesis deals with some unexplored pathways and several original findings associated with soft films' patterning through electrohydrodynamics using 5CB nematic liquid crystal. The micro/nano feature size and the ultrafast ways of patterning without any expensive tool or material makes these techniques novel and handy. In all these patterning techniques, we define the characteristic wavelengths for each pattern, and it can be precisely controlled over a large area.

In **Chapter 3**, the effect of PDMS thin film's rheological properties in electrohydrodynamic instability of PDMS/5CB bilayer has been studied. It was found that for viscoelastic hard samples, microwells formed irrespective of film thickness. Whereas for soft viscoelastic sample, micropillars were predominantly formed in thin films, and a combination of micropillars and microwells were obtained for an $\sim$ 11 μm film. The otherwise hexagonally closed pack mesostructures were meticulously decorated as a patterned interface by selectively changing PDMS's rheological properties with masked UVO treatment.

In **Chapter 4,** the spatial variation of the electric field was introduced to the PDMS/liquid crystal bilayer settings under the electric field. The fast patterning technique of EHD in PDMS/liquid crystal bilayer was made ultrafast by creating an inhomogeneous electric field within the system using a patterned bottom electrode. Patterned electrodes allowed us to go below the barrier of electrode spacing used in our previous works. Spacer thickness of ~ 35 μm was used in all our previous experiments, and in this study, we could incorporate two gap distances of PDMS to the top electrode within that 35 μm range. It also offered three timescales of patterning. As a result, we got multiscale patterned PDMS substrate in the EFL experiment. Finally, we also decorated the patterned electrodes' surface with microwells/micropillars by tuning the incompletely crosslinked PDMS films' rheological properties.

TH-2671_146153005

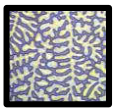

In **Chapter 5**, we demonstrated an ultrafast, template-less technique called ECLL. When the electric field was applied to PDMS/5CB confined bilayer, the liquid crystal layer either stayed static or directionally moving depending on the applied voltage. The static liquid crystal layer produced micro/nanopatterns on PDMS, which were hexagonally closed pack, and the process is termed electric field induced lithography (EFL). Moving 5CB layer generated fingering instability at the PDMS/5CB/air contact line due to high dielectric contrast and the Maxwells' stress at the interface. ECLL developed directional arrays of microwells. One application was demonstrated where these aligned microwells could be transformed into ordered arrays of micro pixels. ECLL generates two types of wavelengths, λ_c and λ_f . λ_c is the wavelength between two line arrays and λ_f is the average in-line wavelength. This micro-fabrication technique has the potential in the fabrication of MEMS/NEMS, optoelectronics, microsensors, etc.

In **Chapter 6**, a novel pattern rectification technique and a method to fabricate square patterns with sufficient accuracy were described. Though one-dimensional arrays of microwells were seen before in ECLL, this type of reorganization to an organized pattern has not been documented in the bilayer setup. The results of square patterned microwells obey the prediction from classical EHD instabilities, and perhaps it opens up a new field of patterning with liquid crystal contact line.

In **Chapter 7**, we demonstrated the coupling of two inexpensive patterning techniques, viz., breath figure patterning and electrohydrodynamic lithography, to prepare hierarchical multiscale patterns on a soft surface. Breath Figure (BF) of water microdroplets surrounding the dry band around an imprinted hygroscopic drop was used as a soft template on the soft elastomeric Polydimethylsiloxane (PDMS) surface. The dry band's width can be tuned by varying the duration of vapor exposure or changing the droplet's hygroscopicity, or using different hygroscopic materials. The rheology of the surface of the PDMS can be modified using UV-ozone (UVO) exposure. The variation of the hardness of the PDMS surface depends on the extent of UVO exposure and controlled by the UV transparency and availability of molecular oxygen in the hygroscopic drop and the water droplets. On this patterned soft surface, miniaturized microwells were fabricated exploiting the fast electric field induced lithography (EFL) technique. The work not only demonstrated the simple methodology for multiscale patterning technique but also offered an insight into the chemistry of UVO action on PDMS.

TH-2671_146153005

In summary, this thesis has introduced a study on the electrohydrodynamic lithography of the confined bilayer of PDMS/liquid crystal. This kind of high dielectric contrast interface can be used as a versatile patterning tool for the sub-micron or nanoscale patterning in thin films. A simple idea with a generic experimental procedure has been successfully investigated to transform into a footprint for future references or further applications.

8.2. Future scopes

The investigation of the interfacial morphology and deformation requires a blend of all research communities for new applications. However, with a complex fluid like liquid crystal, more support is needed from the numerical fraternity. Otherwise, experimental findings will remain unexplained, and the complex will get complicated. So far, based on the experimental findings, one can go in any of these directions in the near future.

- Both ECLL and EFL can be amalgamated to other existing soft lithographic techniques to incorporate its instability wavelength in the resulting pattern. For example, both can be used in combination with contact instability to fabricate multiscale patterns. The process can be used pattern microchannels having viscoelastic walls.
- More scientific exploration is required to tame the polymer/liquid crystal/air contact line under an electric field. The application of anchoring material at the interface or nanoparticle doping can enable one to control the contact line's velocity or geometry.
- One can perform EFL and ECLL for composite dielectric thin films and can expect new morphologies to discover.
- EHD instabilities for block copolymers and conducting polymers are still in their infancy.
- New material can be synthesized, which may be useful in EHD instabilities with new functionalities.

TH-2671_146153005

TH-2671_146153005

APPENDIX – A

A.1 Some other observations (Chapter 5)

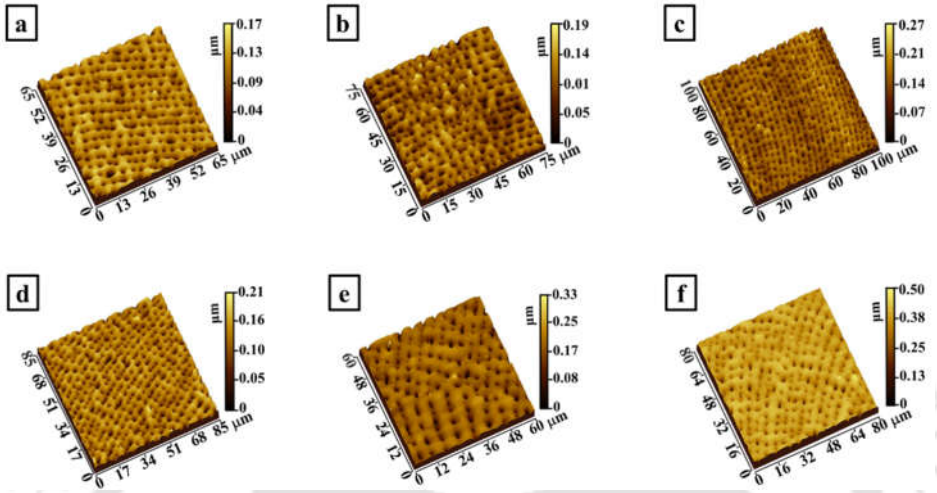

Figure A1.1 (a)-(f) Different intricate geometrical patterns formed through ECLL in a single flow of 5CB NLC. The PDMS film thickness is ~3 μm in all the cases

A.2 Some other observations (Chapter 7)

1. The contact line dynamics of central glycerol droplet changes and this change is dependent on γ_{ls} the component of surface energy. Depending on the interplay between the chemical and physical characteristics of the surface, the dynamics of the moving contact line vary. On glass surfaces, the ripening of evaporation induced condensed water droplets with moving contact line of central glycerol drop was observed (Figure A2.1). Surface imperfection induces pinning sites for advancing the contact line of glycerol drop.

TH-2671_146153005

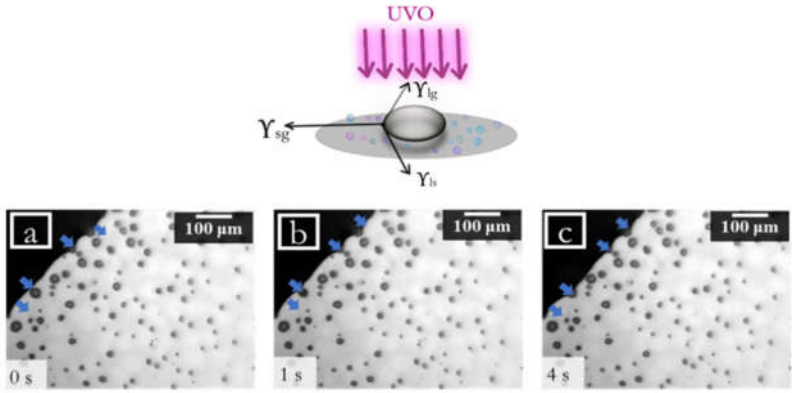

Figure A2.1 (a)-(c) Advancement of the contact line of central glycerol drop due to pinning sites present on a glass surface.

2. In the case of PS made petri dish surfaces inter coalescence among the deposited solvent droplets are observed. Due to the rapid kinetics of evaporation of condensed vapor droplets to get absorbed by central glycerol drop, the water droplets shrink their contact line with the reduced volume. γ_{ls} increases in this case due to mass loss. Here, this phenomenon often induces mobility to the water drops (Figure A2.2).

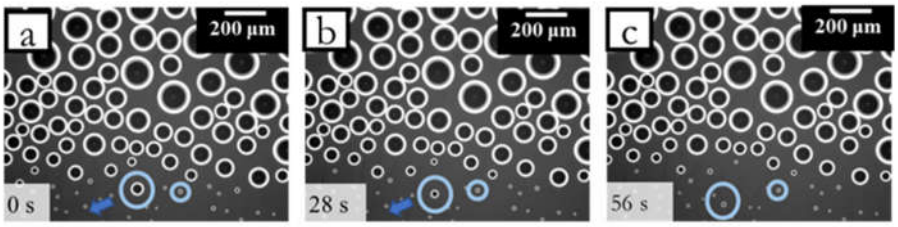

Figure A2.2 (a)-(c) Mobile condensed water droplet under mass loss during evaporation

3. Optical polarised micrograph and FESEM image of the microwell patterned glycerol drop imprint after breath figure and EFL experiment.

TH-2671_146153005

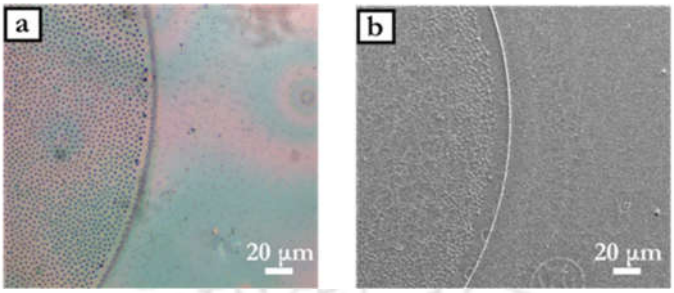

Figure A2.3 (a) Optical polarised micrograph taken after breath figure and EFL experiment. The glycerol droplet is patterned with microwells generated during the EFL experiment. The PDMS film thickness is ~3 µm. (b) Corresponding FESEM image of the same droplet.

4. For ethylene glycol (EG) droplet, the dry band is not actually dry. Near to the contact line of EG droplet, reverse morphology of the condensed water droplets is observed.(Figure A2.4a,b) In the case of polymeric polyethylene glycol 400 (liquid) drop, identical breath figure morphology of glycerol droplet is observed.(A2.1c,d)

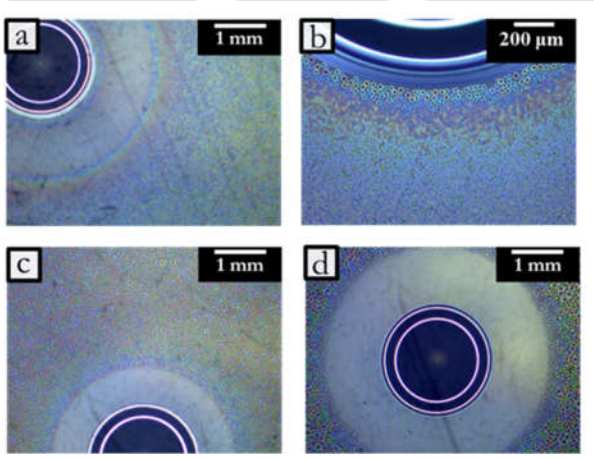

Figure A2.4 Breath-figures for two identical central hygroscopic droplets of (a)-(b) Ethylene glycol and (c)-(d) Polyethylene glycol 400 (liquid) on PS petri dish surface.

TH-2671_146153005

APPENDIX – B

Publications

Publications (From Ph.D. thesis work till Synopsis):

1. Roy, P., Mukherjee, R., Bandyopadhyay, D. & Gooh Pattader, P. S. Electrodynamic-contact-line-lithography with nematic liquid crystals for template-less E-writing of mesopatterns on soft surfaces. *Nanoscale* (2019) https://doi.org/10.1039/C9NR05729C
2. Roy, P., Gooh Pattader, P.S. Electrohydrodynamic instability: effect of rheological characteristics on the morphological evolution of liquid crystal–polymer interface. Bull Mater Sci 43, 169 (2020). (**Selected for cover**) https://doi.org/10.1007/s12034-020-2073-0
3. Three manuscripts are under preparation. (Chapter 4, Chapter 6 & Chapter 7)

Oral/Poster Presentations

- Participated in Paper presentation workshop in Reflux 2018, the Annual Chemical Engineering Symposium of IIT Guwahati (16th -18th March 2018)
- Participated and Contributed oral presentation at National Level Conference 'Characterization of Polymers and Polymeric Products 2019' (CPP-2019), held at Department of Polymer and Surface Engineering, Institute of Chemical Technology, Matunga, Mumbai, during September 17th & 18th, 2019.
- 1st National Student conference on 'Advances in Chemical Engineering' organized by Department of Chemical Engineering, Assam Engineering College, Assam, India on 30th August, 2019 (**Best Oral** in Oral Presentation).
- 2nd International Conference on Nanoscience and Nanotechnology (ICNAN '19), Centre for Nanotechnology Research (CNR), Vellore Institute of Technology (VIT), India, during 29th November – 1st December 2019.

TH-2671_146153005